INAUGURAL-DISSERTATION

zur Erlangung der Doktorwürde der
Naturwissenschaftlich-Mathematischen
Gesamtfakultät der
Ruprecht-Karls-Universität Heidelberg

vorgelegt von
M. Sc. Vasili Stumpf
aus Fergana

Tag der mündlichen Prüfung:
09.12.2016

Neutralization and relaxation of cations in an environment driven by interatomic decay processes

Gutachter:
Prof. Dr. Lorenz S. Cederbaum
Prof. Dr. Andreas Dreuw

To my dear parents

Abstract

Non-local electronic decay mechanisms constitute important pathways for the relaxation of cations produced by the action of ionizing radiation in van-der-Waals or hydrogen bonded chemical environment. Electronically excited cations may undergo the ultrafast Interatomic Coulombic Decay or ICD process, whereby the excess electronic energy is transferred to the environment and used to ionize it. It has been extensively studied by computational and experimental techniques during the last two decades and shown to operate in a variety of systems from rare gas dimers to large biomolecules. In this thesis we investigate using *ab initio* methods the Electron Transfer Mediated Decay or ETMD process which is responsible for the charge redistribution in environment, whenever atomic cations with a low excess energy and high electron affinity are produced. In ETMD electron transfer to the cation leads to the emission of an electron from the neighboring species. The net result is partial neutralization of the cation and the increase of the charge of the environment by two.

The light rare gas atoms He and Ne have a high ionization potential and, in the presence of a suitable neighbor are likely to undergo ETMD when they are singly ionized, e.g. by photoionization. In particular, we showed that a He·Mg cluster efficiently decays by ETMD whenever He is photoionized and a ground state He^+ ion is produced. The joint process of photoionization and ETMD corresponds to a one-photon double ionization of Mg. Remarkably, we found that the cross section of this process is three orders of magnitude higher than the cross section of the atomic one-photon double ionization, which demonstrates the prominent role of the neighboring He species in the double ionization. This mechanism of the ETMD driven one-photon double ionization was recently demonstrated experimentally in doped He nanodroplets and is proposed as a method for the experimental production of cold molecular dications.

Multiply charged rare gas cations have higher electron affinities and undergo ETMD with a larger variety of neighboring atoms or molecules. Such cations are naturally produced by the Auger decay following core ionization of rare gases in the X-Ray absorption. The ETMD process reduces their positive charge by one, i.e. leads to their partial neutralization and serves as a purely electronic alternative to neutralization mechanisms driven by the movement of the nuclei. Our calculations show that in small Ne^{2+}·Xe and Ne^{2+}·Kr_2 clusters the ETMD process takes place on a picosecond timescale. The ETMD in these systems is accompanied by nuclear dynamics which in turn enhance the rate of the electronic decay. We show that for such systems ETMD is an important mechanism responsible for the fast redistribution of the localized charge produced in the Auger decay process.

We also demonstrated that multiply charged hydrated metal cations are likely to decay via complicated cascades comprising both ETMD and ICD steps. Our calculations in the Mg^{2+}·$(H_2O)_6$ microsolvated cluster showed that such a cascade proceeds on a timescale of few hundreds of femtoseconds and leads to a massive degradation of the

metal's solvation shell through its multiple ionization and emission of slow electrons. Repulsive nuclear dynamics at later stages of the cascade, which were not taken into account explicitly, are expected to considerably reduce its duration. We expect that studying interatomic decay cascades of metal cations is important for understanding mechanisms of the damage caused by X-Rays to metal containing biomolecules such as DNA, metalloproteins etc. For the latter of particular importance is the knowledge of the duration of different interatomic decay steps, since it determines the timescale at which proteins become damaged by X-Rays and beyond which their structure becomes compromised.

These considerations led us to investigate the dependence of ICD lifetimes on atomic charge in excited microhydrated Na^{2+} and Mg^{3+} cations. Our *ab initio* results reproduce within the numerical error the experimental ICD lifetimes of the respective ions in aqueous solutions. We show that the microsolvated Mg^{3+} cations decay faster than the Na^{2+} ones, in accordance with experiments on aqueous solutions. The detailed analysis reveals that at characteristic metal-water separations the polarization of the water neighbor enhances ICD the stronger the higher the charge of the metal is. This, together with the shorter Mg-water equilibrium distances, leads to the observed ordering of the ICD rates. We also showed that polarizing the neighbors causes sub-linear growth of ICD rates with the number of water molecules in the first solvation shell. This investigation of ICD in microsolvated metal cations demonstrated the prominent role the cation's charge and the consequent polarization of the medium have on the decay rate. It also leads to a reasonable expectation that even faster, sub-femtosecond decay lifetimes might be achieved for highly charged solvated metals ions.

Kurzfassung

Nichtlokale elektronische Zefallsmechanismen stellen wichtige Relaxationswege für Kationen dar, die durch Einwirkung der ionisierenden Strahlung entstehen und in eine durch van-der-Waals Kräfte oder Wasserstoffbrücken gebundene chemische Umgebung eingebettet sind. So können elektronisch angeregte Kationen nach dem Mechanismus des interatomaren Coulombschen Zerfalls (ICD) relaxieren, wobei die überschüssige Energie auf die chemische Umgebung übertragen und zu deren Ionisierung verwertet wird. Dieser Zerfallsmechanismus wurde in den vergangenen zwei Jahrzehnten mittels computergestützter und experimenteller Methoden ausgiebig erforscht. Die Vielfalt der Systeme, in welchen er nachweislich auftritt, reicht von kleinen Edelgasdimeren bis zu großen biologischen Molekülen. In der vorliegenden Arbeit untersuchten wir mittels *ab initio* Methoden den Elektronentransfer-vermittelten Zerfall (ETMD), welcher für die Umverteilung der positiven Ladung in chemischer Umgebung sorgt, sobald atomare Kationen mit einer niedrigen Überschussenergie und hoher Elektronenaffinität auftreten. Die Übertragung eines Elektrons auf das Kation im Zuge des ETMD hat die Emission eines weiteren Elektrons von der benachbarten Spezies zur Folge. Insgesamt wird das Kation partiell neutralisiert und seine chemische Umgebung zweifach positiv geladen.

Die leichten Edelgasatome He und Ne besitzen ein hohes Ionisierungspotential und können daher nach der Einfachionisierung (bspw. durch Photoionisation) in der Anwesenheit einer geeigneten Nachbarspezies durch ETMD zerfallen. So konnten wir zeigen, dass der He·Mg Cluster effizient durch ETMD zerfällt, falls ein He^+ Ion im Grundzustand durch Photoionisierung von He erzeugt wird. Die Gesamtsequenz der Photoionisierung und des darauffolgenden ETMD entspricht einer Ein-Photonen-Doppelionisierung von Mg. Überraschenderweise ist der von uns ermittelte zugehörige Querschnitt der Doppelionisierung um drei Größenordnungen höher als der atomare Querschnitt der Ein-Photonen-Doppelionisierung. Dies unterstreicht die bedeutende Rolle der He Nachbarspezies in der Doppelionisierung. Der Mechanismus der durch ETMD vermittelten Ein-Photonen-Doppelionisierung wurde kürzlich experimentell in Helium Nanotröpfchen nachgewiesen und als eine Methode für die Erzeugung von kalten molekularen Dikationen vorgeschlagen.

Mehrfach geladene Edelgaskationen besitzen höhere Elektronenaffinitäten, folglich steht eine breitere Auswahl an Atomen und Molekülen als Nachbarspezies für ETMD zur Verfügung. Solche Kationen werden naturgemäß durch den Auger-Zerfall erzeugt, welcher bei Edelgasen nach dem Entfernen der kernnahen Elektronen durch Röntgenstrahlung auftritt. Der ETMD Prozess reduziert ihre positive Ladung um eins, d.h. er führt zu deren partiellen Neutralisation und stellt eine rein elektronische Alternative zu Neutralisationsmechanismen dar, die durch die Bewegung der Atomkerne vermittelt werden. Unsere Berechnungen zeigen, dass in kleinen Ne^{2+}·Xe und Ne^{2+}·Kr_2 Clustern ETMD auf einer Pikosekundenzeitskala abläuft. Der Prozess wird von einer Kerndynamik begleitet, die im Umkehrschluss dessen Rate erhöht. Wir zeigen, dass in solchen

Systemen ETMD für eine schnelle Umverteilung der lokalisierten Ladung sorgt, welche durch den Auger-Zerfall erzeugt wird.

Weiterhin konnten wir demonstrieren, dass mehrfach geladene Metallkationen durch komplizierte Kaskaden bestehend aus ICD und ETMD Schritten zerfallen können. Unsere Berechnungen im mikrosolvatisierten $Mg^{2+}\cdot(H_2O)_6$ Cluster zeigten, dass eine solche Kaskade auf einer Zeitskala von wenigen hundert Femtosekunden ablaufen kann und aufgrund der mehrfachen Ionisierung und Emission langsamer Elektronen eine erhebliche Schädigung der Solvatationshülle des Metalls verursacht. Wir erwarten eine weitere Verkürzung der Kaskadendauer durch repulsive Kerndynamik, welche im späten Stadium der Kaskade auftritt und nicht explizit berücksichtigt werden konnte. Wir nehmen an, dass die Untersuchung interatomarer Zerfallskaskaden von Metallkationen relevant für das Verständnis der Mechanismen der Schädigung von metallhaltigen biologischen Molekülen wie bspw. DNA, Metalloproteinen etc. durch Röntgenstrahlung ist. Für Metalloproteine ist die Kenntnis der Dauer unterschiedlicher interatomarer Zerfallsschritte von besonderer Bedeutung: diese Dauer legt die Zeitskala ihrer Schädigung durch Röntgenstrahlung fest und somit auch den Zeitpunkt, von dem an die ermittelte Struktur nicht mehr aussagekräftig ist.

Diese Überlegungen veranlassten uns, die Abhängigkeit der ICD Lebensdauern von der Ladung der angeregten, mikrohydrierten Na^{2+} and Mg^{3+} Kationen zu untersuchen. Die Ergebnisse unserer *ab initio* Berechnungen stimmen innerhalb des numerischen Fehlers mit den experimentellen ICD Lebensdauern der entsprechenden Ionen in wässriger Lösung überein. Wir zeigen, dass mikrosolvatisierte Mg^{3+} Kationen schneller zerfallen als Na^{2+} Kationen, im Einklang mit den Ergebnissen der Experimente in wässrigen Lösungen. Die detaillierte Analyse demonstriert, dass bei typischen Metall-Wasser Abständen die Polarisation des benachbarten Wassers ICD umso mehr verstärkt, je höher die Ladung des Metalls ist. Dies, zusammen mit kürzeren Mg-Wasser Gleichgewichtsabständen, führt zu der genannten Reihenfolge der ICD Raten. Es wurde weiterhin gezeigt, dass die Polarisation der Nachbarn ein nichtlineares Wachstum der ICD Raten in Abhngigkeit von der Anzahl der Wassermoleküle in der ersten Solvatationshülle verursacht. Somit demonstriert die Studie des ICD in mikrosolvatisierten Metallkationen den ausgeprägten Einfluss der Ladung des Kations und der dadurch bedingten Polarisation des Mediums auf die Zerfallsrate. Dieses Ergebnis begründet die Annahme, dass bei hoch geladenen, solvatisierten Metallionen ICD Lebensdauern unterhalb einer Femtosekunde erreicht werden können.

List of publications

V. Stumpf, P. Kolorenč, K. Gokhberg and L. S. Cederbaum. "Efficient pathway to neutralization of multiply charged ions produced in Auger processes" *Phys. Rev. Lett.* **110**, 258302 (2013).⋆

V. Stumpf, N. V. Kryzhevoi, K. Gokhberg and L. S. Cederbaum. "Enhanced one-photon double ionization of atoms and molecules in an environment of different species" *Phys. Rev. Lett.* **112**, 193001 (2014).⋆

G. Jabbari, T. Miteva, V. Stumpf, P. O'Keeffe, A. Ciavardini, P. Bolognesi, M. Coreno, L. Avaldi, E. Keshavarz, M. Ghandehari, M. Tozihi, C. Callegari, M. Alagia, K. C. Prince, A. Kivimäki and R. Richter. "Soft X-ray absorption spectroscopy of Ar_2 and ArNe dimers and small Ar clusters" *Phys. Chem. Chem. Phys.* **17**, 22160 (2015).

V. Stumpf, K. Gokhberg and L. S. Cederbaum. "The role of metal ions in X-ray-induced photochemistry" *Nat. Chem.* **8**, 237 (2016).⋆

A. C. LaForge, V. Stumpf, K. Gokhberg, J. von Vangerow, F. Stienkemeier, N. V. Kryzhevoi, P. O'Keeffe, A. Ciavardini, S. R. Krishnan, M. Coreno, K. C. Prince, R. Richter, R. Moshammer, T. Pfeifer, L. S. Cederbaum and M. Mudrich. "Enhanced ionization of embedded clusters by electron-transfer-mediated decay in helium nanodroplets" *Phys. Rev. Lett.* **116**, 203001 (2016).⋆

V. Stumpf, S. Scheit, P. Kolorenč and K. Gokhberg. "Electron transfer mediated decay in NeXe triggered by K-LL Auger decay of Ne" *Chem. Phys.*, (2016) http://dx.doi.org/10.1016/j.chemphys.2016.08.018.⋆

V. Stumpf, C. Brunken and K. Gokhberg. "Impact of metal ion's charge on the interatomic Coulombic decay width in microsolvated clusters" *J. Chem. Phys.* **145**, 104306 (2016).⋆

T. Ouchi, V. Stumpf, T. Miteva, H. Fukuzawa, K. Sakai, X.-J. Liu, T. Mazza, M. Schöffler, H. Iwayamah, K. Nagaya, Y. Tamenori, N. Saito, A. I. Kuleff, K. Gokhberg and K. Ueda. "Ion pair formation in the NeAr dimer irradiated by monochromatic soft X-rays" *Chem. Phys.*, (2016) http://dx.doi.org/10.1016/j.chemphys.2016.09.032.

⋆Results presented in this work.

Contents

List of abbreviations

1h	one-hole
2h	two-hole
2h1p	two-hole one-particle
ADC	Algebraic Diagrammatic Construction scheme
ADC(2)	second-order Algebraic Diagrammatic Construction scheme
ADC(2x)	extended second-order Algebraic Diagrammatic Construction scheme
ADC(3)	third-order Algebraic Diagrammatic Construction scheme
ATP	Adenosine TriPhosphate
CAP	Complex Absorbing Potential
CCSD(T)	Coupled-Cluster Singles Doubles and perturbative Triples
CI	Configuration Interaction
DIE	Double Ionization Energy
DIP	Double Ionization Potential
DNA	DesoxyriboNucleic Acid
EE	Excess Energy
EA	Electron Affinity
EOM-CCSD	Equation-Of-Motion Coupled Cluster Singles and Doubles
ETMD	Electron Transfer Mediated Decay
ETMD(2)	Electron Transfer Mediated Decay involving 2 monomers
ETMD(3)	Electron Transfer Mediated Decay involving 3 monomers
FCI	Full Configuration Interaction
ICD	Interatomic Coulombic Decay
IE	Ionization Energy
IP	Ionization Potential
ISR	Intermediate State Representation
KBJ	Kaufmann-Baumeister-Jungen
KER	Kinetic Energy Release (of the nuclei)
MBPT	Many-Body Perturbation Theory
MP2	second order Møller-Plesset perturbation theory
MRCI	Multi-Reference Configuration Interaction
MRCI-S	Multi-Reference Configuration Interaction Singles
MRCI-SD	Multi-Reference Configuration Interaction Singles and Doubles
PEC	Potential Energy Curve
PES	Potential Energy Surface
RCT	Radiative Charge Transfer
RHF	Restricted Hartree-Fock
SCF	Self-Consistent Field
SRCI	Single-Reference Configuration Interaction
TIP	Triple Ionization Potential
XFEL	X-Ray Free-Electron Laser

1 Introduction

Detailed investigation of energy and charge transfer processes [1, 2] is a prerequisite for understanding such important phenomena as conversion of solar energy into electricity, photosynthesis, or redox reactions. The transfer processes typically proceed in an extended chemical environment, e.g. a solvent or a solid, which bears several important functions. The environment has an impact on the energetics of the process; a polar or a polarizable medium may stabilize or destabilize the electronic states involved, therefore, making the processes thermodynamically allowed or forbidden. It furthermore acts as a thermal bath dissipating the excess energy, and thus, steering the process in a certain direction. Finally, the kinetics of the process are largely influenced by the electronic and nuclear reorganization of the medium in its course [3].

For highly electronically excited species the role of the chemical environment is augmented by a further important aspect: it provides an electronic continuum which can efficiently couple to the excitation. As a result, a new mechanism of energy transfer becomes available, where the excess energy brought to the environment is dissipated via electron emission. This mechanism (see Fig. 1.1), known as the Interatomic Coulombic Decay (ICD) [4], has been demonstrated to be highly efficient for electronically excited atoms and molecules embedded in a host chemical environment. Due to the high efficiency, ICD was shown to quench competing relaxation pathways such as fluorescence [5] and dissociative nuclear dynamics [6, 7].

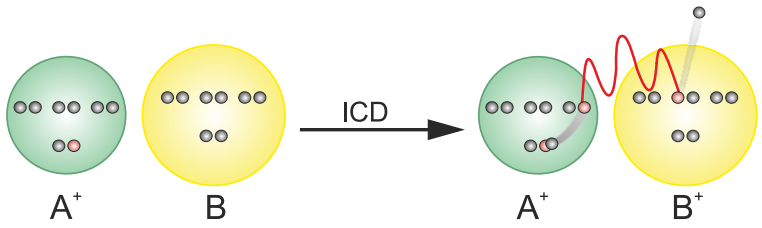

Figure 1.1: Schematic description of the ICD relaxation mechanism of an inner-valence ionized atom A embedded into a non-covalent environment. Excess energy is released by the relaxation of an outer-valence electron into a singly occupied inner-valence orbital (red circle). This excess energy (red line) is utilized to ionize the neighbor B.

Charge transfer processes can be coupled to the electronic continuum of the chemical environment as well, giving rise to the Electron Transfer Mediated Decay (ETMD) mechanism [8]. The mechanism is operative for positively charged ions embedded non-covalently into a weakly bound chemical environment (see Fig. 1.2). If the electron affinity of the ion is sufficiently high, a considerable excess energy is released in an electron transfer from the environment. This excess energy is utilized for the ionization of the latter, which in total loses two electrons in the course of the ETMD process. In an

environment consisting of weakly interacting units (see. Fig. 1.2), two distinct variants of ETMD can be defined. In the case where the electron donor is ionized, the process is assigned as ETMD(2) while the ionization of a different neighbor is described by the ETMD(3) process.

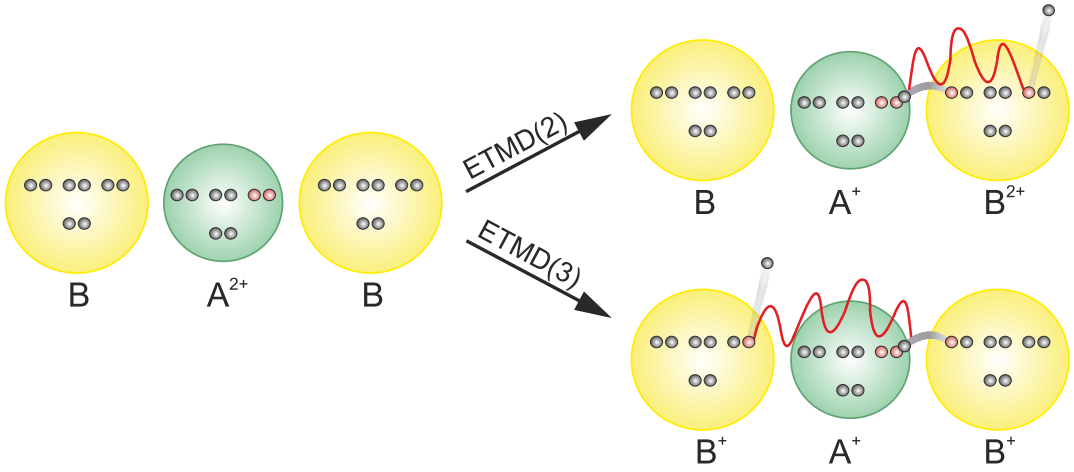

Figure 1.2: Schematic description of the ETMD relaxation mechanism of a doubly outer-valence ionized atom A embedded into a non-covalent environment. An electron transfer from a neighboring species B (gray line) provides an excess energy (red line) which is utilized to ionize either the electron donor(ETMD(2) process) or a different neighbor (ETMD(3) process).

ICD as a novel electronic decay process has gained increasing attention of experimentalists and theorists since its theoretical formulation in the year 1997 [4]. The first experimental evidence of ICD after the inner-valence ionization of neon clusters was provided by means of electron spectroscopy [9]. Being an interatomic electronic process, ICD produces pairs of positive ions (often denoted as nuclei in ion detection experiments), which undergo Coulomb explosions. This feature was utilized for the unambiguous experimental proof of the ICD mechanism, where pairs of ions stemming from the Coulomb explosions of neon dimers were identified together with the ICD electrons by coincidence spectroscopy [10]. Measurements in the coincident regime allow to discriminate groups of particles (electrons, ions) produced in a specific physical event (e.g. electronic decay producing electrons and ions) from the uncorrelated signal background. Since then ICD has been investigated experimentally both by electron and ion spectroscopy in different classes of systems such as rare gas and hydrogen bonded clusters, interfaces, aqueous solutions etc. [11–14]. ICD represents a characteristic probe of a pair of atoms and molecules in which it takes place. For each pair the ICD electrons have characteristic energies which depend on the excited state and are, otherwise, independent of the energy of the pumping photon. Moreover, since it occurs predominantly between the nearest neighbors, the observation of these electrons gives us information about the mutual arrangement of the atoms or molecules in a medium. Therefore, ICD was utilized as a spectroscopic tool to study structure of mixed rare gas clusters [15, 16]. As such it can be considered a complementary technique to the Auger electron spectroscopy - a routine spectroscopic tool in surface science [17].

The main subject of computational studies of ICD has been the accurate prediction

of the observables, i.e. the kinetic energy spectra of the electrons and the nuclei [18]. A further major issue of these studies has been the computation of the ICD lifetimes. On the one hand, these quantities are required for the computation of the ICD observables - on the other hand, the ICD lifetimes are of great interest by themselves. For a process to be efficient, its lifetime has to be shorter than the lifetimes of its competitors. Several theoretical approaches with different levels of accuracy have been developed for determining this notoriously difficult to compute quantity [19–22]. Experimental ICD lifetimes were extracted from the signal broadening in the photoelectron spectra of large rare gas clusters and solutions [14, 23]. They confirmed the femtosecond timescale of ICD predicted by computational approaches. Recently, time-resolved ICD experiments enabled to obtain the timescale of ICD in rare gas dimers by a direct measurement and produced results in good agreement with theory [24, 25].

Overall, a solid knowledge of the ICD process has been acquired during the last two decades, owing to the development of the experimental and computational methods. In contrast to ICD, the knowledge of the ETMD process is limited, which is mainly due to its original formulation as an inferior competitor of ICD in ionized-excited systems where both processes may occur simultaneously. This inferiority of ETMD is a consequence of the low efficiency of the electron transfer compared to the transfer of energy in ICD. Hence, first experimental observations of ETMD were provided only recently by specific kinds of inner-valence ionized rare gas dimers and clusters, where ICD was forbidden either due to energy conservation or due to spin conservation rules [26, 27].

We were able to find a broad class of systems which decay predominantly by ETMD when embedded into a weakly bound environment. Singly or multiply ionized atoms with holes in the outermost occupied orbitals possess none or only a little excess energy. Therefore, a relaxation of these cations via ICD is not possible. However, they may have very large electron affinity and may therefore undergo ETMD. In this thesis we present a comprehensive study of ETMD in cations with holes in the outermost occupied orbitals. We studied both its fundamental properties and its role in more complicated electronic processes unleashed by X-ray photoabsorption. On a technical level this work includes computing the corresponding lifetimes and experimentally available observables, such as kinetic energies of the emitted electrons and of the nuclei. We selected the systems for investigation with a view for collaborating with the experimentalists. Indeed, comparison with the experimental results would allow us to verify the quality of the utilized models and to benchmark the numerical methods. On the other hand, the computed observables could be used for the interpretation of the experimental data. The *ab initio* electronic structure methods, which are required for the computation of the decay lifetimes and the kinetic energy spectra of the decay products, are described in the chapter 2.

The most obvious way to create an atomic cation with holes in the outermost orbitals is the photoemission, i.e. emission of an electron due to the interaction with highly energetic light. Consider, for example, the helium atom, whose already singly charged cation has considerable electron affinity of 24.6 eV. It is larger than the double ionization energy of a magnesium atom. Therefore, in the presence of a magnesium neighbor electronic relaxation of He^+ via ETMD(2) takes place, leading to the double ionization of the metal and the production of the Mg^{2+} ion. The joint process of the helium photoionization and the subsequent ETMD(2) can be viewed as a one-photon double

ionization of magnesium. This double ionization mechanism can be applied not only to atoms but also to molecules having low double ionization energies. For example, polyaromatic hydrocarbons such as anthracene, phenanthrene and larger polyacenes have double ionization energies of less than 20 eV [28]. Embedding these molecules into a helium environment would allow to produce by a soft ionization molecular dications and to investigate them spectroscopically.

A specific sort of helium environment is readily available experimentally in the form of helium nanodroplets [29]. These ultracold, superfluid clusters of helium atoms have been used as nanoscopic matrices for the spectroscopic characterization of the embedded atoms and molecules [30]. In our study of the double ionization driven by ETMD, we first investigated the double ionization process in the He·Mg diatomic by means of *ab initio* methods. Later on, in collaboration with the research group of PD M. Mudrich from the Freiburg University we participated in an experiment investigating the same mechanism of double ionization in helium nanodroplets doped with magnesium clusters.

Another way to produce atomic cations with holes in the outermost orbitals and a high electron affinity, which is applicable to a significantly broader range of systems, is given by the atomic Auger decay. It is initiated by the core ionization of an atom, which results in highly energetic ionic states. The energy is released by filling the core hole with an electron from an energetically higher shell and emitting a second such electron into the continuum. In light elements this process mostly leads to the production of doubly charged cations. In heavier elements creation of holes in deep lying electronic levels results in cascades of Auger steps and multiply charged products. The relaxation mechanism for the products of Auger decay in an environment depends on their excess energy. The cations with a sufficiently high excess energy decay by ICD, as was proposed by Santra et al. [31]. The existence of this Auger-ICD cascade was verified in numerous experiments [32, 33]. For the cations with holes in the outermost orbitals embedded in a suitable environment ETMD becomes the dominant relaxation mechanism.

A good starting point for studying this Auger-ETMD cascade is the Ne·Xe model cluster. The majority of the outer-valence doubly ionized states produced in the Auger decay of neon fulfills the energetic criteria to undergo ETMD(2) in the presence of a xenon neighbor. The simplicity of this system, possessing only a single internal nuclear degree of freedom, permitted a detailed study of ETMD(2) by applying accurate *ab initio* quantum chemical methods both for the description of the electronic structure and of the nuclear dynamics. This approach was proven to be successful in the studies of ICD in the neon dimer [10,34], where a close collaboration between the theoreticians and experimentalists helped to understand basic features of ICD and to improve the accuracy of the computational methods. Hence, with our study we also aimed to motivate future experiments on the Auger-ETMD(2) cascade in Ne·Xe.

From the point of view of the neon dications obtained in the Auger decay of Ne·Xe, ETMD(2) facilitates their neutralization, reducing the positive charge by one. This finding is in agreement with the above definition of ETMD as an electron transfer mechanism enabled by the coupling to the electronic continuum of the medium. Hence, studying the timescale of ETMD after Auger provides important information about its relevance as a neutralization mechanism. In an extended chemical environment, in addition to ETMD(2), the ETMD(3) mechanism is expected to play a significant role in the charge neutralization. It benefits from the less strict energy conservation

condition and the more favorable scaling of its efficiency on the size of the system. Thus, replacing the xenon by a krypton neighbor prohibits the Auger-ETMD(2) cascade due to the higher double ionization potential of krypton. However, adding a second krypton neighbor offers a possibility to study the Auger-ETMD(3) cascade instead. The goal of our study on Ne·Kr_2 was to determine the ETMD(3) lifetimes in and to characterize the impact of the nuclear dynamics on these lifetimes.

Cascades involving Auger decay and the subsequent interatomic electronic decay steps are not of purely academic interest but have features which make them potentially relevant for the damage of biological systems by X-Rays. The main physical effect of the latter on the biological matter lies in the core ionization of the matter constituents. For the light chemical elements (C, N, O, P), the largest portion of the energy stored by the core ionization is taken away by the Auger electrons and utilized for secondary electron impact ionizations and excitations of the environment. These events are well-studied and considered as the main source of the damaging effect of the X-Rays [35].

The fate of the cations produced in the Auger decay depends on their structure. Molecular cations in general may dissociate distributing the positive charge [36], while for excited cations ICD is available as well, which was demonstrated by Stoychev et al. for water dimers [37]. In the relaxation via ICD low-energy electrons are released while stable neighboring molecules, such as water, are converted into radicals. Both sorts of species are highly reactive and thus are able to damage the biomolecules in the vicinity of the initial ionization site [38, 39]. Therefore, an enhancement of the X-Ray induced radiation damage due to ICD can be anticipated. In this context, Gokhberg et al. (theory) [40] and Trinter et al. (experiment) [41] introduced the resonant Auger-ICD cascades initiated by X-Ray absorption as a tool for the production of low-energy ICD electrons and control of their location and energy. The authors furthermore proposed this scheme for the radiotherapeutic treatment of cancer cells.

For atomic cations produced by core ionization and subsequent Auger decay no dissociative degrees of freedom are available, hence, not only the fast ICD but also the slower ETMD mechanism is expected to play an important role in their relaxation. In terms of radiation damage the impact of ETMD, which produces slow electrons and pairs of radicals, is even higher than the impact of ICD. Nevertheless, the total number of reactive species released after the Auger decay is considerably larger than the number of those released by the interatomic decay since the Auger electron has a high kinetic energy and dissipates it ionizing the environment many times. Therefore, the contribution of the interatomic decay to the X-Ray induced radiation damage may at first glance appear insignificant. However, the ionizations caused by the Auger electron are randomly distributed along its path through the system. In contrast, reactive species produced by both ICD and ETMD are localized in the vicinity of the core ionization site. Taking into account the limited mean free path of radicals and electrons in biological systems [42, 43], a prominent contribution of interatomic decay initiated in the vicinity of biomolecules to the X-Ray induced radiation damage should be expected.

Interestingly, ETMD and ICD can be considered as complementary processes with respect to the conditions under which they occur. Thus, for ICD the charge of the excited species does not play a crucial role but a sufficient excess energy is necessary, whereas ETMD does not require an excess energy but is possible only if the central atom bears a sufficiently high charge. Therefore, while the low energy cations produced by Auger

decay are expected to undergo ETMD, the excited cations are likely to lose their excess energy in an ICD step and subsequently undergo ETMD, giving rise to an ICD-ETMD cascade. If the cations produced by Auger decay are multiply charged, interatomic decay will ensure the transfer of electronic energy to the environment and gradual neutralization of the cation. Obviously, multiply charged atomic cations produced by Auger decay can dissipate their excess energy and their excess positive charge to the environment in multistep interatomic electronic decay cascades. Multiple ionizations of the neighboring molecules take place all along these decay cascades.

We found a suitable class of chemical systems for the realization of this scenario in microsolvated metal ions. Due to the presence of the initial positive charge on the metal, we expect multiply charged metal cations to be produced already in the one-step Auger decay process. We would like to answer the question - how much damage a core ionization of the metal is able to cause to the metal's environment by means of a multistep electronic cascade involving Auger, ICD and ETMD steps? To investigate such a cascade, we chose the $Mg^{2+}\cdot(H_2O)_6$ model system. In our study we concentrated on the timescales and branching ratios of the interatomic decay, required to estimate the distribution of the decay products. Nuclear dynamics are not taken into account explicitly because of the numerical limitations, only a discussion of their influence on the cascade duration is included.

Metal atoms are abundant in biological systems and appear mostly as cations bound either by electrostatic or coordinative interactions. In the former case the metal ions (Na, K, Mg, Ca) bear such important functions as signaling and stabilizing or controlling the structure of the multiply negatively charged macromolecules, e.g. DNA or proteins. In the metalloenzymes and metal cofactors the strongly bound metals (Fe, Zn, Cu etc.) directly participate in the catalytic processes, acting as Lewis acids and facilitating electrons transfer, group transfer and further important types of reaction steps [44]. The structure of metalloenzymes is a subject of X-Ray crystallographic studies, where an accumulation of the radiation damage is frequently observed in the course of the measurement [45]. This damage is often non-random and involves specific functional groups, e.g. carboxylates and disulfides [46]. The metal centers are one of the vulnerable spots as well, becoming modified already at relatively low radiation doses [47, 48]. Typical damage patterns are the reduction of the metal and modification of the metal-ligand distances [47, 49]. The underlying mechanisms have not yet been sufficiently investigated, mainly addressing the attachment of the X-Ray photoelectrons to the metal center [45, 48, 50]. Cascades of interatomic processes discussed above initiated by the adsorption of X-Rays by the metal center may add to our understanding of crystallographic radiation damage and in general, radiation damage of biological compounds exposed to metal atoms (e.g. proteins, nucleic acids, cofactors etc.).

Recently, a new experimental technique was introduced to obtain damage-free crystallographic structure of proteins [51]. The underlying idea is the application of extremely intense, femtosecond X-Ray pulses which have become available due to the development of X-Ray Free-Electron Lasers (XFEL) [52] over the last decade. Under such conditions it is not the extent of the radiation damage which is relevant for the quality of the recorded structure but rather the timescale on which it occurs. The goal is to record a structure before the molecule is destroyed by the radiation and, therefore, the measurement should take shorter time than the characteristic rates of damaging pro-

cesses. Interatomic decay processes are able to induce repulsive nuclear dynamics on a femtosecond timescale by ionizing the molecules in the vicinity of the metal center. In this context, especially the very efficient ICD mechanism and the factors governing its timescale are of great interest if one wishes to estimate the onset of the structural modifications in metalloproteins.

ICD is driven by the Coulombic interaction between the relaxing electron on the excited atom and the electron on the neighboring species which is transferred into the continuum. Therefore, the ICD lifetime is sensitive to the average distance between these electrons. A parameter directly influencing the average distance between the electrons participating in ICD is the distance between the atoms on which they are located. The ICD lifetimes in rare gas dimers, the most extensively studied systems, were found to lie in the tens to hundreds of femtoseconds range at characteristic interatomic distances between 3 Å and 4 Å [21, 24, 25, 53]. In water dimers, where the equilibrium distance between the monomers is significantly smaller, the efficiency of ICD is enhanced and the process becomes sufficiently fast to quench the proton transfer after inner-valence ionization [12]. For positively charged species decaying by ICD an additional enhancement may appear due to the polarization of the neighbor. Again, the effect of the polarization is to bring the electrons on the neighbor closer to the electrons of the decaying species without moving the nuclei to which these electrons are bound. Another parameter which has strong effect on the ICD lifetime is the number of the neighbors, since more electrons is available for the electronic decay. Thus, in the case of neon clusters the ICD lifetime of the bulk atoms lies below 10 fs compared to about 100 fs in the Ne dimer [14, 54].

The ICD steps involved in the decay cascade of $Mg^{2+}\cdot(H_2O)_6$ exhibit ultrashort lifetimes of only few femtoseconds at most. An experimental study by Öhrwall et al. supports these findings. They determined an ICD lifetime of 1.5 fs for magnesium trications in aqueous solution [14]. The authors furthermore determined the ICD lifetimes of sodium and aluminum ions to lie at 3.0 and 0.9 fs, respectively. To rationalize the reduction of the ICD lifetime with the growing charge of the metal, they proposed decreasing metal-oxygen distances in the equilibrium solvation structures and the growing polarization of the water molecules by an ion as the relevant parameters which depend on the ionic charge. By means of *ab initio* methods we were able to disentangle the effects of these parameters. To do that we calculated ICD lifetimes switching off the polarization effects in the ionized state and varying the distance between the metal ion and the water ligands.

The thesis is organized as follows. In the next chapter the *ab initio* methods for computations of electronic decay widths and energies of the initial states and products of electronic decay are introduced. The third chapter contains the methodological and computational details of the conducted *ab initio* studies. In the fourth chapter we discuss the double ionization process mediated by ETMD in the He·Mg cluster and analyze the results of the experiment dealing with double ionization of magnesium clusters in helium nanodroplets. In the fifth chapter we characterize the timescales of the Auger-ETMD cascades in the Ne·Xe and $Ne\cdot Kr_2$ clusters, leading to the neutralization of the neon dication. For the Ne·Xe cluster, kinetic energy spectra of the ETMD electrons and nuclei are presented. Chapter six contains a detailed discussion of the interatomic decay cascade in the $Mg^{2+}\cdot(H_2O)_6$ cluster with the focus on the cascade duration and yields

of the reactive products of decay, i.e. electrons and ionized water molecules. In chapter seven the dependence of ICD lifetimes on metal-oxygen equilibrium distances, coordination number and polarization effects in $Na^+ \cdot (H_2O)_m$ ($m = 1 - 4$) and $Mg^{2+} \cdot (H_2O)_n$ ($m = 1 - 6$) clusters is investigated. In chapter eight we present an overview of the obtained results and make suggestions for future studies on the interatomic electronic decay processes and the required methodological development.

2 Electronic structure methods

The major goal of the present work lies in the quantitative characterization of interatomic electronic decay processes and cascades of such processes. The initial step within a computational study of electronic decay is computing the initial and final states and identify open channels from the energy conservation. The efficiency of a decay process, directly related to its relevance, is determined by the decay lifetime. Since the lifetimes corresponding to the electronic decay mechanisms discussed in the present work are non-trivial quantities to compute and not common in the literature, they constitute the main quantity of interest.

For a decay process, a comprehensive study of the decay products is instructive. Ideally, their distribution can also be recorded experimentally and used for the evaluation of the numerical results. In the case of interatomic electronic decay processes the products include released electrons and positively charged atoms or molecules. An accurate theoretical description of the product energy distributions requires nuclear dynamics simulations which rely on the potential energy surfaces of the initial and final states of decay as well as electronic decay lifetimes and branching ratios. In specific cases, where an electronic decay process is faster than the nuclear dynamics, a few calculations around the equilibrium geometries approximately reproduce the product distributions sufficiently well.

All electronic structure calculations presented in this work were performed at the *ab initio* level. Since the systems under investigation had a closed shell character in the electronic ground state, Møller-Plesset perturbation theory (MP2) and and coupled cluster approach including single, double and perturbative triple excitations (CCSD(T)) were used for the determination of equilibrium structures. For the computation of the singly and doubly ionized states involved in the electronic decay we employed the Algebraic Diagrammatic Construction (ADC(n)) method complete up to the perturbational order n. Triply ionized states were obtained by the Multi-Reference Configuration Interaction (MRCI) approach. All correlated electronic structure methods we used rely on molecular orbitals and orbital energies calculated by means of the Restricted Hartree-Fock (RHF) approach. The most elaborate task within the present work involved the computation of electronic decay widths of the singly and doubly ionized states. The investigated resonance states belong to the class of Feshbach resonances, the corresponding decay widths were computed by the Fano-ADC-Stieltjes approach utilizing square integrable $\mathcal{L}^2$ basis sets.

This chapter is organized as follows. In the first section we introduce the electronic structure methods for the computation of the neutral and ionized electronic states. In the second section we explain the concept of the electronic resonance and derive the Fano-ADC-Stieltjes method for the computation of the electronic decay widths. All expressions are given in atomic units.

2.1 Ab initio methods for electronic structure calculations

Quantum chemistry deals with the solution of many-body problems in systems consisting of nuclei and electrons. The quantum mechanical description of such a system of M nuclei and N electrons is given by the many-body wavefunction $\Psi(R, r)$ which depends on the sets of coordinates R for the nuclei and r for the electrons. This wavefunction satisfies the Schrödinger equation:

$$\hat{H}_f \Psi(R, r) = E\Psi(R, r). \tag{2.1}$$

The full Hamilton operator $\hat{H}_f$ has the following form:

$$\hat{H}_f = -\frac{1}{2}\sum_A \frac{1}{m_A}\nabla^2_{R,A} - \frac{1}{2}\sum_i \nabla^2_{r,i} - \sum_{iA} \frac{1}{|r_i - R_A|} + \sum_{i<j} \frac{1}{|r_i - r_j|} + \sum_{A<B} \frac{1}{|R_A - R_B|}. \tag{2.2}$$

It includes the kinetic energy operators of the nuclei (first term) and electrons (second term) as well as the potential energy operators describing electron-nuclei, electron-electron and nuclei-nuclei interactions (last three terms), respectively. Here, the indices i and j denote the electrons, the indices A and B the nuclei while the indices m_A denote the nuclear masses.

Due to the different magnitudes of the electron and nuclei masses, the motion of the electrons is assumed to adjust instantaneously to the position of the nuclei (the Born-Oppenheimer approximation [55]). In this case, the total wavefunction $\Psi(R, r)$ can be factorized:

$$\Psi(R, r) = F(R)\Phi(R, r), \tag{2.3}$$

where $F(R)$ denotes the nuclear wavefunction and $\Phi(R, r)$ the so-called adiabatic electronic wavefunction. The latter depends parametrically on the position of the nuclei and satisfies the *electronic* Schrödinger equation:

$$\hat{H}_{el}(R)\Phi(R, r) = E_{el}(R)\Phi(R, r), \tag{2.4}$$

where the corresponding *electronic* Hamiltonian is defined as:

$$\hat{H}_{el}(R) = -\frac{1}{2}\sum_i \nabla^2_i - \sum_{iA} \frac{1}{|r_i - R_A|} + \sum_{i<j} \frac{1}{|r_i - r_j|} + \sum_{A<B} \frac{1}{|R_A - R_B|}. \tag{2.5}$$

For the brevity of notation, in the following we will denote the electronic Hamiltonian as $\hat{H}$. The motion of the nuclei takes place on an adiabatic potential energy surface $E_{el}(R)$, generated by the electrons:

$$\hat{H}_{nuc} F(R) = EF(R), \tag{2.6}$$

$$\hat{H}_{nuc} = -\frac{1}{2}\sum_A \frac{1}{m_A}\nabla^2_{R,A} + E_{el}(R). \tag{2.7}$$

The Born-Oppenheimer approximation is valid only if the energy difference for neighboring adiabatic states is sufficiently large, otherwise the timescales of the electronic and nuclear motions become comparable and the motion of the nuclei may couple the adiabatic electronic states. This phenomenon is assigned as the non-adiabatic coupling and plays an important role for the dynamics of systems where the adiabatic electronic states become quasi-degenerate.

2.1.1 Hartree-Fock approximation

The solution of the electronic Schrödinger equation (2.4) is the central problem of the quantum chemical electronic structure methods. The most primitive description of a system containing N electrons is given by the model of independent electrons. Within this model, the approximate electronic wavefunction $|\Phi_0\rangle$ is a product of one-electron spin orbitals $\chi_i(i)$ accommodating the i-th electron, the so-called Hartree product:

$$|\Phi_0\rangle = \chi_1(1)\chi_2(2)\cdots\chi_N(N), \tag{2.8}$$

Due to the fermionic properties of the electrons, the Hartree product has to be antisymmetrized with respect to electron permutations. The corresponding compact notation is assigned as the Slater determinant [56]:

$$|\Phi_0\rangle = \frac{1}{\sqrt{N!}}\begin{vmatrix} \chi_1(1) & \chi_2(1) & \cdots & \chi_N(1) \\ \chi_1(2) & \chi_2(2) & \cdots & \chi_N(2) \\ \vdots & \vdots & \ddots & \vdots \\ \chi_1(N) & \chi_2(N) & \cdots & \chi_N(N) \end{vmatrix} \tag{2.9}$$

The optimal set of one-electron spin orbitals is defined by the variational solution of the energy functional $\langle\tilde{\Phi}_0|\hat{H}|\tilde{\Phi}_0\rangle$:

$$\delta E = \delta\langle\tilde{\Phi}_0|\hat{H}|\tilde{\Phi}_0\rangle - \delta(\langle\tilde{\Phi}_0|\tilde{\Phi}_0\rangle - 1) = 0, \tag{2.10}$$

where $|\tilde{\Phi}_0\rangle$ is the Slater determinant constructed from a trial set of one-electron spin orbitals. It can be demonstrated that the optimal one-electron spin orbitals are solutions of the so-called Hartree-Fock (HF) equations:

$$\hat{F}\chi_i = \epsilon_i\chi_i, \tag{2.11}$$

$$\langle\chi_i^*|\chi_j\rangle = \delta_{ij}, \tag{2.12}$$

$\hat{F}$ being the Fock operator and ϵ_i the energy of spin orbital χ_i. The Fock operator is a one-particle operator and has the following explicit form:

$$\begin{aligned}\hat{F}(1) = -\frac{1}{2}\nabla_1^2 - \sum_A \frac{Z_A}{r_{1A}} + \sum_{j\neq i}\int \chi_j(2)\frac{1}{|r_1 - r_2|}\chi_j(2)dr_2 \\ - \sum_{j\neq i}\int \chi_j(2)\frac{1}{|r_1 - r_2|}P_{12}\chi_j(2)dr_2,\end{aligned} \tag{2.13}$$

where r_1 and r_2 are the coordinates of the considered electron and one of the remaining electrons in the system, respectively. The first term of the Fock operator denotes the kinetic energy operator of the considered electron, the second term the Coulomb interaction between the considered electron and the nuclei. The third term can be interpreted classically as the interaction between the electron and an averaged Coulomb potential created by the remaining electrons. Finally, the last term has no classical meaning as it contains the operator P_{12} exchanging the electrons one and two. The exchange term appears due to the antisymmetric properties of the electronic wave function.

For an efficient computational implementation of the HF method, aimed to determine solutions of the Fock equations, spin orbitals χ_i are expanded in a finite basis of functions ϕ_μ:

$$\chi_i = \sum_\mu c_{i\mu}\phi_\mu. \tag{2.14}$$

This expansion leads to the HF equations in the matrix form (the Roothaan equations):

$$\mathbf{FC} = \mathbf{SCE}, \tag{2.15}$$

where $\mathbf{F}$ is the representation of the Fock operator in the basis ϕ_μ (the Fock matrix), $\mathbf{C}$ the matrix of spin orbital coefficients and $\mathbf{E}$ the diagonal matrix of orbital energies, respectively. The overlap matrix $\mathbf{S}$ is non-diagonal due to the non-orthonormality of the primary basis ϕ_μ. The Roothaan equations are solved iteratively, converging to a total electronic energy which typically covers a large portion of the exact value.

The difference between the HF total energy E_0^{HF} and the exact energy of the electronic ground state E_0 is termed the correlation energy:

$$E_{corr} = E_0 - E_0^{HF} = \langle\Psi_0|\hat{H}|\Psi_0\rangle - \langle\Phi_0|\hat{H}|\Phi_0\rangle, \tag{2.16}$$

$|\Psi_0\rangle$ being the exact ground state electronic wave function. The correlation energy usually amounts to few percents of the total electronic energy for atoms and molecules at equilibrium geometries [57]. This energy, which is rather large in absolute terms (e.g. 5.9 eV for the water molecule in the cc-pVDZ basis set) appears due to the fact that the Slater determinant $|\Phi_0\rangle$ is not able to describe the correlated motion of the electrons with opposite spins. Therefore, it does not constitute the best solution for the N-electron system. The correlation energy is crucial to accurately describe energetics of chemical reactions, non-covalent interactions etc. Furthermore, correlated electronic wave functions are necessary to obtain accurate properties of the system. Hence, methods including electronic correlation play a prominent role in the electronic structure theory. The main purpose of the HF method is to provide a set of one-electron orbitals and energies, based on which systematic improvement of the electronic wavefunction and the electronic energy can be achieved.

2.1.2 Perturbational approach to the ground state electronic correlation energy

Calculation of electronic correlation energies at a moderate computational cost is provided by the Many-Body Perturbation Theory (MBPT). The basic idea of the MBPT lies in the separation of the full electronic Hamiltionian into an unperturbed contribution $\hat{H}_0$ and a perturbation $\hat{V}$ [57]:

$$\hat{H} = \hat{H}_0 + \lambda\hat{V}, \tag{2.17}$$

the strength of the latter being λ. The exact ground state solution $|\Psi_0\rangle$ satisfies the Schrödinger equation for the full electronic Hamiltionian:

$$(\hat{H}_0 + \lambda\hat{V})|\Psi_0\rangle = E_0|\Psi_0\rangle, \tag{2.18}$$

Assuming that a perturbation is weak (i.e. λ is small), both the ground state $|\Psi_0\rangle$ and the corresponding energy E_0 can be expanded in a Taylor series in λ:

$$|\Psi_0\rangle = |\Psi_0^{(0)}\rangle + \lambda|\Psi_0^{(1)}\rangle + ... + \lambda^n|\Psi_0^{(n)}\rangle \tag{2.19}$$

$$E_0 = E_0^{(0)} + \lambda E_0^{(1)} + ... + \lambda^n E_0^{(n)}, \tag{2.20}$$

where $|\Psi_0^{(0)}\rangle$ and $E_0^{(0)}$ assign the wavefunction and the energy of the unperturbed ground state, respectively. It has to be remarked, that in contrast to variational methods such as the HF approach, the energy calculated to a given perturbational order does not constitute an upper bound to the exact energy. Inserting the expansions 2.19 and 2.20 into the Schrödinger equation 2.18 and equating the λ^n coefficients, the first-order energy correction can be determined:

$$E_0^{(1)} = \langle\Psi_0^{(0)}|\hat{V}|\Psi_0^{(0)}\rangle. \tag{2.21}$$

For the second-order energy correction one obtains:

$$E_0^{(2)} = \langle\Psi_0^{(0)}|\hat{V}|\Psi_0^{(1)}\rangle = \sum_i \frac{|\langle\Psi_0^{(0)}|\hat{V}|\Psi_i^{(0)}\rangle|^2}{E_0^{(0)} - E_i^{(0)}}, \tag{2.22}$$

where $E_i^{(0)}$ is the zeroth-order energy of the unperturbed state $|\Psi_i^{(0)}\rangle$.

According to Møller and Plesset [58] the electronic correlation energy can be obtained utilizing the following partitioning of the electronic Hamiltonian:

$$\hat{V} = \hat{H} - \hat{H}_0 \tag{2.23}$$

$$\hat{H}_0 = \sum_i \hat{F}_i, \tag{2.24}$$

$\hat{F}_i$ being a Fock operator acting on the i-th electron. The unperturbed wave function is given by the Hartree-Fock ground state determinant:

$$|\Psi_0^{(0)}\rangle = |\Phi_0\rangle. \tag{2.25}$$

The correlation energy can be considered as an energy correction appearing due to the small perturbation of the non-correlated wavefunction by electron-electron interactions included in the full electronic Hamiltonian. Within the Møller-Plesset partitioning scheme the sum of the zeroth and first-order energies yields the ground state Hartree-Fock energy:

$$E_0^{(0)} + E_0^{(1)} = \langle\Phi_0|\hat{H}_0 + \hat{V}|\Phi_0\rangle = \langle\Phi_0|\hat{H}|\Phi_0\rangle = E^{HF}. \tag{2.26}$$

Therefore, the second-order correction is the first contribution to the ground state correlation energy:

$$E_0^{(2)} = \sum_{\substack{i<j \\ a<b}} \frac{\langle ij||ab\rangle^2}{\epsilon_i + \epsilon_j - \epsilon_a - \epsilon_b}, \tag{2.27}$$

where the indices i, j belong to the occupied (hole) and a, b to the unoccupied (particle) Hartree-Fock orbitals, respectively. The numerator contains the antisymmetrized two-electron integrals:

$$\langle ij||ab\rangle = \int \chi_i(1)\chi_j(2)\frac{1}{|r_1 - r_2|}(1 - P_{12})\chi_a(1)\chi_b(2)dr_1dr_2. \tag{2.28}$$

The correlation energy recovered by the Møller-Plesset perturbation theory has its physical origin in the correlated motion of electrons, influenced by the mutual repulsive interaction. This type of electronic correlation energy is denoted as *dynamic* correlation energy [57]. The Møller-Plesset correlation energies are size extensive, scaling properly with the size of the system.

As is shown by the Eq. 2.27, the perturbational calculation of the electronic correlation energy involves only integral transformation from the atomic to the molecular orbital basis and summations over the transformed integrals. For higher perturbational orders, however, the product structure of the numerators becomes more complicated, increasing the computational demand. Furthermore, in general, the convergence of a perturbation expansion can not be ensured due to interactions with other unperturbed states [57]. Therefore, it is the lowest order scheme, the Møller-Plesset second-order perturbation theory (MP2), which is the most widely used in practice for the computation of the correlation energies, offering a good compromise between the accuracy and the numerical demand. A general drawback of all methods based on the perturbation theory is the non-variationality of the energy corrections, making these methods unfeasible for high-accuracy electronic structure calculations. In the present work, the MP2 method was utilized to compute non-degenerate closed shell ground state energies and to determine the ground state equilibrium geometries.

2.1.3 Configuration interaction approaches for computation of ionized states

The many-body perturbation theory as formulated in the previous chapter is suited only for computing the electronic ground state of non-degenerate closed shell systems. Strong *static* correlation, i.e. the near degeneracy of electronic configurations [57], is a typical feature of excited and ionized states. A conceptually simple way to treat both static and dynamic correlation effects is given by the Configuration Interaction (CI) methods.

Before discussing the more general Multi-Reference CI (MRCI) method, we will briefly introduce the Single-Reference CI (SRCI) method for computation of ground state properties of closed shell systems. Within this method the ground state electronic wavefunction $|\Psi_0\rangle$is linearly expanded within a basis of electronic configurations $|\Phi_I\rangle$:

$$|\Psi_0\rangle = \sum_I C_{I0}|\Phi_I\rangle \tag{2.29}$$

created by promotion of electrons from the hole (here j,k) into the particle spin orbitals (here a,b,c) of a ground state Hartree-Fock reference $|\Phi_0\rangle$:

$$|\Phi_I\rangle = \hat{C}_I|\Phi_0\rangle. \tag{2.30}$$

$$\hat{C}_I = \{c_a^\dagger c_j, c_a^\dagger c_b^\dagger c_j c_k, c_a^\dagger c_b^\dagger c_j^\dagger c_j c_k c_l, ...\}. \tag{2.31}$$

The coefficients C_{I0} are determined by the variational condition:

$$\delta E = \delta\langle\tilde{\Psi}_0|\hat{H}|\tilde{\Psi}_0\rangle - \delta(\langle\tilde{\Psi}_0|\tilde{\Psi}_0\rangle - 1) = 0, \tag{2.32}$$

where $|\tilde{\Psi}_0\rangle$ is a trial ground state CI wavefunction. In the matrix formulation determining C_{I0} coefficients is equivalent to solving the eigenvalue problem:

$$\mathbf{HC} = \mathbf{EC}, \tag{2.33}$$

where $\mathbf{H}$ is the matrix representation of the Hamiltonian in the $|\Phi_I\rangle$ basis, $\mathbf{C}$ the matrix of coefficients C_{In} and $\mathbf{E}$ the diagonal matrix of the electronic energy eigenvalues $E_n = \langle\Psi_n|\hat{H}|\Psi_n\rangle$. Including all excitations in $\hat{C}_I$ leads to the so called Full CI (FCI) wavefunction, being exact within the given one-electron basis. Due to the $\binom{2K}{N}$ dependence of the configuration space size on the number of electrons N and one-electron basis functions K, FCI is feasible only for systems containing few electrons. Truncation of the excitation level at low values, e.g. at Singles and Doubles (CI-SD) results in a tractable size of the CI problem, recovering a large portion of the correlation energy for ground states of small systems. The truncated CI approaches suffer from the not size-extensive behavior, i.e. the portion of recovered correlation energy does not scale properly with the size of the system.

The truncated single-reference CI schemes are suited for the description of ground state wavefunctions with a high contribution of the reference configuration. Excited and ionized states, which typically exhibit a strong mixing of electronic configurations, require a different construction scheme for the configuration space. Here, we will visualize such a construction scheme for singly ionized states. The wave function of a singly ionized state $|\Psi_n^{N-1}\rangle$ is expanded within a space of ionic configurations $|\Psi_J^{N-1}\rangle$:

$$|\Psi_n^{N-1}\rangle = \sum_{Jn} C_{Jn}|\Phi_J^{N-1}\rangle, \tag{2.34}$$

which are generated by applying the ionization operators $\hat{C}_J$ to the Hartree-Fock ground state reference:

$$|\Phi_J^{N-1}\rangle = \hat{C}_J|\Phi_0\rangle. \tag{2.35}$$

The operators $\hat{C}_J$ can be divided into $1h$(one-hole), $2h1p$ (two-hole one-particle), $3h2p$ (three-hole two-particle) etc. classes of excitations:

$$\hat{C}_J = \{c_k, c_a^\dagger c_k c_l, c_a^\dagger c_b^\dagger c_k c_l c_m, ...;\}. \tag{2.36}$$

The resulting configuration space can be formally classified as MRCI if the manifold of the ionic $1h$ configurations is considered as the so-called reference space, replacing the single reference utilized in the SRCI approach. The higher $2h1p$, $3h2p$, $4h3p$ etc. configurations correspond to single, double, triple excitations from the reference into the virtual space and give rise to the MRCI-S, MRCI-SD, MRCI-SDT etc. schemes. The flexibility of the reference space permits an inclusion of the static correlation effects while the excitations into the virtual space provide a description of the dynamic correlation.

The ionic states are obtained by solving the eigenvalue problem as defined in Eq. 2.33, however, the larger reference space leads to a higher computational demand compared to the SRCI method. Due to the truncation of the excitation levels the MRCI schemes remain not size-extensive, limiting their application to small systems. Nevertheless, the MRCI approach has the advantage of being universal, i.e. the formulation of the CI wavefunction as shown in Eq. 2.34 is applicable to doubly, triply, etc. ionized and excited states. We made use of this property to compute triply ionized states, for which no Green's function based approaches are available.

2.1.4 Green's function approach for computation of the ionized states

For computing ionized (excited) states a particularly efficient approach, with characteristics complementary to those of the CI methods, is given by the electronic propagator. We will introduce the one-particle propagator for ionization in detail, whereas the description of the two-particle propagator for double ionization can be found in the literature [59].

The electronic particle propagator describes the propagation of a particle which is added to the ground state of the system at a time t_1 and is characterized by a specific initial state. Within a basis of one-electron basis functions, the electronic particle propagator, also termed as the many-body Green's function, is given by the following expression [60]:

$$G(t_1, t_2)_{pq} = -i\langle\Psi_0|\hat{T}[c_p(t_1)c_q^\dagger(t_2)]|\Psi_0\rangle, \tag{2.37}$$

where $|\Psi_0\rangle$ denotes the exact electronic ground state of a system containing N electrons and p,q are the indices of one-electron basis functions. The time dependent creation and annihilation operators have the explicit form:

$$c_p(t_1) = e^{i\hat{H}t_1}c_p e^{-i\hat{H}t_1} \tag{2.38}$$

$$c_q^\dagger(t_2) = e^{i\hat{H}t_2}c_q^\dagger e^{-i\hat{H}t_2}, \tag{2.39}$$

$\hat{H}$ being the time-independent electronic Hamiltonian of the many-body system. The Wick's time-ordering operator $\hat{T}$ defines the explicit dependence of the matrix element on the times t_1 and t_2:

$$\hat{T}[a_p(t_1)a_q^\dagger(t_2)] = \theta(t_2 - t_1)a_p(t_1)a_q^\dagger(t_2) - \theta(t_1 - t_2)a_q^\dagger(t_2)a_p(t_1) \tag{2.40}$$

θ being the Heavyside step function. The first (second) term of the one-particle Green's function $G(t_1, t_2)_{pq}$ is equal to the probability amplitude to find a particle (a hole) added at the time t_1 into the orbital χ_p in the orbital χ_q at the time t_2. The fact that a forward propagation ($t_1 < t_2$) of a particle is equivalent to the backward propagation ($t_1 < t_2$) of a hole, is taken into account by the Heavyside step functions in Eq. 2.40. Due to the time-independence of the Hamiltonian the dynamics of the system are defined by the relative time variable $t = t_1 - t_2$. The energy domain representation of the Green's function is obtained via a Fourier transformation of $G(t)_{pq}$:

$$G_{pq}(\omega) = \int_{-\infty}^{\infty} G(t)_{pq}e^{i\omega t}e^{-i\eta t}dt, \tag{2.41}$$

where η is a positive infinitesimal required for the convergence of the integral. The resulting expression contains two contributions:

$$G_{pq}(\omega) = G^{+}_{pq}(\omega) + G^{-}_{pq}(\omega) \tag{2.42}$$

$$G^{+}_{pq}(\omega)_{pq} = \langle \Psi_0 | c_p [\omega + E_0 - H + i\eta]^{-1} c^{\dagger}_q | \Psi_0 \rangle \tag{2.43}$$

$$G^{-}_{pq}(\omega)_{pq} = \langle \Psi_0 | c^{\dagger}_p [\omega - E_0 + H - i\eta]^{-1} c_q | \Psi_0 \rangle, \tag{2.44}$$

describing the attachment (Eq. 2.43) and the detachment (Eq. 2.44) of an electron, respectively. Here, E_0 denotes the energy of the electronic ground state and ω is the energy variable. Inserting complete sets of $(N+1)$ and $(N-1)$ electronic states into the first and second terms of Eq. 2.42, respectively, leads to the so-called spectral representation of the Green's function:

$$G_{pq}(\omega) = \sum_{m \in (N+1)} \frac{X_{pm} X^{*}_{qm}}{\omega - \omega_m + i\eta} + \sum_{n \in (N-1)} \frac{X_{pn} X^{*}_{qn}}{\omega - \omega_n - i\eta}. \tag{2.45}$$

The Green's function has its poles at electron affinities ω_m and ionization potentials ω_n:

$$\omega_m = E^{N+1}_n - E_0, \tag{2.46}$$

$$\omega_n = E^{N-1}_n - E_0. \tag{2.47}$$

The squares of the associated transition amplitudes:

$$X^{*}_{pm} = \langle \Psi^{N+1}_m | c^{\dagger}_p | \Psi_0 \rangle \tag{2.48}$$

$$X_{pn} = \langle \Psi^{N-1}_n | c_p | \Psi_0 \rangle \tag{2.49}$$

contribute to the relative strengths of the electron attachement and detachement transitions:

$$T^{(m)} = \sum_p |X_{pm}|^2. \tag{2.50}$$

$$T^{(n)} = \sum_p |X_{pn}|^2. \tag{2.51}$$

from the ground state $|\Psi^N_0\rangle$ to the anionic state $|\Psi^{N+1}_m\rangle$ and the cationic state $|\Psi^{N-1}_n\rangle$, respectively. The expression 2.45 reads in matrix formulation as:

$$\mathbf{G}(\omega) = \mathbf{X}^{\dagger}(\omega \mathbf{1} - \mathbf{\Omega})\mathbf{X}, \tag{2.52}$$

where $\mathbf{\Omega}$ is the diagonal matrix of the ionization energies and electron affinities. The construction of the exact Green's function requires explicit knowledge of the electronic many-body interactions in the neutral and charged states of the system and is thus equivalent to the exact solution of the corresponding electronic Schrödinger equations. In analogy to the Schrödinger equation, a perturbational expansion of the Green's function leads to approximate solutions for the ionization energies and electron affinities as well as transition amplitudes.

The perturbational non-Dyson Algebraic Diagrammatic Construction (ADC) scheme for the one-particle Green's function [61,62] decouples the ionization and electron attachment contributions, allowing separate treatments of both. In the following discussion we will focus on the ionization contribution, the mathematical description of the attachement contribution being analogous. Within the non-Dyson ADC scheme the ionization part of the one-particle Green's function is represented in the following way:

$$\mathbf{G}^{-}(\omega) = \mathbf{F}^{\dagger}(\omega\mathbf{1} - \mathbf{K} - \mathbf{C})\mathbf{F}, \tag{2.53}$$

where $\mathbf{K} + \mathbf{C}$ is the non-diagonal effective interaction matrix and $\mathbf{F}$ the matrix of effective transition amplitudes:

$$F_{pJ} = \langle \tilde{\Psi}_J | c_p | \Psi_0 \rangle. \tag{2.54}$$

The representation of the Green's function as shown in the Eq. 2.53 is assigned as the Intermediate State Representation (ISR) [63]. The basis of "intermediate states" $|\tilde{\Psi}_J^{N-1}\rangle$ is constructed by the orthonormalization of the correlated excited states $|\Psi_J\rangle$:

$$|\Psi_J\rangle = \hat{C}_J |\Psi_0\rangle, \tag{2.55}$$

$$\hat{C}_J = \{c_k, c_a^{\dagger} c_k c_l, c_a^{\dagger} c_b^{\dagger} c_k c_l c_m, ...;\}, \tag{2.56}$$

i,j,k denoting the indices of the occupied and a,b,c of the virtual orbitals, respectively. The correlated excited states include $1h$ (one-hole), $2h1p$ (two-hole one-particle), $3h2p$ (three-hole two-particle) etc. excitation classes. In the recursive orthogonalization procedure, the correlated excited states belonging to an excitation class $[J]$ are first orthogonalized to intermediate states $|\tilde{\Psi}_K\rangle$ of lower excitation classes $[K] < [J]$ in a Gram-Schmidt procedure:

$$|\Psi_J^{\#}\rangle = |\Psi_J\rangle - \sum_K |\tilde{\Psi}_K\rangle\langle\tilde{\Psi}_K|\Psi_J^{\#}\rangle. \tag{2.57}$$

In the next step the precursor states $|\Psi_J^{\#}\rangle$ are orthonormalized within the excitation class $[J]$:

$$|\tilde{\Psi}_J\rangle = \sum_{J'} |\Psi_{J'}^{\#}\rangle (\rho^{\#-\frac{1}{2}})_{J'J}, \tag{2.58}$$

$$\rho_{J'J}^{\#} = \langle \Psi_{J'}^{\#} | \Psi_J^{\#} \rangle. \tag{2.59}$$

In contrast to CI approaches, where the operators $\hat{C}_J$ are applied to the uncorrelated ground state of the system, the intermediate states are in general not equivalent to the $1h$, $2h1p$, $3h2p$ etc. configurations but rather are linear combinations of these, depending on the level of description of the correlated ground state $|\Psi_0\rangle$. The intermediate states include correlation effects which are present in the neutral ground state and which are expected to be modified only weakly by the removal of an electron. Therefore, the level of the correlation description at a given excitation class is higher for intermediate states than for CI configurations.
The solution of the eigenvalue problem for the effective interaction matrix $\mathbf{K} + \mathbf{C}$:

$$(\mathbf{K} + \mathbf{C})\mathbf{Y} = \mathbf{Y}\mathbf{\Omega}, \ \mathbf{Y}^{\dagger}\mathbf{Y} = \mathbf{1} \tag{2.60}$$

delivers the ionization potentials ω_n, the corresponding eigenvectors transform the effective transition amplitudes into the transition amplitudes X_{pn} via:

$$X_{pn} = \sum_J Y^*_{Jn} F_{pJ}. \tag{2.61}$$

The ADC schemes used in this work rely on the Möller-Plesset partitioning of the electronic Hamiltonian (see Eq. 2.24), expanding both the $\mathbf{K} + \mathbf{C}$ and $\mathbf{F}$ matrices up to the perturbational order n:

$$\mathbf{K} + \mathbf{C} = \mathbf{K} + \mathbf{C^1} + \mathbf{C^2} + ... + \mathbf{C^n} \tag{2.62}$$

$$\mathbf{F} = \mathbf{F^0} + \mathbf{F^1} + \mathbf{F^2} + ... + \mathbf{F^n}. \tag{2.63}$$

The expansion space is augmented by a $(n/2+1)h(n/2)p$ excitation class at each even order n. Hence, both the ADC(2) and the ADC(3) schemes, used throughout the present work, require only $1h$ and $2h1p$ excitation classes. The explicit expressions for the expansions of the effective interaction matrix elements and the effective transition amplitudes are obtained by comparison with the diagrammatic series for $\mathbf{G}^-$. It must be remarked that the complexity of the expressions defining the ADC matrix elements increases noticeably with the growing maximum perturbational order n.

The ADC(n) approaches for computation of ionization energies combines a Hermitian eigenvalue problem with the perturbational expansion of the matrix elements, leading to the favorable characteristics of *size-consistency* and *compactness*. The size-consistency ensures that ionizations occurring at a constituent of the system are decoupled from the excitations on other constituents if there are no interactions with the latter. Due to the compactness property, the maximum excitation class required for a consistent treatment of the ionized states at a given order n is smaller than the corresponding configuration interaction excitation class. Therefore, the computational demand for storing and diagonalizing the interaction matrix is substantially reduced in the case of the ADC approach. Both characteristics are crucial for the ADC(n) approaches to be applicable to medium size systems. The most essential drawback of the ADC(n) methods is the restriction to systems with single-determinant character of the neutral electronic ground state. Furthermore, relying on a perturbational expansion scheme, the ADC ionization energies typically do not converge smoothly with the growing perturbational order but rather exhibit an oscillatory behavior [62]. In the present work ADC(n) methods were used for the computation of single and double ionization energies as well as for constructing the bound and continuum components of the resonance wave functions (see chapter 2.2.2).

2.2 Ab initio methods for computation of electronic decay widths

2.2.1 Fano approach to electronic resonance widths

Resonance phenomena play an important role in the field of scattering physics, describing enhancement of scattering cross sections at specific energy values of the scattered

particles [64]. Thus, an incoming particle (e.g. an electron) is temporarily captured by the target (e.g. an atom) in a metastable state, assigned as a *resonance*. After a characteristic time, the metastable state decays, releasing a particle into the continuum again.

According to the mechanism of their occurrence, the majority of the resonances can be classified either as shape or as Feshbach resonances [65], which we will visualize for the case of the electron scattering. The electronic shape resonances occur due to the temporary capture of an electron in a potential with a barrier, e.g. a centrifugal barrier. The energy of the captured electron is typically lower than the barrier height, therefore the electron leaves the potential via the tunneling mechanism. Feshbach electronic resonances occur due to the coupling of the incoming electron to a bound state of the target via electron-electron interactions. The emission of the captured electron from a Feshbach resonance proceeds via the autoionization mechanism.

The electronic resonances can be populated not only in an electron scattering process but furthermore by optical excitations of a compound system consisting of the target with an additional electron. In the present work, we investigate metastable electronic states formed by photoionization and decaying via two-electron autoionization mechanisms such as Auger decay, ICD and ETMD. According to the criteria mentioned above these metastable states belong to the class of Feshbach resonances.

An important characteristic of a resonance state is the so-called resonance width Γ. As we will demonstrate in the following, it is directly related to the lifetime of the resonance state and determines the timescale of electronic decay in the systems considered in this work. A formulation of the resonance width in terms of a configuration interaction scheme was given by Fano [66]. The corresponding resonance wave function $|\Phi_E\rangle$ is obtained by solving the electronic Schrödinger equation:

$$\hat{H}|\Psi_E\rangle = E|\Psi_E\rangle. \tag{2.64}$$

The underlying basis for the construction of the resonance wavefunction comprises zeroth order states with bound ($|\Phi\rangle$) and continuum ($|\Psi_{E'}\rangle$) properties:

$$\langle\Phi|\hat{H}|\Phi\rangle = E_\Phi \tag{2.65}$$

$$\langle\Psi_{E'}|\hat{H}|\Psi_{E''}\rangle = E'\delta(E' - E''). \tag{2.66}$$

At large separations from the bound component the continuum components $|\Psi_{E'}\rangle$ represent unperturbed scattering states. The electronic Hamiltonian $\hat{H}$ introduces a coupling between the bound and continuum components:

$$\langle\Phi|\hat{H}|\Psi_{E'}\rangle = V_{E'} \tag{2.67}$$

In a specific case, where only one bound component $|\Phi\rangle$ and one continuum configuration $|\Psi_{E'}\rangle$ are present, the resonance wave function has the following explicit form:

$$|\Psi_E\rangle = a(E)|\Phi\rangle + \int b_{E'}(E)|\Psi_{E'}\rangle \, dE'. \tag{2.68}$$

The coefficients $a(E)$, $b_{E'}(E)$ as well as the resonance energy E can be determined by a solving the following system of equations:

$$E_\Phi a(E) + \int V^*_{E'} b_{E'}(E) \, dE' = Ea(E) \tag{2.69}$$

$$V_{E'}a(E) + E'b_{E'}(E) = Eb_{E'}(E). \tag{2.70}$$

These equations are constructed by the scalar multiplication of the $\langle\Phi|\hat{H}$ and $\langle\Psi_{E'}|\hat{H}$ vectors with the resonance wave function (2.68). For the determination of the coefficient $a(E)$ it is sufficient to rely on the normalization condition of the resonance wavefunction:

$$\langle\Psi_{\bar{E}}|\Psi_E\rangle = a^*(\bar{E})a(E) + \int b^*_{E'}(\bar{E})b_{E'}(E)\ dE' = \delta(\bar{E} - E) \tag{2.71}$$

and to insert for $b_{E'}$ the solution of Eq. 2.70:

$$b_{E'} = [\frac{1}{E - E'} + z(E)\delta(E - E')]V_{E'}a. \tag{2.72}$$

Here, the formal Dirac solution [67] for $b_{E'}$ is used due to the singularity appearing at $E = E'$. The factor $z(E)$ has to be chosen according to the desired boundary condition (e.g. $z(E) = i\pi$ in the case of scattering problems). The explicit normalization condition (2.71) reads as:

$$\begin{aligned}\langle\Psi_{\bar{E}}|\Psi_E\rangle =& a^*(\bar{E})a(E)(1 + \int [\frac{1}{\bar{E} - E'} + z(\bar{E})\delta(\bar{E} - E')] \\ & * [\frac{1}{E - E'} + z(E)\delta(E - E')]\,|V_{E'}|^2\ dE' = \delta(\bar{E} - E).\end{aligned} \tag{2.73}$$

Following form of the coefficient $a(E)$ can be shown to satisfy this normalization condition:

$$|a(E)|^2 = \frac{|V_E|^2}{(E - (E_\Phi + \Delta(E)))^2 + \pi^2\,|V_E|^4}, \tag{2.74}$$

where the $\Delta(E)$ denotes the energy shift of the bound component energy due to the interaction with the continuum:

$$\Delta(E) = P\int \frac{|V'_E|^2}{E - E'}\ dE'. \tag{2.75}$$

The symbol P denotes the principal value of the corresponding integral. Assuming a slow variation of V_E with the energy E in the vicinity of the resonance, a simple interpretation of the expression 2.74 is possible. In the energy domain the interaction with the continuum transforms the discrete state $|\Phi\rangle$ into a continuous Lorentzian distribution with the maximum located at $E_{res} = E_\Phi + \Delta(E)$ and the width Γ defined as follows:

$$\Gamma = 2\pi\,|V_E|^2\,. \tag{2.76}$$

In the time domain, the originally bound state $|\Phi\rangle$ would decay exponentially, the decay lifetime being:

$$\tau = \frac{1}{\Gamma}. \tag{2.77}$$

In a general case, the continuum subspace contains more than one zeroth order state, therefore the specific definition of the decay width given in Eq. 2.76 has to be modified:

$$\Gamma = 2\pi\sum_f \left|\langle\Phi|\hat{H}|\chi_{fE}\rangle\right|^2. \tag{2.78}$$

The state $|\chi_{fE}\rangle$ denotes the decay channel f belonging to the continuum subspace, which is assumed to be diagonal:

$$\langle\chi_{fE}|\hat{H}|\chi_{gE'}\rangle = E\delta_{fg}\delta(E-E'). \tag{2.79}$$

Calculation of decay widths according to the Fano approach involves explicit construction of continuum functions χ_{fE}. In contrast, the majority of the numerical electronic structure methods rely on square integral basis sets. Therefore, numerous approaches were introduced to adapt such methods for the computation of resonance widths [19]. Among the most prominent, the complex scaling approach transforms the electronic Schrödinger equation into the coordinates $r' = re^{i\theta}$, in which the resonance wave function is square integrable [68]. The same goal can be achieved by augmenting the electronic Hamiltonian by a Complex Absorbing Potential (CAP) [69,70]. Both approaches comprise a parameter such as the scaling angle or the strength of the CAP which requires an optimization via repeated numerical calculations.

It is evident from the Fano formula (Eq. 2.78) that the electronic interaction of the bound component with the continuum is non-vanishing only in a restricted region of space, given by the extension of the bound state. Therefore, in a decay width calculation the continuum component needs to be properly described only in this interaction region. This can be achieved by an expansion of the continuum component within a basis of so-called discretized continuum states [71], available in standard electronic structure methods (CI, ADC etc.) dealing with square integrable basis sets. Compared to complex scaling or CAP approaches such an implementation of the Fano method is computationally less demanding since it does not involve an optimization of the internal parameter.

2.2.2 Construction of the resonance components by the ADC scheme

In the present work, the method of choice for constructing the disretized continuum and the bound component of the resonance is the ADC approach implemented for $\mathcal{L}^2$ electronic basis sets. The basic idea lies in the separation of the available set of $1h$, $2h1p$ etc. intermediate states into the continuum subspace $\mathcal{P}$, comprising final states of decay and the subspace $\mathcal{Q}$, comprising bound components:

$$\mathcal{P} + \mathcal{Q} = 1. \tag{2.80}$$

More specifically, the projection of the ADC Hamiltonian onto these subspaces yields interaction matrices $P\hat{H}P$ and $Q\hat{H}Q$, which after diagonalization deliver the bound component $|\Phi_b\rangle$ and a set of pseudocontinuum states $|\tilde{\chi_j}\rangle$, respectively. The diagonalization of $Q\hat{H}Q$ furthermore provides the energy expectation value E_Φ of the bound component required to calculate the exact resonance energy $E_{res} = E_\Phi + \Delta(E)$. In the present work the approximation $E_{res}{\approx}E_\Phi$ is made since the energy shift $\Delta(E)$ is expected to be smaller than the error of E_Φ within the ADC approach.

The adaptation of the ADC approach for the construction of the $\mathcal{P}$ and $\mathcal{Q}$ subspaces will be exemplified for the ICD of singly ionized states. The corresponding definitions for the doubly ionized decaying states are analogous and can be found in the literature [21].

In a typical weakly bound dimer AB without inversion symmetry the initial state of ICD is characterized by a hole in the inner-valence orbital iv_A of A while in the final state the holes are located in the outer-valence orbitals ov_A of A and ov_B of B:

$$A^+(iv_A^{-1})B \rightarrow A^+(ov_A^{-1})B^+(ov_B^{-1}) + e_{ICD}. \tag{2.81}$$

In the hierarchy of the ADC(n) schemes, the excitation classes required for the construction of the resonance components are available already at the ADC(2) level. As was demonstrated in the chapter 2.1.4, this level includes $1h$ and $2h1p$ excitation classes. By applying $c_p^\dagger c_{ov_A} c_{ov_B}$ excitation operators to the neutral electronic ground state $|\Psi_N^0\rangle$, intermediate states $|\tilde{\Psi}_I^{N-1}\rangle$ are constructed:

$$|\tilde{\Psi}_I^{N-1}\rangle = \hat{C}_I|\Psi_N^0\rangle = c_p^\dagger c_{ov_A} c_{ov_B}|\Psi_N^0\rangle, \tag{2.82}$$

which mimic open ICD channels in the presence of a continuum electron by accommodating the holes in the valence orbitals ov_A, ov_B and an electron in the virtual orbital p. These states define the $\mathcal{P}$ subspace [20]. The initial subspace is constructed applying local excitation operators c_{k_A} and $c_p^\dagger c_{k_A} c_{l_A}$ to $|\Psi_N^0\rangle$, where k_A, l_A denote hole orbitals localized on A and p a virtual orbital. The inclusion of the local $2h1p$ configurations is meant to describe intraatomic relaxation and correlation effects in the initial state of ICD. The described method allows a straightforward construction of the initial and final subspaces, however, it can not be used if the states involved in the electronic decay are delocalized due to small distances between A and B or due to inversion symmetry, e.g. in homonuclear diatomics [53].

The procedure for the construction of the $\mathcal{Q}$ and $\mathcal{P}$ subspaces used in the present work is based on the energy criterion for the open decay channels rather than on the less strictly defined localization of molecular orbitals. The central assumption behind this construction scheme is that the ordering of states within a $2h1p$ spectrum of the final states for a fixed particle p reproduces the ordering within the $2h$ spectrum in the same orbital space. Before the actual decay width calculation is performed, the number of open decay channels n_{open} for each irreducible representation is determined in preliminary *ab initio* calculations. Holding a particle index p and varying the hole indices, a subset of intermediate states can be obtained. Using the ADC(2x) scheme, a first order interaction within a subset is introduced. The diagonalization of the interaction matrix yields so-called *adapted* states $|\Theta_J^{(p)}\rangle$:

$$|\Theta_J^{(p)}\rangle = \sum_J c_{IJ}|\tilde{\Psi}_I^{N-1}\rangle. \tag{2.83}$$

The lowest n_{open} adapted states are expected to represent the open decay channels and are added to the $\mathcal{P}$ subspace. The remaining adapted states as well as the $1h$ intermediate states represent closed decay channels and bound states, respectively, and belong to the $\mathcal{Q}$ subspace. This procedure is repeated for all particles p. Compared to the construction scheme based on the spatial characteristics of the intermediate states, the scheme based on the energetic criteria is more general and permits a proper definition of decay channels in systems with high symmetry by means of adapted states.

2.2.3 Renormalization of the discretized ADC continuum by the Stieljtes imaging technique

The pseudocontinuum states $|\tilde{\chi}_j\rangle$ constructed by the ADC scheme implemented for $\mathcal{L}^2$ electronic basis sets can not be directly inserted into the Fano formula for the decay width (2.78). This can be deduced from the normalization conditions:

$$\langle \chi_{iE} | \chi_{jE'} \rangle = \delta_{ij} \delta(E - E'), \tag{2.84}$$

$$\langle \tilde{\chi}_i | \tilde{\chi}_j \rangle = \delta_{ij}, \tag{2.85}$$

indicating that the pseudocontinuum states $|\tilde{\chi}_j\rangle$ need to be renormalized to gain proper amplitude and dimensionality.
The decay width $\Gamma(E)$ in Fano's formulation is a matrix element (see Eq. 2.78) non-vanishing only in the region where the bound component $|\Phi_b\rangle$ is located. In this region the discrete pseudocontinuum function $|\tilde{\chi}_j\rangle$ reproduces the true continuum function $|\chi_{fE_j}\rangle$ apart from a normalization factor. Therefore, the pseudocontinuum couplings $\tilde{\gamma}_j$ and energies $\tilde{E}_j$:

$$\tilde{\gamma}_j = 2\pi \left| \langle \Phi_b | Q \hat{H} P | \tilde{\chi}_j \rangle \right|^2 \tag{2.86}$$

$$\tilde{E}_j = \langle \tilde{\chi}_j | P \hat{H} P | \tilde{\chi}_j \rangle \tag{2.87}$$

can be used to construct an approximate cumulative function $\tilde{G}(E)$ of the decay rate $\Gamma(E)$ [72]:

$$\tilde{G}(E) = \sum_{j=1}^{N} \tilde{\gamma}_j \approx \int_a^b \Gamma(E)\, dE,\ a < E_j < b \tag{2.88}$$

N being the size of the $\mathcal{P}$ subspace. The cumulative function $\tilde{G}(E)$ has a staircase like behavior with the points of increase located at energies $\tilde{E}_j$:

$$\tilde{G}(E) = \begin{cases} 0, E < \tilde{E}_1 \\ \sum_{j=1}^{k} \tilde{\gamma}_j,\ \tilde{E}_k < E < \tilde{E}_{k+1} \\ \sum_{j=1}^{N} \tilde{\gamma}_j,\ \tilde{E}_N < E. \end{cases} \tag{2.89}$$

A regularized version of $\tilde{G}(E)$ can be obtained by defining its value at the points of increase $\tilde{E}_j$ as the average of two neighboring values:

$$\tilde{G}(\tilde{E}_j) = \frac{1}{2}(\tilde{G}(\tilde{E}_{j-1}) + \tilde{G}(\tilde{E}_{j+1})). \tag{2.90}$$

The regularized cumulative function can be differentiated numerically to yield the approximate decay rate function $\tilde{\Gamma}(E)$ at the midpoints of the stairs $\bar{E}_j$:

$$\bar{E}_j = \frac{1}{2}(\tilde{E}_j + \tilde{E}_{j+1}), \tag{2.91}$$

if the $\tilde{G}(\tilde{E}_j)$ values are connected by straight lines:

$$\tilde{\Gamma}(\bar{E}_j) = \frac{1}{2} \frac{\tilde{G}(\tilde{E}_{j+1}) - \tilde{G}(\tilde{E}_j)}{\tilde{E}_{j+1} - \tilde{E}_j} = \frac{1}{2} \frac{\tilde{\gamma}_j + \tilde{\gamma}_{j+1}}{\tilde{E}_{j+1} - \tilde{E}_j}. \tag{2.92}$$

This operation, assigned as the Stieltjes differentiation, renormalizes the pseudocoupling $\tilde{\gamma}_j$ by taking into account the density of pseudocontinuum states in the corresponding spectral region. The continuous $\tilde{\Gamma}(E)$ function, which can be obtained by a subsequent interpolation, however, is sensitive to the electronic basis set and often exhibits a non-regular behavior [72]. Relying on the lowest $2n$ moments of the decay rate function:

$$S(k) = \int_0^\infty E^k \Gamma(E)\ dE \approx \sum_j^N \tilde{E}_j^k \tilde{\gamma}_j,\ k = 0, 1, 2, ..., 2n\ , \tag{2.93}$$

a different, so-called *principal* set containing n pairs of couplings g_i and energies E_i can be determined [71]. It has to be remarked that in the calculation of ionization cross sections and decay rates only negative moments can be used since the positive moments of the atomic ionization cross sections for $k > 2$ are known to diverge [73]. The corresponding cumulative function $G(E)$:

$$G(E) = \sum_{i=1}^{n} g_i(E_i) \approx \int_a^b \Gamma(E)\ dE,\ a < E_i < b \tag{2.94}$$

has a regular shape and can be systematically improved using principal sets of increasing order n. The inclusion of the lowest moments only, which exhibit a quick convergence with the size of the electronic basis set [74], eliminates the strong dependence of the cumulative function on the electronic basis.

The principal energies and couplings are computed using auxiliary polynomials $Q_n(1/E)$ of order n [75]:

$$Q_n(1/E) = \sum_{i=0}^{n} Q_i^n (\frac{1}{E})^i, \tag{2.95}$$

where Q_i^n are the polynomial coefficients. The polynomials $Q_n(1/E)$ are orthogonal to the decay rate function $\Gamma(E)$:

$$\int_a^b Q_n(1/E) Q_m(1/E) \Gamma(E)\ dE = N_n \delta_{nm}, \tag{2.96}$$

the normalization constant N_n chosen in such a way that $Q_n^n = 1$. The corresponding principal energies and couplings are found according to:

$$Q_n(1/E_i) = 0 \tag{2.97}$$

$$g_i^n = \sum_{m=0}^{n-1} [\frac{(Q_m(\frac{1}{E_i}))^2}{N_m}]^{-1}. \tag{2.98}$$

The polynomials Q_n are generated recursively:

$$Q_n(1/E) = (\frac{1}{E} - a_n) Q_{n-1}(1/E) - b_{n-1} Q_{n-2}(1/E) \tag{2.99}$$

with the lowest order functions defined as:

$$Q_0(1/E) = 1;\quad Q_1(1/E) = \frac{1}{E} - a_1. \tag{2.100}$$

The recurrent coefficients a_n and b_{n-1} are given by:

$$a_n = \frac{1}{b_0 b_1 ... b_{n-1}} \int (\frac{1}{E})^n Q_{n-1}(1/E)\Gamma(E)\ dE - \sum_{l=1}^{n-1} a_l, \tag{2.101}$$

$$b_{n-1} = \frac{1}{b_0 b_1 ... b_{n-2}} \int (\frac{1}{E})^{n-1} Q_{n-1}(1/E)\Gamma(E)\ dE = \frac{N_{n-1}}{N_{n-2}}. \tag{2.102}$$

The integrals appearing on the right side can be reformulated inserting the expansion (2.95):

$$\begin{aligned} \int (\frac{1}{E})^{n-1} Q_{n-1}(1/E)\Gamma(E)\ dE &= \int (\frac{1}{E})^{n-1} \sum_{i=0}^{n-1} Q_{n-1}^i (\frac{1}{E})^i \Gamma(E)\ dE \\ &= \sum_{i=0}^{n-1} Q_{n-1}^i \int (\frac{1}{E})^{n+i-1} \Gamma(E)\ dE. \end{aligned} \tag{2.103}$$

The approximate moments (2.93) can be used to replace the resulting simplified integral, yielding after reordering a discrete representation:

$$\int (\frac{1}{E})^{n-1} Q_{n-1}(1/E)\Gamma(E)\ dE = \sum_{j}^{N} (\frac{1}{\tilde{E}_j})^{n-1} Q_{n-1}(1/E_j)\tilde{\gamma}_j \tag{2.104}$$

involving the pseudocontinuum energies and couplings. The corresponding representations of the recurrent coefficients are:

$$a_n = \frac{1}{b_0 b_1 ... b_{n-1}} \sum_{j}^{N} (\frac{1}{\tilde{E}_j})^n Q_{n-1}(1/E_j)\tilde{\gamma}_j - \sum_{l=1}^{n-1} a_l, \tag{2.105}$$

$$b_{n-1} = \frac{1}{b_0 b_1 ... b_{n-2}} \sum_{j}^{N} (\frac{1}{\tilde{E}_j})^{n-1} Q_{n-1}(1/E_j)\tilde{\gamma}_j. \tag{2.106}$$

The recursive scheme (2.99) can be reformulated by defining a modified set of polynomials $R_n(1/E)$:

$$R_n(1/E) = \frac{(-1)^n Q_n(1/E)}{\sqrt{N_n}} \tag{2.107}$$

$$(\frac{1}{E}) R_{n-1}(1/E) = -\sqrt{b_n} R_n(1/E) + a_n R_{n-1}(1/E) - \sqrt{b_{n-1}} R_{n-2}(1/E). \tag{2.108}$$

This recursive scheme can be translated into the eigenvalue problem:

$$\mathbf{CR} = \mathbf{E^{-1}R}, \tag{2.109}$$

the tridiagonal matrix $\mathbf{C}$ containing the recurrent coefficients and diagonal matrix $\mathbf{E}$ the principal energies E_i^n. The principal couplings are calculated using the eigenvectors R:

$$g_i^n = (R_{0i}^n)^2. \tag{2.110}$$

A Stieltjes derivative of the cumulative function $G^n(E)$ finally returns the nth order approximation to the decay rate $\Gamma(E)$ at the midpoints of the "stairs" $\bar{E}_i^n$:

$$\Gamma^n(\bar{E}_i^n) = \frac{1}{2}\frac{g_i^n + g_{i+1}^n}{E_{i+1}^n - E_i^n}. \tag{2.111}$$

The joint numerical approach for calculating electronic decay widths relying on the Fano formalism and the renormalization of the ADC pseudocontinuum by the Stieltjes imaging technique is assigned as the Fano-ADC-Stieljtes approach.

The convergence of the $\Gamma^n(E)$ function with the increasing order n results from the specific characterictics of the cumulative function $G^n(E)$, satisfying the so-called Chebyshev inequalities:

$$G^n(E_i - 0) < G^{n+1}(E_i - 0) \leq G^{n+1}(E_i + 0) < G^n(E_i + 0). \tag{2.112}$$

Here, the energies $E_i \pm 0$ assign the limits from above (below), relatively to the abscissa E_i. With the increasing order the $G^n(E)$ function converges to a limit, given by the inifinite order n. Furthermore, the limits $E \pm 0$ of $G^n(E)$ bracket the true $G(E)$ function at the points of increase E_i.

The analytical convergence behavior of the $G^n(E)$ function can not be fully exploited in numerical computations. The limited precision causes increasing errors at high Stieltjes orders as the substraction of large numbers is involved in the calculation of recurrence coefficients. Therefore, the convergence of the numerical results has to be analyzed to find optimal range of Stieltjes orders, typically lying at n<20 for quadruple precision.

2.2.4 Calculation of partial decay widths by the Fano-ADC-Stieltjes method

Total electronic decay widths contain information about the timescale of the decay and allow to estimate its efficiency relative to alternative relaxation processes. The computation of *partial* decay widths (see Eq. 2.78), describing decay into individual channels, is crucial for determining the branching ratios of the decay and hence the distribution of the products (electrons and ionic species).

A true decay channel is defined by a set of quantum numbers, fully characterizing the state of the system including the ionic core and the continuum electron after the decay has happened. The determination of the corresponding partial widths is not possible within the Fano-Stieljtes-ADC approach since the pseudocontinuum states $|\Theta_J^{(p)}\rangle$ are not identical to true continuum functions. In the present work we are interested in the state of the ionic core, which can be associated with electronic decay mechanisms. For instance, in a singly ionized heteronuclear dimer AB the holes are located on both monomers in the final state of ICD while in the final state of ETMD they are located on B:

$$A^+(iv_A^{-1})B \rightarrow A^+(ov_A^{-1})B^+(ov_B^{-1}) + e_{ICD}, \tag{2.113}$$

$$A^+(iv_A^{-1})B \rightarrow AB^{2+}(ov_B^{-2}) + e_{ETMD}. \tag{2.114}$$

To determine the partial widths associated with different decay mechanisms, we use an *ad hoc* scheme based on approximate channel projectors [20] in conjunction with the

Fano-ADC-Stieltjes method. Within this scheme the total final subspace is represented as

$$\mathcal{P} = \sum_f \mathcal{P}_f, \tag{2.115}$$

where $\mathcal{P}_f$ is a projector on the channel f. The partial widths are obtained from the auxiliary quantities

$$\tilde{\gamma}_j^f = 2\pi |\langle \Phi_b | Q H_{el} P_f | \tilde{\chi}_j \rangle|^2. \tag{2.116}$$

similarly to the case of the total width. The construction scheme of the projectors P_f will be visualized for the electronic decay of singly ionized states.
In constructing the projector operators P_f we rely on the fact that the intermediate states spanning the subspace $\mathcal{P}$ are just the $2h1p$ configuration state functions. Thus, a Hamiltonian matrix is built within the basis of $2h$ configurations

$$|\Phi_L^{N-2}\rangle = C_L |\Phi_0\rangle = c_k c_l |\Phi_0\rangle, \tag{2.117}$$

whose diagonalization yields a set of doubly ionized states

$$|\tilde{\Phi}_f^{N-2}\rangle = \sum_L c_{fL} |\Phi_L^{N-2}\rangle. \tag{2.118}$$

Different decay channels can be clearly identified among the $|\tilde{\Phi}_f^{N-2}\rangle$ states. A discretized representation of a scattering state corresponding to the open decay channel f is then obtained in the following series of steps. First, a continuum electron is added to a virtual orbital p:

$$|\tilde{\Phi}_{p,f}^{N-1}\rangle = c_p^\dagger |\tilde{\Phi}_f^{N-2}\rangle. \tag{2.119}$$

Second, the $2h1p$ states $|\tilde{\Phi}_{p,f}^{N-1}\rangle$ are orthogonalized relative to the bound component Φ_b

$$|\bar{\Phi}_{p,f}^{N-1}\rangle = |\tilde{\Phi}_{p,f}^{N-1}\rangle - |\Phi_b\rangle\langle\check{\Phi}_{p,f}^{N-1}|\Phi_b\rangle, \tag{2.120}$$

yielding a set of states $|\bar{\Phi}_{p,f}^{N-1}\rangle$. Finally, the latter are further orthonormalized among themselves by a symmetric orthonormalization procedure:

$$|\bar{\Psi}_{p,f}^{N-1}\rangle = \sum_{p'} |\bar{\Phi}_{p',f}^{N-1}\rangle (\rho^{-\frac{1}{2}})_{p'p} \tag{2.121}$$

$$\rho_{p',p} = \langle \bar{\Phi}_{p',f}^{N-1} | \bar{\Phi}_{p,f}^{N-1} \rangle. \tag{2.122}$$

The $2h1p$ states $|\bar{\Psi}_{p,f}^{N-1}\rangle$ are used to construct the projector onto the channel f:

$$P_f = \sum_p |\bar{\Psi}_{p,f}^{N-1}\rangle\langle\bar{\Psi}_{p,f}^{N-1}|. \tag{2.123}$$

Separate computations of decay widths for each of the channels introduce numerical errors, requiring a renormalization of the partial widths Γ_f with respect to the total width:

$$\Gamma_f^r = \frac{\sum_f \Gamma_f}{\Gamma}. \tag{2.124}$$

3 Computational details

3.1 He·Mg

3.1.1 Energetics of the electronic decay

The He·Mg ground state potential energy curve has been computed by the coupled-cluster method including singles, doubles and perturbative triples (CCSD(T)) as implemented in the MOLPRO 2010.1 quantum chemistry package [76]. Aug-cc-pVQZ basis sets [77, 78] at the atomic centers plus additional 3 s-type, 3 p-type, 2 d-type, 2 f-type, 1 g-type ($3s3p2d2f1g$) mid-bond basis functions were utilized for an improved description of electronic density between the atoms [79]. The vibrational wavefunction in the electronic ground state of He·Mg was obtained by solving the Schrödinger equation represented on a grid. The energy curves of the cationic and dicationic states were obtained by means of the algebraic diagrammatic construction scheme ADC(n) for the one- [62] and two-particle [59, 80] propagators. The ADC(3) scheme, complete up to third order in perturbation theory, was used for the calculation of monocationic states of the He·Mg cluster with the aug-cc-pVQZ basis set for He and aug-cc-pVTZ basis set augmented by one diffuse d and one diffuse f Gaussian type orbitals ($\zeta_d = 0.0148$, $\zeta_d = 0.0297$) for Mg. The energy curves of the dicationic states are more costly to compute and were calculated by the second order ADC(2) method using the aug-cc-pVQZ basis sets for both He and Mg. The restricted Hartree-Fock molecular orbitals and Coulomb integrals which serve as the input for the ADC(n) calculations were determined by the MOLCAS 7.4 quantum chemistry package [81].

3.1.2 Electronic decay widths

The ETMD rates were calculated by means of Fano-ADC-Stieltjes method, with the bound and continuum part of the corresponding resonance state constructed using the ADC(2)-extended (ADC(2x)) scheme for the one-particle propagator [20]. For this purpose we used on each atom a cc-pVQZ basis set augmented by $8s8p8d$ Kaufmann-Baumeister-Jungen (KBJ) continuumlike functions [82] on the atoms and $4s4p4d$ KBJ functions were added between the atomic centers to improve the convergence behavior of the Stieltjes procedure.

The RCT rates were computed using the multi-reference configuration interaction (MRCI) method implemented in the GAMESS-US 2011 quantum chemistry package [83]. Aug-cc-pVQZ basis sets at the atomic centers were utilized. The CI expansion comprised

Parts of this chapter have been already published in
V. Stumpf, N. V. Kryzhevoi, K. Gokhberg and L. S. Cederbaum, Phys. Rev. Lett. **112**, 193001 (2014). Copyright 2014, American Physical Society.

all single, double, and triple excitations (MRCI-SDT) out of the reference configurations. The reference space included the one-hole (1h) configurations resulting from all possible occupations of the two highest occupied orbitals ($1s$ of He and $3s$ of Mg) with three electrons.

3.2 He_m·Mg_n

3.2.1 Cluster geometries

The geometries of neutral, symmetric He·Mg_3 and He_2·Mg_n ($n = 1 - 3$) clusters were determined by means of the CCSD(T) method implemented in the MOLPRO 2010.1 [76] quantum chemistry software package using aug-cc-pVQZ [78] basis sets for both He and Mg atoms. The geometries at which ETMD shows the highest decay rate and contributes at most to the electron spectra are classical turning points along the coordinates of He^+ or He_2^+ center of mass movement relative to the Mg_n center of mass.

3.2.2 Energetics of the electronic decay

The energies of the initial states of ETMD were computed using the ADC(2x) scheme for the particle propagator [62] and aug-cc-pVTZ basis sets [78] for both He and Mg atoms. Similar basis sets and the ADC(2) scheme for the two-particle propagator [59, 80] were utilized to compute the energies of the doubly ionized final states of ETMD. The restricted Hartree-Fock molecular orbitals and Coulomb integrals which serve as the input for the ADC(n) calculations were computed by the MOLCAS 7.4 quantum chemistry package [81].

3.3 Ne·Xe

3.3.1 Energetics of the electronic decay

The Ne·Xe ground state potential energy curve (PEC) was calculated by the CCSD(T) method implemented in the GAMESS-US 2011 quantum chemistry package [83] using the aug-cc-pVQZ basis set on neon and the aug-cc-pVQZ-PP basis set on xenon atoms. The scalar relativistic effects on xenon were taken into account by a 28-electron effective core potential [78]. An additional mid-bond basis set comprising $3s3p2d2f1g$ basis functions was used to improve the description of the electronic density between the atoms [79]. The BSSE error was corrected by a counterpoise procedure.

The potential energies of the doubly ionized decaying states and the triply ionized ETMD channels were obtained by adding the corresponding non-relativistic ionization

Parts of this chapter have been already published in
A. C. LaForge, V. Stumpf, K. Gokhberg, J. von Vangerow, F. Stienkemeier et al., Rev. Lett. **116**, 203001 (2016). Copyright 2016, American Physical Society.
V. Stumpf, S. Scheit, P. Kolorenč and K. Gokhberg, Chem. Phys., http://dx.doi.org/10.1016/j.chemphys.2016.08.018 (2016). Copyright 2016, Elsevier.

energies to the ground state energy of Ne·Xe. The double and triple ionization energies were computed within the framework of the Algebraic Diagrammatic Construction (ADC) scheme based on the perturbational expansion of the two-particle and three-particle propagator, respectively, complete up to second order in perturbation theory (ADC(2)) [59, 84]. The double ionization energies were computed using the strict, the triple ionization energies using the ADC(2x) scheme. In the $Ne^+(2p^{-1}\ ^2P)\cdot Xe^{2+}(5p^{-2}\ ^3P)$ ETMD channel a strong splitting due to the relativistic effects occurs. We performed only nonrelativistic calculations since a phenomenological model derived from non-relativistic results leads to the ETMD spectra of sufficient accuracy. More important, for the computation of electronic decay widths no relativistic methods were available, prohibiting a fully relativistic calculation of the ETMD spectra.

3.3.2 Electronic decay widths

The ETMD widths were calculated by the Fano-ADC-Stieltjes method, with the bound and continuum part of the corresponding resonance state constructed using the ADC(2)-extended scheme for the two-particle propagator [21]. The 90 different $Ne^+(2p^{-1}\ ^2P)\cdot Xe^{2+}(5p^{-2})$ non-relativistic states split into three groups derived from the ^3P, ^1D and ^1S multiplets of $Xe^{2+}(5p^{-2})$. Among these states, only the spin-doublet states are accessible in the electronic decay, since the $Ne^{2+}(2p^{-2})\cdot Xe$ decaying states are spin-singlet and the coupling term is spin free. At large interatomic distances, there are 27 open $Ne^+(2p^{-1}\ ^2P)\cdot Xe^{2+}(5p^{-2})$ doublet channels, represented by 27 adapted states in the $\mathcal{P}$ subspace of the Fano-ADC-Stieltjes scheme. Reducing the interatomic distance leads to subsequent closing of the $Ne^+(2p^{-1}\ ^2P)\cdot Xe^{2+}(5p^{-2}\ ^1S)$ and $Ne^+(2p^{-1}\ ^2P)\cdot Xe^{2+}(5p^{-2}\ ^1D)$ groups of channels. We take the closing of these channels into account by reducing the number of the adapted states to 24 and 9, respectively. The partial ETMD widths describing decay into groups of channels given by the ^3P, ^1D and ^1S multiplets of $Xe^{2+}(5p^{-2})$ were determined by the projection operator approach described in chapter 2.2.4. The decaying $Ne^{2+}(2p^{-2})\cdot Xe$ states interact with other resonances in the considered range of interatomic distances. The interaction with resonances of main state character is discussed in chapter 5.1.3. Additionally, numerous satellite states appear, which cross the decaying state and modify its wavefunction at the position of the crossing. Lying in the electronic continuum, they populate the same states as the ETMD of $Ne^{2+}(2p^{-2})\cdot Xe$ but by a different mechanism such as ICD or atomic autoionization. The charge transfer driven ETMD belongs to the slowest two-electron relaxation mechanisms at intermediate and large internuclear distances. Therefore, any interaction with a resonance decaying by ICD or autoionization mechanisms leads to a clearly visible enhancement of the decay width and an irregular behavior of Γ along the nuclear coordinate.

In the present case the satellites crossing the $Ne^{2+}(2p^{-2})\cdot Xe$ states contain mostly $Ne^+(2p^{-1})\cdot Xe^{2+}(5s^{-1}5p^{-1})nl$ and $Ne\cdot Xe^{3+}(5p^{-3})nl$ configurations, where nl is a virtual orbital. The nl series converge to the tricationic states with $Ne^+(2p^{-1})\cdot Xe^{2+}(5s^{-1}5p^{-1})$ and $Ne\cdot Xe^{3+}(5p^{-3})$ character, respectively. The behavior of the electronic decay widths resulting from the interaction with the satellite states is exemplified for the $Ne^{2+}(2p^{-2})\cdot Xe$ $^1\Delta$ state in Fig. 3.1. At distances larger than 4.55 Å, where all $Ne^+(2p^{-1}\ ^2P)\cdot Xe^{2+}(5p^{-2})$ are open, the decay width is highly irregular although the weights of the coefficients

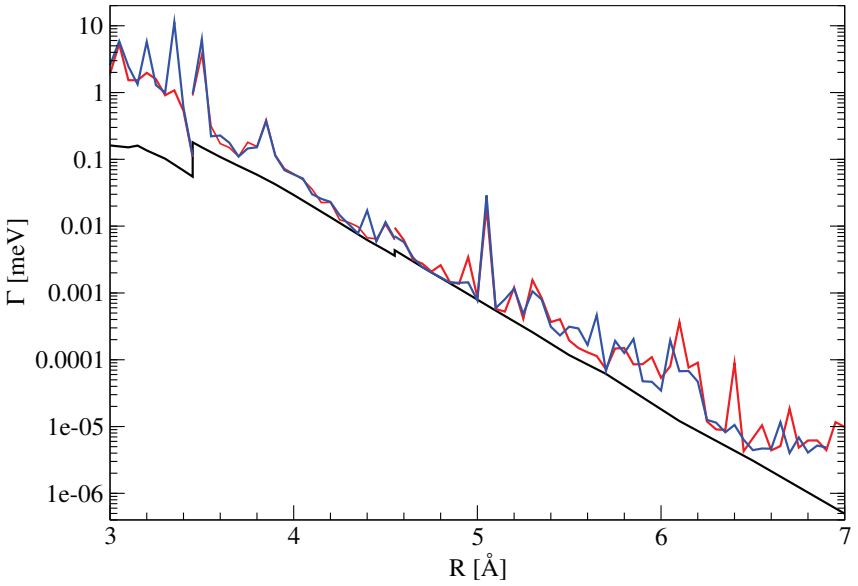

Figure 3.1: Variation of the electronic decay width of the $Ne^{2+}(2p^{-2})$·Xe $^1\Delta$ state with the composition of the $\mathcal{Q}$ subspace. (Red line) Full $\mathcal{Q}$ subspace includes adapted states of $Ne^{+}(2p^{-1})$·$Xe^{2+}(5s^{-1}5p^{-1})nl$ and Ne·$Xe^{3+}(5p^{-3})nl$ character, which cross the decaying state and cause an increase of the decay width at the position of the crossings. (Blue line) Minor modification of the electronic basis set (removal of a diffuse basis function of Xe) changes positions of certain crossings, weights of $Ne^{+}(2p^{-1})$·$Xe^{2+}(5s^{-1}5p^{-1})nl$ and Ne·$Xe^{3+}(5p^{-3})nl$ configurations and thus the decay widths. (Black line) Removal of the corresponding adapted states from the $\mathcal{Q}$ subspace leads to a regular behavior of the decay width.

belonging to the satellite configurations are low ($<10^{-4}$). The coupling of the $Ne^{+}(2p^{-1})$·$Xe^{2+}(5s^{-1}5p^{-1})nl$ and the Ne·$Xe^{3+}(5p^{-3})nl$ configurations to the $Ne^{+}(2p^{-1}\ ^2P)$·$Xe^{2+}(5p^{-2})$ final states is of ICD type and autoionization type, respectively. Thus, in spite of the low weights of these configurations the decay width is markedly increased.

To obtain a regular behavior of the ETMD width we removed adapted states with the $Ne^{+}(2p^{-1})$·$Xe^{2+}(5s^{-1}5p^{-1})nl$ and Ne·$Xe^{3+}(5p^{-3})nl$ character from the $\mathcal{Q}$ subspace. Additionally, we removed adapted states of $Ne^{+}(2p^{-1})$·$Xe^{2+}(5p^{-2})nl$ character describing the closed ETMD channels in the corresponding intervals of nuclear distances. One has to keep in mind that the energies of the satellites crossing the decaying state are treated at first perturbational order in the ADC(2x) scheme, hence the positions of the crossings with the $Ne^{2+}(2p^{-2})$·Xe states and the weights of the satellite configurations are highly inaccurate. Moreover, these properties are mostly sensitive to the electronic basis sets. The modification of the $\mathcal{Q}$ subspace provides decay widths which converge with respect to the electronic basis and constitute a lower bound to the uncorrected decay widths. We utilized the regularized ETMD width in further discussions and in nuclear dynamics simulations.

For the decay width calculations we utilized the cc-pVQZ basis set on neon [78]

and non-relativistic cc-pVQZ [85] basis set on xenon. To improve the description of the discretized ADC continuum we added $5s5p5d3f$ continuum like Kaufmann-BaumeisterJungen (KBJ) [82] basis functions on neon, $7s7p7d4f1g$ basis functions on xenon and $2s2p2d$ mid-bond basis functions.

3.3.3 Nuclear dynamics

The nuclear dynamics accompanying the electronic decay process is described by using a theoretical framework based on the propagation of nuclear wave packets, described in detail in Ref. [86] to which the reader is referred. The nuclear wave packets propagating along the initial, decaying and final states PES are obtained by solving a system of coupled time dependent Schrödinger equations. The Hamilton operator associated to each of the electronic states is given by the sum of the nuclear kinetic energy operator $\hat{T}_N$ and the associated potential energy operators $\hat{V}_i$, $\hat{V}_{d_j}$ and $\hat{V}_{f_k}$ obtained as described in 3.3.1, where i stays for initial, d for decaying and f for final state and the indices j and k number the decaying and final states, respectively. Additionally, for the decaying states the complex term $i\frac{\Gamma^{d_j}}{2}$ has to be added, with Γ^{d_j} being the corresponding total decay width operator computed as in 3.3.2: this renders the Hamilton operator for the ETMD states non-hermitian. The partial decay width operator $\Gamma^{d_j}_{f_k}$ associated to the transition from a given decaying state to a specific final state f_k, is responsible instead for the coupling between the equations for the corresponding decaying and final wave packets.

In principle, also the equations for the initial and the decaying wave packets are coupled through the excitation operator, which typically contains the transition dipole moment between the states. For the present study, however, the ionization process is assumed to be instantaneous, and the excitation operator independent on the nuclear coordinate. Furthermore, due to the much shorter Auger lifetime of the $Ne^+(1s^{-1})$·Xe state in comparison to the ETMD lifetime of the $Ne^{2+}(2p^{-2})$·Xe states, the nuclear dynamics is neglected also in the Auger decay step, so that the nuclear wave packet propagation is started by a vertical transition of the initial wave packet to the PES of the states decaying via ETMD, as done in similar dynamical studies of Auger-ICD cascades (see e.g. Refs. [87, 88]). Therefore the initial condition is $\Psi_{d_j}(t_0) = \Psi_i(t_0)$, where Ψ_{d_j} is the wave packet propagating along the PES of the j-th decaying state and Ψ_i is the wave packet associated to the initial electronic state. The initial wave packet at time t_0, $\Psi_i(t_0)$, is taken to coincide with the lowest vibrational eigenstate of the electronic ground state of Ne·Xe: it is therefore gaussian-like and centered at about 3.9 Å, the equilibrium distance of the ground state PES. The numerical grid used starts at 2 Å, ends at 11 Å and contains 1806 points, the wave packets are propagated for about 200 ps before convergence for all decay channels is obtained.

All the spectroscopic information required for the computation of the ETMD electron spectrum is contained in the wave packets for the final electronic states. In the absence of non-adiabatic couplings between the decaying and final states, the total electron spectrum is obtained as the sum of the partial spectra associated to the decay from each

intermediate to each accessible final state,

$$\sigma^{fin}(E_{ETMD}) = \lim_{t\to\infty} \sigma(E_{ETMD}, t) = \lim_{t\to\infty} \sum_j \sum_k \langle \Psi_{f_k}^{d_j}(E_{ETMD}, t) | \Psi_{f_k}^{d_j}(E_{ETMD}, t) \rangle, \quad (3.1)$$

where E_{ETMD} is the energy of the emitted ETMD electron and $\Psi_{f_k}^{d_j}(E_{ETMD})$ is the final wave packet propagating along the k-th final state and resulting from the decay of the j-th decaying state. Therefore, by the knowledge of the nuclear wave packets at each time, it is possible to follow the time evolution of the spectrum, given by $\sigma(E_{ETMD}, t)$.

The kinetic energy release spectrum for the fragments emitted after the decay is obtained from the electron decay spectrum by making use of the reflection principle [34], which is based on the principle of energy conservation and, therefore, exploits the relation $E_{TOT} = E_{ETMD} + E_{KER} + V_f^\infty$, where V_f^∞ is the asymptotic value of the final state PES. Note, however, that additional information about the different decay channels can be extracted from the KER, which is instead hidden in the electron spectrum.

3.4 Ne·Kr$_2$

3.4.1 Cluster geometry

The equilibrium geometry of the neutral Ne·Kr$_2$ cluster was determined by means of the CCSD(T) method as implemented in the MOLPRO 2010.1 quantum chemistry package [76]. For both Ne and Kr aug-cc-pVQZ correlation consistent basis sets [78] located on the corresponding atoms were used. Three sets of additional $3s3p2d2f1g$ mid-bond basis functions were used to improve the description of the electronic density between the pairs of atoms [79]. The optimized geometry of Ne·Kr$_2$ has a C_{2v} symmetry with Ne·Kr interatomic distance $r = 3.68$ Å and KrNeKr angle $\theta = 67.01$ °.

3.4.2 Energetics of the electronic decay

The energies of the Ne$^{2+}(2p^{-2}\ ^1\mathrm{D})$·Kr$_2$ electronic states decaying by ETMD were determined using the ADC(2) scheme for the two-particle propagator [59]. The aug-cc-pVQZ basis sets located on the Ne and Kr atoms were used in this calculation. The restricted Hartree-Fock orbitals and integrals needed as input data for ADC(2) were generated by SCF routine implemented in MOLCAS 7.4 quantum chemistry package [81]. The energies of the final states Ne$^+(2p^{-1}\ ^2\mathrm{P})$·$(\mathrm{Kr}^+(4p^{-1}\ ^2\mathrm{P}))_2$ of ETMD(3) were calculated by adding to the ground state potential energy of Ne·Kr$_2$ the triple ionization potential approximated analytically as $IP(Ne) + 2IP(Kr) + 2/R_{NeKr} + 1/R_{KrKr}$. The abbreviation IP(X) stands for the ionization potential of atom X and R_{XY} is the distance between atoms X and Y.

Parts of this chapter have been already published in
V. Stumpf, P. Kolorenč, K. Gokhberg and L. S. Cederbaum, Phys. Rev. Lett. **110**, 258302 (2013).

3.4.3 Electronic decay widths

The ETMD widths were obtained employing the Fano-ADC-Stieltjes approach [21]. Adapted states representing the closed $Ne^+(2p^{-1}\ ^2P)\cdot(Kr)Kr^{2+}(4p^{-2})$ ETMD(2) channels were removed from the $\mathcal{Q}$ subspace to ensure a regular behavior of the ETMD(3) width (see chapter 3.3.2 for the description of this procedure). We used cc-pVTZ basis set augmented by $4s4p4d$ for Ne, and cc-pVTZ basis set augmented by $5s5p5d$ KBJ [82] continuum-like basis functions for Kr to improve the description of the ADC discretized continuum.

3.4.4 Nuclear dynamics

For the $Ne^{2+}(2p^{-2}\ ^1D)\cdot Kr_2$ decaying state classical nuclear dynamics calculations were performed. We assumed that the $Ne^{2+}(2p^{-2}\ ^1D)\cdot Kr_2$ cluster is in the rotational ground state, hence the rotational degrees of freedom were neglected. We solved the classical Hamilton equation of the nuclear motion, employing internal Jacobi coordinates: q_1 is given by the distance between the Kr atoms, q_2 by the distance between Ne and the Kr_2 center of mass while ϕ is given ..by the angle between q_1 and q_2. We only considered the coordinates q_1, q_2, therefore preserving the C_{2v} symmetry of the cluster; the angle ϕ was kept constant ($\phi = 90°$). In these coordinates the representation of the nuclear Hamiltonian H has a simple structure [89]:

$$H = \frac{1}{2\mu_1}P_1^2 + \frac{1}{2\mu_2}P_2^2 + V(q_1, q_2), \tag{3.2}$$

where P_i denote the conjugate momenta and $V(q_1, q_2)$ is the PES of the $Ne^{2+}(2p^{-2}\ ^1D)\cdot Kr_2$ state of b_1 symmetry. The reduced masses are defined as:

$$\mu_1 = \frac{m_{Kr}}{2}, \quad \mu_2 = \frac{2m_{Kr}m_{Ne}}{2m_{Kr} + m_{Ne}}. \tag{3.3}$$

The equilibrium geometry of the $Ne\cdot Kr_2$ cluster defined the initial values of q_1 and q_2, while the initial momenta were set to zero. The numerical solution of the Hamilton equation provided a trajectory for the nuclear motion on the two-dimensional, real PES. We calculated the ETMD rate $\Gamma(R)$ along this trajectory, which allowed us to reformulate this rate as a time dependent quantity $\Gamma(t)$ which enters the following differential equation for the population $N(t)$ of the decaying state:

$$\frac{dN(t)}{dt} = -\Gamma(t)N(t). \tag{3.4}$$

The solution of this equation with the initial condition $N(t = 0) = 1$ yields the cumulative ETMD yield $P(t)$:

$$P(t) = 1 - N(t) = 1 - e^{-\int_0^t \Gamma(t')dt'}. \tag{3.5}$$

3.5 $Mg^{2+}\cdot(H_2O)_6$

3.5.1 Cluster geometry

The geometry of the $Mg^{2+}\cdot(H_2O)_6$ cluster was obtained by symmetry constrained optimization, relying on the Møller-Plesset second order perturbation theory (MP2) implemented in the MOLPRO 2010.1 quantum chemistry package [76]. The T_h symmetry of the cluster was chosen according to Glendening et al. and represents the global minimum geometry [90]. All electronic decay processes were studied at this cluster geometry.

3.5.2 Energetics of the electronic decay

Core ionization of the $Mg^{2+}\cdot(H_2O)_6$ cluster creates a highly energetic magnesium trication which decays by the Auger mechanism and accumulates positive charge. A series of interatomic electronic decay steps leads to the reduction of magnesium to the original Mg^{2+} state. We found that the cascade comprises the following steps:

$$\begin{aligned} &Mg^{3+}(1s^{-1})\cdot(H_2O)_6 \xrightarrow{Auger} Mg^{4+}([2p^{-2}]/[2s^{-1}2p^{-1}]/[2s^{-2}])\cdot(H_2O)_6 + e_{Auger} \\ &Mg^{3+}(1s^{-1})\cdot(H_2O)_6 \xrightarrow{Core\ ICD-like} Mg^{3+}(2p^{-1})\cdot(H_2O^{+})(H_2O)_5 \end{aligned} \tag{3.6}$$

$$\begin{aligned} &Mg^{4+}([2s^{-1}2p^{-1}]/[2s^{-2}])\cdot(H_2O)_6 \xrightarrow{ICD} Mg^{4+}([2p^{-2}]/[2s^{-1}2p^{-1}])\cdot(H_2O^{+})(H_2O)_5 \\ &Mg^{4+}([2p^{-2}]/[2s^{-1}2p^{-1}])\cdot(H_2O)_6 \xrightarrow{ETMD(2)} Mg^{3+}([2p^{-1}]/[2s^{-1}])\cdot(H_2O^{2+})(H_2O)_5 \\ &Mg^{4+}([2p^{-2}]/[2s^{-1}2p^{-1}])\cdot(H_2O)_6 \xrightarrow{ETMD(3)} Mg^{3+}([2p^{-1}]/[2s^{-1}])\cdot(H_2O^{+})_2(H_2O)_4 \end{aligned} \tag{3.7}$$

$$\begin{aligned} &Mg^{3+}(2s^{-1})\cdot(H_2O)_6 \xrightarrow{ICD} Mg^{3+}(2p^{-1})\cdot(H_2O^{+})(H_2O)_5 \\ &Mg^{3+}(2p^{-1})\cdot(H_2O)_6 \xrightarrow{ETMD(2)} Mg^{2+} - (H_2O^{2+})(H_2O)_5 \\ &Mg^{3+}(2p^{-1})\cdot(H_2O)_6 \xrightarrow{ETMD(3)} Mg^{2+} - (H_2O^{+})_2(H_2O)_4, \end{aligned} \tag{3.8}$$

where for better readability we provided Mg^{q+} ions with the full complement of six neutral water ligands. In complexes obtained during the cascade some of the water ligands will be ionized in the previous steps. The number and charge of these ligands will depend on a particular de-excitation route followed by the system.

To determine the electronic states of Mg involved in the decay cascade we computed their energies. All electronic structure calculations were carried out at the equilibrium geometry of the $Mg^{2+}\cdot(H_2O)_6$ cluster using the electronic configuration in the ground electronic state of $Mg^{2+}\cdot(H_2O)_6$ as the reference. The initial $Mg^{2+}\cdot(H_2O)_6$ state energy was determined by the Møller-Plesset second order perturbation theory (MP2).

Parts of this chapter have been already published in
V. Stumpf, K. Gokhberg and L. S. Cederbaum, Nat. Chem. **8**, 237 (2016).

The electronic states of interest include tricationic, tetracationic and pentacationic states. The energies of the tricationic states were obtained by the ADC(2x) method [62]. The energies of the tetracationic states were calculated by the ADC(2) method for the two-particle propagator [59,80]. The electron integrals and molecular orbitals serving as input for the propagator based computations were calculated by MOLCAS 7.4 software package [81].

The ETMD and ICD of high lying tetracationic states lead to pentacationic states (Eq. (3.6)), for which no propagator approach was available. Therefore, a multi-reference configuration interaction (MRCI) method including single and double excitations (DIRECT-CI) [91] implemented in the GAMESS-UK 8.0 quantum chemistry package [92] was used. The final states of ETMD were constructed by selecting all configurations having a hole in a $2s$ or $2p$ orbital of Mg^{2+} plus two additional holes in the valence orbitals localized on water molecules. The final states of ICD were constructed by selecting all configurations having two holes in $2s$, $2p$ orbitals of Mg^{2+} plus an additional hole in the valence orbitals localized on water molecules. This method is computationally demanding and not size extensive which limited the size of the model system to the metal cation and two water neighbors. We estimated the effect of leaving out four water molecules and found that the same ICD and ETMD channels are open in $Mg^{4+}\cdot(H_2O)_2$ and $Mg^{4+}\cdot(H_2O)_6$. Addition of point charges simulating the ionized water molecules in the first solvation shell lead to closing of some of ETMD(2) channels.

3.5.3 Electronic decay widths

We computed the energy widths of the decaying states in Eqs. (3.6-3.8) to determine the timescales on which different electronic decay processes occur. To this end we used the *ab initio* Fano-ADC-Stieltjes method [20, 21]. The bound and continuum parts of the decaying tricationic and tetracationic states were constructed by means of the ADC(2)-extended scheme for the one-particle and two-particle propagator, respectively [59, 62]. The renormalization of the pseudocontinuum generated by the ADC scheme in an $\mathcal{L}^2$ basis is done by the Stieltjes imaging technique [74]. The partial decay widths were estimated by projecting the pseudocontinuum part of the resonance wave function onto the configurations belonging to a channel of interest (e.g. the ETMD(2) channel, see chapter 2.2.4).

The ICD and ETMD widths of the Mg^{3+} ion could be computed for the full solvation shell of six water molecules. In the case of the Mg^{4+} ion we had to resort to an approximation, since it was not feasible to construct an accurate pseudocontinuum part of the resonances in the $Mg^{4+}\cdot(H_2O)_6$ cluster. However, as was demonstrated in previous studies on ETMD and ICD, a good approximation to the electronic decay widths in a large system can be obtained by adding up the decay widths calculated for subunits of a system [93, 94]. Thus the total ICD width in a cluster with N water neighbors

$$\Gamma^{ICD} = \sum_{i=1}^{N} \Gamma_i^{ICD}, \tag{3.9}$$

where Γ_i^{ICD} is the ICD width due to the i-th water neighbor. The total ETMD(2) width

is obtained in a similar way

$$\Gamma^{(2)} = \sum_{i=1}^{N} \Gamma_i^{(2)}, \tag{3.10}$$

while for the determination of the total ETMD(3) width the system is divided into subunits containing the metal ion and distinct pairs of neighbors

$$\Gamma^{(3)} = \sum_{i<j} \Gamma_{ij}^{(3)}. \tag{3.11}$$

We verified the accuracy of this approximation by comparing the results of the full calculation of $Mg^{3+}(2p^{-1}\ ^2P)\cdot(H_2O)_6$ widths with the ones obtained by the additive approach. The ETMD lifetime obtained by the additive approach (15.6 fs) lies close to the value obtained by the full calculation (17.3 fs). The branching ratio of ETMD(3) to ETMD(2) product populations is 1.50 and 1.23, respectively. We conclude that the approximate method is able to reproduce the total decay width and the branching ratio fairly well.

The additive approach was also applied to calculate the width of the initially core ionized $Mg^{3+}(1s^{-1}\ ^2S)\cdot(H_2O)_6$ state itself. It decays not only locally by the Auger process but also interatomically in the core ICD-like process [95, 96] whereby the relaxation of the core vacancy results in the ionization of the neighboring water molecule. The rate of the core ICD-like processes was calculated for a subsystem with one water neighbor and extrapolated to $n = 6$. The Auger rate in the $Mg^{2+}\cdot(H_2O)_6$ cluster is only weakly modified compared to the atomic value computed by the Fano-ADC-Stieltjes method.

3.5.4 Cascade of electronic decay processes

The separate electronic decay processes discussed above constitute a decay cascade initiated by removing a $1s$ electron of Mg. One of the important characteristics of this cascade is its overall duration which can be found if the decay rates of each individual step of the cascade is known. The calculation of these rates is complicated by the fact that interatomic processes occurring earlier in the cascade ionized the nearest neighbors. Therefore, subsequent interatomic decay happens in the presence of water cations and is accompanied by the Coulomb explosion of the cluster. The accumulation of the positive charge in the vicinity of the metal has an impact on the electron energies and decay rates. In general, the latter are expected to decrease due to the fact that fewer ionizable water neighbors are available and the number of open decay channels per neighbor is less than in the $Mg^{q+}(H_2O)_6$ case.

We took this effect into account by replacing the ionized neighbors by point charges in determining the open decay channels and the corresponding decay rates at each individual step (see Tab. 3.1). The point charge model contains the leading term in the multipole expansion of the charge distribution on the ionized water molecules; therefore, the main part of the electrostatic interaction with the ionized water neighbors is taken into account. Such calculations show that the whole cascade is energetically possible even without removing ionized water molecules from the first solvation shell. To obtain the overall duration of the decay cascade and the time dependent populations of the species involved we solved the corresponding system of rate equations. The decreasing

Table 3.1: Rates utilized in the kinetic model of the electronic decay cascade initiated by the core ionization of Mg in the $Mg^{2+}\cdot(H_2O)_6$ cluster. The individual decay steps can be found in the cascade scheme, Fig. 6.2. Repulsive nuclear dynamics occurring after the interatomic electronic decay steps are not taken into account, all decay rates were determined at the equilibrium geometry of the $Mg^{2+}\cdot(H_2O)_6$ cluster. Water neighbors ionized in a decay step are not available for further interatomic electronic decay. The presence of water cations from previous steps of the cascade may lead to the closing of open decay channels, which was taken into account by using a point charge approximation of these cations. The numbers in parentheses represent the decay rates for a given number of water neighbors with the water cations/point charges removed.

Decay mode	Decay step	k [fs^{-1}]
Auger	$Mg^{3+}(1s^{-1}\ ^2P)\cdot(H_2O)_6 \rightarrow Mg^{4+}(2p^{-2}\ ^1D,\ ^1S)\cdot(H_2O)_6$	0.3211
	$Mg^{3+}(1s^{-1}\ ^2P)\cdot(H_2O)_6 \rightarrow Mg^{4+}(2s^{-1}2p^{-1}\ ^3P)\cdot(H_2O)_6$	0.0442
	$Mg^{3+}(1s^{-1}\ ^2P)\cdot(H_2O)_6 \rightarrow Mg^{4+}(2s^{-1}2p^{-1}\ ^1P)\cdot(H_2O)_6$	0.1068
	$Mg^{3+}(1s^{-1}\ ^2P)\cdot(H_2O)_6 \rightarrow Mg^{4+}(2s^{-2}\ ^1S)\cdot(H_2O)_6$	0.0374
Core ICD-like	$Mg^{3+}(1s^{-1}\ ^2P)\cdot(H_2O)_6 \rightarrow Mg^{4+}(2s^{-2}\ ^1S)\cdot(H_2O^+)(H_2O)_5$	0.0168
ICD	$Mg^{4+}(2s^{-1}2p^{-1}\ ^1P)\cdot(H_2O)_6 \rightarrow Mg^{4+}(2p^{-2}\ ^1D,\ ^1S)\cdot(H_2O^+)(H_2O)_5$	1.2987
	$Mg^{4+}(2s^{-2}\ ^1S)\cdot(H_2O)_6 \rightarrow Mg^{4+}(2s^{-1}2p^{-1}\ ^3P)\cdot(H_2O^+)(H_2O)_5$	1.1111
	$Mg^{3+}(2s^{-1}\ ^2S)\cdot(H_2O)_5 \rightarrow Mg^{3+}(2p^{-1}\ ^2P)\cdot(H_2O^+)(H_2O)_4$	0.1190 (1.0417)
	$Mg^{3+}(2s^{-1}\ ^2S)\cdot(H_2O)_4 \rightarrow Mg^{3+}(2p^{-1}\ ^2P)\cdot(H_2O^+)(H_2O)_3$	0.0952 (0.8333)
	$Mg^{3+}(2s^{-1}\ ^2S)\cdot(H_2O)_3 \rightarrow Mg^{3+}(2p^{-1}\ ^2P)\cdot(H_2O^+)(H_2O)_2$	0.0066 (0.6250)
ETMD(2)	$Mg^{4+}(2p^{-2}\ ^1D,\ ^1S)\cdot(H_2O)_6 \rightarrow Mg^{3+}(2p^{-1}\ ^2P)\cdot(H_2O^{2+})(H_2O)_5$	0.0240
	$Mg^{4+}(2p^{-2}\ ^1D,\ ^1S)\cdot(H_2O)_5 \rightarrow Mg^{3+}(2p^{-1}\ ^2P)\cdot(H_2O^{2+})(H_2O)_4$	0.0200
	$Mg^{4+}(2s^{-1}2p^{-1}\ ^3P)\cdot(H_2O)_6 \rightarrow Mg^{3+}(2p^{-1}\ ^2P)\cdot(H_2O^{2+})(H_2O)_5$	0.0119
	$Mg^{4+}(2s^{-1}2p^{-1}\ ^3P)\cdot(H_2O)_6 \rightarrow Mg^{3+}(2s^{-1}\ ^2S)\cdot(H_2O^{2+})(H_2O)_5$	0.0158
	$Mg^{4+}(2s^{-1}2p^{-1}\ ^3P)\cdot(H_2O)_5 \rightarrow Mg^{3+}(2p^{-1}\ ^2P)\cdot(H_2O^{2+})(H_2O)_4$	0.0100
	$Mg^{4+}(2s^{-1}2p^{-1}\ ^3P)\cdot(H_2O)_5 \rightarrow Mg^{3+}(2s^{-1}\ ^2S)\cdot(H_2O^{2+})(H_2O)_4$	0.0134
ETMD(3)	$Mg^{4+}(2p^{-2}\ ^1D,\ ^1S)\cdot(H_2O)_6 \rightarrow Mg^{3+}(2p^{-1}\ ^2P)\cdot(H_2O^+)_2(H_2O)_4$	0.0388
	$Mg^{4+}(2p^{-2}\ ^1D,\ ^1S)\cdot(H_2O)_5 \rightarrow Mg^{3+}(2p^{-1}\ ^2P)\cdot(H_2O^+)_2(H_2O)_2$	0.0258
	$Mg^{4+}(2s^{-1}2p^{-1}\ ^3P)\cdot(H_2O)_6 \rightarrow Mg^{3+}(2p^{-1}\ ^2P)\cdot(H_2O^+)_2(H_2O)_4$	0.0106
	$Mg^{4+}(2s^{-1}2p^{-1}\ ^3P)\cdot(H_2O)_6 \rightarrow Mg^{3+}(2s^{-1}\ ^2S)\cdot(H_2O^+)_2(H_2O)_4$	0.0191
	$Mg^{4+}(2s^{-1}2p^{-1}\ ^3P)\cdot(H_2O)_5 \rightarrow Mg^{3+}(2p^{-1}\ ^2P)\cdot(H_2O^+)_2(H_2O)_3$	0.0071
	$Mg^{4+}(2s^{-1}2p^{-1}\ ^3P)\cdot(H_2O)_5 \rightarrow Mg^{3+}(2s^{-1}\ ^2S)\cdot(H_2O^+)_2(H_2O)_3$	0.0126
	$Mg^{3+}(2p^{-1}\ ^2P)\cdot(H_2O)_5 \rightarrow Mg^{2+}(^1S)\cdot(H_2O^+)_2(H_2O)_3$	0.0230 (0.0438)
	$Mg^{3+}(2p^{-1}\ ^2P)\cdot(H_2O)_4 \rightarrow Mg^{2+}(^1S)\cdot(H_2O^+)_2(H_2O)_2$	0.0140 (0.0299)
	$Mg^{3+}(2p^{-1}\ ^2P)\cdot(H_2O)_3 \rightarrow Mg^{2+}(^1S)\cdot(H_2O^+)_2(H_2O)$	0.0070 (0.0188)
	$Mg^{3+}(2p^{-1}\ ^2P)\cdot(H_2O)_2 \rightarrow Mg^{2+}(^1S)\cdot(H_2O^+)_2$	0.0025 (0.0125)

number of ionizable neighbors in the course of the cascade was taken into account by calculating decay rates as described in Eqs. 3.9-3.11.

3.5.5 Basis sets for electronic structure calculations

The cc-pCVTZ basis set on magnesium and daug-cc-pVTZ basis set on oxygen and hydrogen atoms were utilized for geometry optimizations and calculations of energies of the decaying states [78,97]. The calculation of the core ionization potential of $Mg^{2+}\cdot(H_2O)_6$ required an uncontraction of the atomic basis set on magnesium. In the final states of the electronic decay additional positive charge on the neighboring water molecules is created, therefore cc-pCVTZ basis set for oxygen and cc-pVTZ for hydrogen atoms were used [98,99].

Decay width calculations required an augmentation of the standard atomic basis sets by Kaufmann-Baumeister-Jungen (KBJ) continuum-like functions to improve the description of the pseudocontinuum [82]. In particular, cc-pCVTZ (magnesium and oxygen) and cc-pVTZ atomic basis set (hydrogen) were augmented by $1s1p1d1f$ KBJ basis functions on magnesium, $4s4p4d1f$ on oxygen and $2s2p2d$ on hydrogen. Additionally, $2s2p2d$ KBJ basis functions were located between the magnesium and oxygen atoms. The atomic cc-pCV5Z (magnesium, oxygen) and cc-pV5Z (hydrogen) basis sets were uncontracted for the computation of the Auger rate in order to better describe the fast outgoing Auger electron [78,98].

3.6 $M^{q+}\cdot(H_2O)_n$

3.6.1 Cluster geometries

We investigated the behavior of the ICD widths in microsolvated clusters as the function of two parameters: the number of water neighbors, and the M^{q+}-O distance. To find the width's variation with the number of neighbors we constructed $Na^+\cdot(H_2O)_m$ (m = 1-4), $Mg^{2+}\cdot(H_2O)_n$ (n = 1-6) clusters starting from the equilibrium structures of the parent $Na^+\cdot(H_2O)_4$, $Mg^{2+}\cdot(H_2O)_6$ clusters. The latter represent stable clusters with the highest possible number of water molecules in the first coordination shell in the gas phase. However, they also play an important role in the description of the metal ions' solvation shell in solution as we will discuss below. The symmetries of the parent clusters were chosen following the structural studies of Glendening et al. [90] as S_4 and T_h respectively. For the geometry optimization of the parent clusters we used Møller-Plesset second order perturbation theory (MP2) implemented in the MOLPRO 2010.1 package [76] which provides accurate results for the systems with ion-permanent dipole interactions [100]. To obtain the clusters with $m < 4$ and $n < 6$ we removed the water ligands one by one from the parent clusters leaving the structure of the rest of the cluster intact. There is no unique way to do that and we selected the procedure, whereby the number of *cis*-pairs is maximized. The derived $Na^+\cdot(H_2O)_m$ clusters belong to C_{2v}, C_1

Parts of this chapter have been already published in
V. Stumpf, C. Brunken and K. Gokhberg, J. Chem. Phys. **145**, 104306 (2016). Copyright 2016, American Institute of Physics.

and C_1 symmetry groups for m equaling 1, 2, or 3, respectively, while the $Mg^{2+}\cdot(H_2O)_n$ clusters belong to C_{2v}, C_s, C_3, C_s, C_{2v} for n ranging from 1 to 5.

The parent $Mg^{2+}\cdot(H_2O)_6$ cluster bears close resemblance to the structure of the magnesium ion and its first solvation shell in dilute solutions. The coordination number 6 is the most probable in solution due to the strong attractive interaction between Mg^{2+} and the water neighbors. The Mg^{2+}-O distance of 2.08 Å obtained in the geometry optimization lies within the range obtained in experimental studies of the aqueous solutions (2.00-2.15 Å) [101]. In contrast, the interaction between the sodium cation and the water molecules is considerably weaker resulting in a broad distribution of coordination numbers (mainly between 4 and 6 [101, 102]) and average sodium-oxygen distances in aqueous solutions (2.33-2.50 Å with the width at half-maximum being ca. 0.5 Å). However, both the coordination number and the optimal Na^+-O distance of 2.30 Å used for the $Na^+\cdot(H_2O)_4$ cluster in this work are probable in dilute solutions.

To investigate the variation of ICD widths with the cation-oxygen distance we considered $Na^+\cdot H_2O$ and $Mg^{2+}\cdot H_2O$ mono-coordinated clusters. Their reference equilibrium geometries which belong to the C_{2v} point group were obtained from the parent six- and four-coordinated structures structures by removing all but one water ligand. In the width calculations the cation-oxygen distance, R, was varied, while the rest of the coordinates were kept constant. We also considered ICD in the $Ne\cdot H_2O$ cluster extending the isoelectronic $M^{q+}\cdot H_2O$ series towards $q = 0$. To facilitate the comparison with the metal - water clusters we constrained the $Ne\cdot H_2O$ geometry to the C_{2v} symmetry and optimized the $Ne\cdot H_2O$ geometry by using the CCSD(T) method implemented in the MOLPRO 2010.1 package [76]. High-level CCSD(T) method was necessary for the $Ne\cdot H_2O$ cluster which is bound by the weak dipole-induced dipole interaction. Afterwards the Ne-oxygen distance was varied, while the rest of the coordinates were kept at their equilibrium values.

The cluster models described above deserve a short discussion. First, the smaller clusters constructed from the parent $Na^+\cdot(H_2O)_4$ and $Mg^{2+}\cdot(H_2O)_6$ ones do not represent the equilibrium geometries for a given coordination number. Since we intended to study the dependence of ICD widths on the coordination number, it was natural that the second important parameter, the metal-oxygen distance, should have been kept constant. Moreover, the dependence of the width on the symmetry of the particular arrangement of the ligands around the ion is weak, as long as the coordination number and R are kept constant. In addition, the internal geometry of water barely changes upon addition of the ion (e.g. in the case of $Mg^{2+}\cdot H_2O$ $\Delta R_{OH} = 0.007$ Å and $\Delta\theta_{HOH} = 1.5°$). Also, the equilibrium geometry of the $Ne\cdot H_2O$ cluster belongs to the C_s point group [103]. However, the C_{2v} symmetry allows a direct comparison of the ICD widths as a function of R with the widths in $Na^+\cdot H_2O$ and $Mg^{2+}\cdot H_2O$ clusters.

3.6.2 Energetics of the electronic decay

We determined the open ICD channels and the kinetic energies of the emitted ICD electrons by computing the single and double ionization energies of the cluster in question. The computations were done within the framework of the Algebraic Diagrammatic Construction (ADC(n)) scheme based on the perturbational expansion of the one-particle and two-particle propagators, respectively, complete up to second order [59, 61, 62, 80].

For the one-particle propagator expansion the extended second-order scheme, for the two-particle propagator the strict second-order scheme were used. The $Na^+\cdot(H_2O)_m$, $Mg^{2+}\cdot(H_2O)_n$ and $Ne\cdot H_2O$ reference electronic states, molecular orbitals and electron integrals required by the ADC calculations were computed by the RHF method implemented in the MOLCAS 7.4 package [81].

3.6.3 Electronic decay widths

The electronic decay widths were calculated by means of the Fano-ADC-Stieltjes method [20]. We constructed the matrix representation of H_{el} and both wave functions components using the ADC(2x) scheme for the one-particle propagator [62]. The continuum component corresponding to the $M^{(q+1)+}\cdot H_2O^+$ ICD final states and a free electron is obtained by diagonalizing the ADC matrix projected on the $2h1p$ subspace ($\mathcal{P}$) which describes open decay channels. The $\mathcal{P}$ subspace comprises $(2p_M^{-1}ov_{H_2O}^{-1})b^1$ and $(ov_{H_2O}^{-2})b^1$ configurations, where b refers to a virtual orbital. ADC matrix projected onto the initial subspace ($\mathcal{Q} = 1 - \mathcal{P}$) which includes the remaining $2h1p$ and all $1h$ configurations provides both the bound one-hole states of the system and the bound part of the resonance function in question. The latter is characterized by a large contribution of the $2s$-hole on the metal atom and can be easily identified among the eigenvectors.

In addition to the ICD final states of $M^{(q+1)+}\cdot H_2O^+$ character the ETMD into the states of $M^{q+}\cdot H_2O^{2+}$ character is also energetically allowed. The branching ratio of the ICD and ETMD processes was estimated using a projection operator approach described in Ref. [104] and chapter 2.2.4. The ICD widths were shown to dominate the ETMD ones even in the largest clusters by approximately two orders of magnitude for the considered range of metal-oxygen distances. Therefore, the total decay width in all calculations was considered to a high degree of accuracy equal to the ICD width and the calculation of the partial decay widths was not carried out. In the calculations of the sodium-water clusters the $(iv_{H_2O}^{-1}ov_{H_2O}^{-1})b^1$ and $(iv_{H_2O}^{-2})b^1$ configurations corresponding to the decay into the ETMD channels were omitted altogether. In the calculations of the magnesium-water clusters they were added to the $\mathcal{P}$ subspace.

Interatomic relaxation following the sudden creation of a $2s$-hole on the metal cations has a large impact on the ICD widths. This relaxation can be described by the interaction between $(2s_M^{-1})$ and $(2s_M^{-1}ov_{H_2O}^{-1})b^1$ configurations. The physical effect expressed by the interatomic relaxation falls between two limiting cases: dipole polarization of the water molecule (if the virtual orbital b is localized on the water molecule), or the transfer of an electron from water to the metal (if b is localized on the metal). Excluding the $(2s_M^{-1}ov_{H_2O}^{-1})b^1$ configurations from the initial subspace $\mathcal{Q}$ eliminates the effect of the polarization in a decay width calculation; it also eliminates the excited states of the charge-transfer character, e.g. $(2s_{Mg}^{-1}ov_{H_2O}^{-1})3s_{Mg}^1$ from the computed spectrum. Such states are also electronically unstable and their interaction with the ICD state may lead to irregular $\Gamma(R)$ behavior. Therefore, to study the effect of the interatomic relaxation in the ICD state as well as its interaction with other resonances present in the system we carried out calculations both with and without the corresponding configurations.

The construction of the $2s$-ionized state by the propagator based ADC method relies on the closed shell single determinant representation of the $M^{q+}\cdot(H_2O)_n$ reference state. This condition is fulfilled in $Na^+\cdot(H_2O)_n$ for all sodium-oxygen distances and any

number of neighbors. In the case of the $Mg^{2+}{\cdot}H_2O$ cluster the potential energy curve of the $Mg^{2+}{\cdot}H_2O$ state crosses the curve of the $Mg^{+}(3s^1){\cdot}H_2O^{+}$ state at $R \approx 6$ Å [105] potentially invalidating the use of the one-particle ADC schemes around this geometry. However, a single determinant RHF solution can still be obtained for the geometries in question by defining the corresponding closed shell occupation pattern. To check that the one-particle ADC(2x) calculation based on this determinant still leads to the correct description of the $(2s^{-1}_{Mg})$ state we computed the same state by the three-particle ADC(2x) propagator [84] starting from the $Mg{\cdot}H_2O$ closed shell reference. It could be demonstrated that both methods provide a closely matching results for the energy of this state and the character of its wave function for $R \approx 6.0$ Å . Therefore, we expect the widths obtained by the one-particle ADC(2x) method to be accurate even at the geometries where the ground state of the clusters is of multi-reference character.

In the analysis of the performance of the Fano-ADC-Stieltjes method in the asymptotic regime a computation of transition energies and transition dipole moments for the $M^{q+1}(2s^{-1}) \rightarrow M^{q+1}(2p^{-1})$ and $Ne^{+}(2s^{-1}) \rightarrow Ne^{+}(2p^{-1})$ transitions is required. We performed this computations by means of the multi-reference configuration interaction (MRCI) method implemented in the MOLPRO 2010.1 package [76]. We restricted the configuration space for the initial state at the $1h$ plus $2h1p$ and for the final state at the $1h$ level with respect to the M^{q+} and Ne Hartree-Fock references, respectively.

3.6.4 Basis sets for electronic structure calculatios

The cc-pCVTZ basis set on magnesium and aug-cc-pVTZ basis set on oxygen and hydrogen atoms were utilized for geometry optimization of the $Na^{+}{\cdot}(H_2O)_4$ and $Mg^{2+}{\cdot}(H_2O)_6$ clusters [78,106]. The aug-cc-pVQZ on all atoms were utilized for geometry optimization of the $Ne{\cdot}H_2O$ cluster [78]. In calculations of the ionization energies in $Na^{+}{\cdot}(H_2O)_m$, $Mg^{2+}{\cdot}(H_2O)_n$ and $Ne{\cdot}H_2O$ clusters cc-pCVTZ basis sets on neon [78] and metal atoms as well as aug-cc-pVTZ basis sets on oxygen and hydrogen atoms were used.

In decay width calculation cc-pCVTZ basis sets on neon, metal and oxygen atoms as well as cc-pVTZ basis set [99] on hydrogen atoms were utilized. For an improved description of the ADC pseudocontinuum we added $2s2p2d1f$ KBJ basis functions [82] oxygen, $1s1p1d$ on hydrogen, and $2s2p2d1f$ on sodium in the case of $Na^{+}{\cdot}(H_2O)_m$ clusters. In the case of $Mg^{2+}{\cdot}(H_2O)_n$ clusters $3s3p3d1f$ KBJ basis functions on oxygen, $1s1p1d$ on hydrogen, and $1s1p1d1f$ basis on magnesium were added. In singly coordinated clusters additional $4s4p4d$ ($Na^{+}{\cdot}H_2O$) and $3s3p3d$ ($Mg^{2+}{\cdot}H_2O$) KBJ basis functions were placed midway between the metal and the oxygen atoms as well as at the geometrical center of the water molecule to improve the convergence of the Stieltjes renormalization procedure. The midway basis functions also improve the description of the electronic density on the water molecule polarized by the metal cation [79]. For larger clusters, the basis functions at the center of the water molecule were removed due to numerical limitations. The calculation of decay widths in $Ne{\cdot}H_2O$ included $5s5p5d1f$ KBJ basis functions on neon and oxygen, $2s2p2d$ on hydrogen, and $2s2p2d$ midway between the neon and oxygen atoms and at the geometrical center of the water molecule.

4 One-photon double ionization via ETMD

4.1 ETMD in the He·Mg cluster

One-photon double ionization is an important tool for studying electron correlation in atomic and molecular physics [107]. This can be deduced from the fact that simultaneous emission of two electrons via interaction with the one-electron dipole operator is not possible and has to occur due to electron correlation. In this context, two mechanisms representing different photon energy regimes, are used to visualize the double ionization process [108]. The so-called knock-out mechanism, is operative at photon energies close to the double ionization threshold. It involves emission of a slow first electron induced by the interaction with the photon. The subsequent removal of the second electron occurs due to the interaction between the leaving and the remaining electrons in the system. In this regime it is the electron correlation in the final state of the double ionization which plays the decisive role. In contrast, the so-called shake-off mechanism is operative at high photon energies, where a sudden ionization of the first electron takes place. The ionized system is not in in an eigenstate and there is a finite probability to populate an ionic continuum state, i.e. to emit a second electron. Electron correlation present in the system prior to the interaction with the photon facilitates the double ionization in this regime.

The one-photon double ionization is a correlation driven two-electron process which has to compete with the efficient one-electron process of single ionization. Therefore, the double-to-single photoionization ratios lie at typically few percents only for metal atoms such as magnesium [109,110]. Surprisingly, ETMD might be used to increase the effectiveness of the double ionization process. In this chapter we will visualize the enhancement for the magnesium atom weakly bound to a helium neighbor. Removing an electron from the helium atom by photoionization initiates a relaxation via ETMD(2), which leads to the neutralization of the helium and the double ionization of the magnesium:

$$\mathrm{He}\cdot\mathrm{Mg} + h\nu \rightarrow \mathrm{He}^{+}\cdot\mathrm{Mg} \xrightarrow{ETMD(2)} \mathrm{He}\cdot\mathrm{Mg}^{2+} + \mathrm{e}_{ETMD(2)} \tag{4.1}$$

The ETMD process is energetically allowed given the high electron affinity of the He^+ cation (24.6 eV) and the low double ionization potential (DIP) of magnesium (22.7 eV). The joint process shown by Eq. 4.1 can be considered as an one-photon double ionization of magnesium. It is a sequence of an efficient one-electron helium photoionization and a two-electron ETMD process. Hence, an increase of the double-to-single ionization

Parts of this chapter have been already published in
V. Stumpf, N. V. Kryzhevoi, K. Gokhberg and L. S. Cederbaum, Phys. Rev. Lett. **112**, 193001 (2014). Copyright 2014, American Physical Society.

ratio can be expected for magnesium atom attached to helium if ETMD has no strong competitors. Again, it is the interatomic correlation between the transferred and the emitted electrons in the ETMD process that drives the double ionization of magnesium.

The only process competing with ETMD after the photoionization of helium is the radiative charge transfer (RCT):

$$\mathrm{He}\cdot\mathrm{Mg} + h\nu \rightarrow \mathrm{He}^{+}\cdot\mathrm{Mg} \xrightarrow{RCT} \mathrm{He}\cdot\mathrm{Mg}^{+} + h\nu_{E}, \tag{4.2}$$

accompanied by the emission of a photon with the frequency ν_{E}. Both ETMD and RCT processes involve an electron transfer and are expected to be slow at the equilibrium geometry. Thus, we are interested in the ETMD-RCT branching ratio and its alteration due to the impact of the nuclear dynamics. We consider the photoionization in the photon energy range between 24.6 and 54 eV. There are no resonant excitations for the isolated atoms in this range and the atomic electronic structure is assumed to be only weakly modified by the presence of the neighbor [111].

4.1.1 Discussion

We start by inspecting the properties of the electronic ground state in the He·Mg cluster. It is a typical weakly bound system, the binding energy being only 5.6 meV and the equilibrium interatomic distance relatively large (R_{Eq} = 5.15 Å, see Fig. 4.1). The very weak attractive interaction leads to a broad probability density distribution of interatomic distances which has a width of 2.7 Å while the distribution's maximum is shifted to the interatomic distance of 5.98 Å. Assuming instantaneous photoionization the vibrational wave packet is vertically promoted from the He·Mg into the He^{+}·Mg and He·Mg^{+} states [112]. Additionally, a direct one-photon double ionization may populate the He·Mg^{2+} state. We estimate the relative populations of the He^{+}·Mg, He·Mg^{+} and He·Mg^{2+} in the 24.6-54 eV photon energy range from the atomic photoionization cross sections [109,113] as approximately 3000:100:1, given the weak interaction and the large interatomic distance between the monomers.

The minimum of the He^{+}·Mg potential energy curve (PEC) is shifted relatively to the ground state towards a lower value of 3.15 Å, expressing the attractive charge-induced dipole interaction of the hole on helium with the highly polarizable magnesium atom. Hence, nuclear dynamics will set on immediately after the population of the He^{+}·Mg state and accompany the ETMD and RCT processes. At the equilibrium geometry ETMD dominates RCT by approximately two orders of magnitude being by itself rather slow with a lifetime of 4.8 ns^{-1}. The comparison with the characteristic vibrational frequency of 4.7 ps^{-1} shows that in contrast to ICD [6,34], ETMD is not able to compete with nuclear dynamics. A reduction of the interatomic distance caused by the movement of the nuclei increases the efficiency of both ETMD and RCT due to the exponentially growing electronic overlap between the atomic centers [8]. Nevertheless, in the whole classically allowed range of interatomic distances (i.e. up to the left classical turning point R_{TP} = 2.41 Å), ETMD remains the dominant electronic relaxation mechanism (see Fig. 4.1, upper panel).

We expect ETMD to take place mostly at R_{TP}, where the ETMD lifetime is reduced to approximately 100 fs. In contrast to ICD, ETMD after single ionization does not

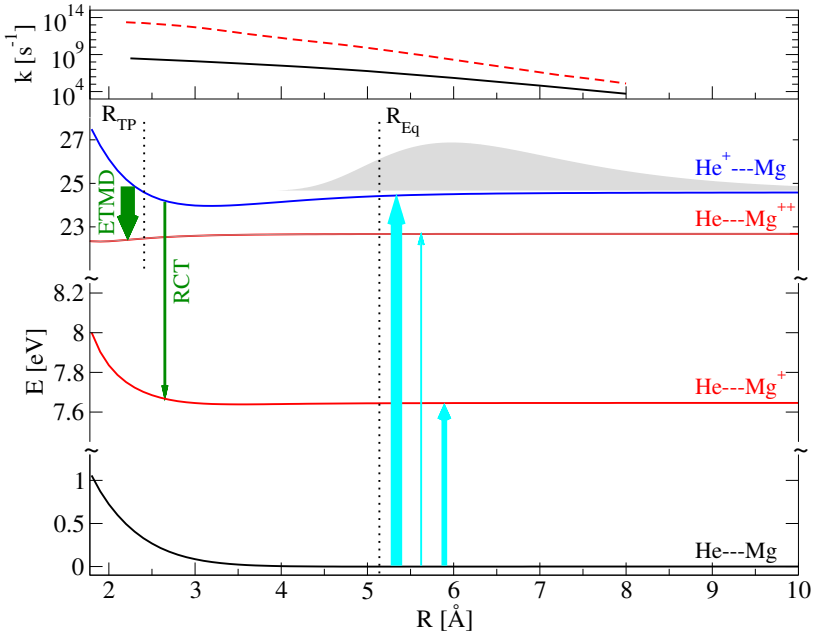

Figure 4.1: Potential energy curves and decay rates involved in the one-photon double ionization of magnesium in the He·Mg cluster. In the photon energy range between 24.6 and 54 eV, the photoionization of the electronic ground state of He·Mg (black curve) predominantly populates the He^{+}·Mg state (as indicated by the size of the upwards pointing arrows). The latter subsequently decays via competing ETMD and RCT mechanisms; the associated decay rates are displayed by the full black and dashed red lines in the upper panel, respectively. The equilibrium interatomic distance R_{Eq} and the classical turning point R_{TP}, where ETMD is the most efficient, are indicated by dashed vertical lines. Reprinted with permission from Ref. [114]. Copyright (2014) by the American Physical Society.

yield a pair of positively charged fragments. Hence, a characterization of the decay process by ion-ion-electron coincidence techniques, as it has been performed for ICD in van-der-Waals dimers [10, 115], is not possible. The energy of the emitted ETMD electrons at the classical turning point lies at 2.1 eV, while in total an energy range of 1.3-2.1 eV is covered. One should keep in mind that the energy sharing between the two emitted electrons is significantly different in the direct and the ETMD-assisted double ionization pathways. In the former case, the so-called knockout mechanism implies emission of a first electron and a knockout of a second electron by the first, the excess energy being shared by both electrons. In the latter case, the energy of the photoelectron grows linearly with the photon energy, if the photoelectron is sufficiently fast to avoid deceleration due to the so-called post-collision interaction [24]. Under the same conditions, the energy of the ETMD electron is independent of the photon energy and is determined by the energy difference between initial and final states at the classical turning point. These features could be exploited in experiments recording ion-electron-electron coincidences to distinguish both pathways of double ionization. To find how efficient is the indirect mechanism, we define the double-to-single ionization ratio for magnesium achieved in the photoionization of He·Mg by the following expression:

$$\mathcal{R}(cluster) = \frac{\sigma_{Mg^{2+}} + \sigma_{He^{+}}\Gamma_{ETMD}/\Gamma_t}{\sigma_{Mg^{+}} + \sigma_{He^{+}}\Gamma_{RCT}/\Gamma_t}, \tag{4.3}$$

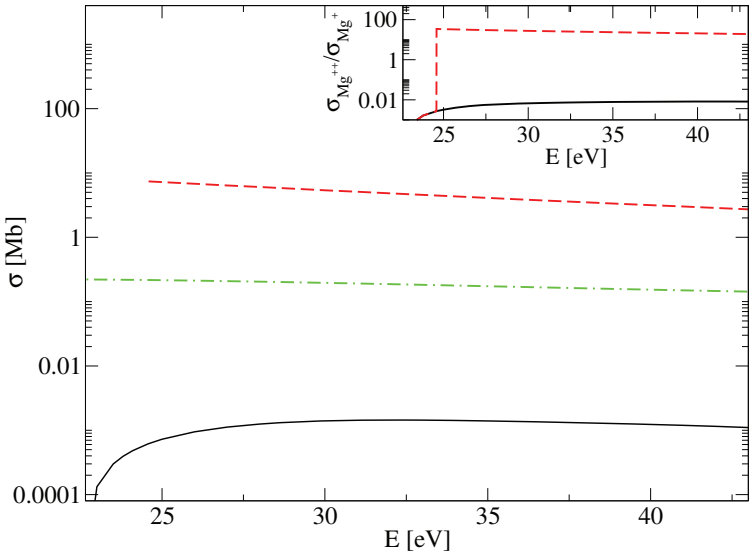

Figure 4.2: One-photon ionization cross sections of magnesium being in the atomic state and weakly bound to a helium neighbor. For the isolated atom, the double ionization cross section is indicated by the solid black line. The single ionization cross section is assumed to be identical for the isolated and bound states and is displayed by the green dashed-dotted line. The double ionization cross section of the bound atom is indicated by the red dashed line. Note the similarity of this cross section to the photoionization cross section of helium [113]. The inset shows the one-photon double-to-single ionization ratio for bound magnesium computed using the Eq. 4.3. Reprinted with permission from Ref. [114]. Copyright (2014) by the American Physical Society.

where the atomic photoionization cross sections are denoted by σ_{He^+}, σ_{Mg^+} and $\sigma_{Mg^{2+}}$. The ETMD, RCT and the total decay widths of He^+·Mg are given by Γ_{ETMD}, Γ_{RCT} and Γ_T, respectively. Utilizing experimental values for the atomic photoionization cross sections [109, 113], we calculated the $\mathcal{R}(cluster)$ value in the energy range of interest (see the inset of Fig. 4.2). The enhancement of the double-to-single ionization ratio relative to the isolated atoms sets on immediately above the helium ionization threshold and is as large as three orders of magnitude. To explain this behavior, we plotted the atomic photoionization cross sections together with the double ionization cross section of magnesium in the He·Mg cluster (following the expression in the denominator of Eq. 4.3). We notice that because of the higher cross section helium is more likely to be ionized by the photon than magnesium. Furthermore, due to the dominance of ETMD over RCT the double ionization cross section of magnesium is virtually identical to the photoionization cross section of helium. Applying the same argument, further enhancement of double ionization can be achieved by attaching additional helium neighbors to the magnesium atom.

The indirect double ionization mechanism discussed above is not restricted to metal atoms. Molecules with a low double ionization potential, e.g. polyacenes fulfill the requirements to undergo ETMD in the presence of the helium cation. Thus, naphtalene has a DIP of 21.4 eV, in anthracene the DIP is decreased to 20.1 eV while for the larger

polyacenes it is below 19 eV [28]. The double ionization enhancement is expected to be weaker compared to the metal atoms since the double-to-single photoionization ratios are higher for polyacenes and tend to grow with the size of the molecule. Increasing the number of helium neighbors may remedy for this fact. Replacing helium neighbors with neon atoms having a high ionization potential (IP) of 21.6 eV and up to 4-fold higher photoionization cross section [113] would be another alternative for larger polyacenes.

4.2 ETMD of magnesium clusters embedded in helium nanodroplets

To verify if the enhancement of the one-photon double ionization presented in the previous chapter takes place in large helium clusters, LaForge et al. performed an experiment on photoionization of magnesium-doped helium nanodroplets [116]. The latter are ultracold ($T < 1$ K), superfluid aggregates of helium atoms (10^3-10^8) which can be loaded with atomic and molecular dopants [29]. The dopants are picked up from the gas phase and cooled by evaporation of helium atoms from the nanodroplets. Sequential pickup schemes provide complexes and molecules of specific composition [29, 117]. Being inert and weakly perturbing, the nanodroplets serve as a unique matrix for spectroscopic and photophysical studies of the embedded species [30]. In this context, the transparency in the range from IR to photon energies of the lowest electronic excitations (20 eV) is of great importance.

At higher photon energies, electronic excitation and ionization of the nanodroplets give rise to electronic relaxation processes. In pure nanodroplets ICD occurs after multiple excitation [118]. In doped nanodroplets ICD between the singly excited nanodroplets and the dopant may occur [119]. Ionization of nanodroplets at photon energies above 24.6 eV has been shown to induce an electron transfer from the dopant [120]. In these studies double ionization energy of the dopant was higher than the electron affinity of the ionized droplet. LaForge et al. intended to initiate ETMD by the photoionization of nanodroplets doped with magnesium atoms and clusters. We performed *ab initio* calculations of ETMD electron energies in small $He{\cdot}Mg_n$ and $He_2{\cdot}Mg_n$ (n =1-3) model clusters to support the interpretation of the experimental spectra.

4.2.1 Discussion

In their experiment LaForge et al. generated nanodroplets of size 10^3-10^5 and subsequently doped them with 1 to 25 magnesium atoms. The size of the droplets was controlled via the temperature of the helium source while the amount of the dopant was given by the droplet size and the temperature (i.e. vapor pressure) of the magnesium oven. The doped droplets were ionized in a synchrotron beamline at photon energies between 24.6 and 40 eV, the charged products of the ionization (electrons and ions) were recorded. For the electrons the kinetic energy spectra, for the ions the mass spectra were generated. Ion-ion and ion-electron coincidences were extracted from the raw data.

Parts of this chapter have been already published in
A. C. LaForge, V. Stumpf, K. Gokhberg, J. von Vangerow, F. Stienkemeier et al., Rev. Lett. **116**, 203001 (2016). Copyright 2016, American Physical Society.

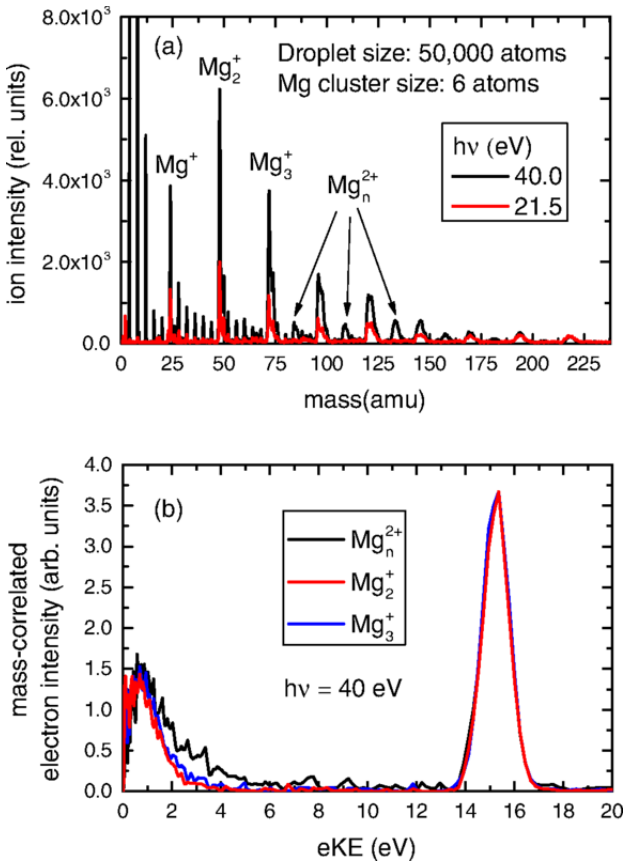

Figure 4.3: Products recorded after excitation (hν =21.5 eV) and photoionization (hν =40 eV) of helium nanodroplets doped with magnesium clusters. (a) Mass spectra, indicating formation of stable, doubly charged Mg_n^{2+} ions after the photoionization of the droplet. (b) Kinetic energy spectra of electrons measured in coincidence with these ions (black line). Reprinted with permission from Ref. [116]. Copyright (2016) by the American Physical Society.

First evidence for double ionization via ETMD after the photoionization of the nanodroplet is given by the mass spectra (see Fig. 4.3) belonging to a nanodroplet doped on average with six magnesium atoms. At even values of n the Mg_n^{2+} signals can not be distinguished from the Mg_m^+ series. For $n = 7, 9, 11$ a series of doubly ionized magnesium clusters Mg_n^{2+} is visible in the spectrum while for $n = 5$ the overlap with the $He_l Mg_2^+$ series makes the interpretation of the signal at 60 amu ambiguous. These findings are in agreement with a former study on the stability of doubly ionized magnesium clusters, where five was the minimum cluster size detected by mass spectrometry [121]. The fact that for photon energies lower than 20 eV no magnesium signal can be observed in the mass spectra (see Fig. 1 in Ref. [116]) implies that the Mg_n^{2+} ions are produced solely after the ionization of the nanodroplet. Under such conditions, ETMD appears as the most efficient mechanism to yield the Mg_n^{2+} ions:

$$He_d \cdot Mg_n + h\nu \rightarrow He_d^+ \cdot Mg_n \xrightarrow{ETMD} He_d \cdot Mg_n^{2+} + e_{ETMD}, \tag{4.4}$$

where He_d denotes the helium environment of the magnesium cluster in a nanodroplet.

Taking into account the lacking stability of the Mg_n^{2+} clusters for $n < 5$, singly charged Mg_m^+ fragments with $m < 4$ are likely to be produced by ETMD as well. An alterna-

tive source of such fragments is the charge transfer from the dopant to the ionized nanodroplet as has been demonstrated for alkali metals [120]. An ion-ion coincidence measurement of the Mg_m^+/Mg_l^+ ion pairs provides a possibility to discriminate between the charge transfer and ETMD mechanisms since only the latter produces two ions simultaneously. In the Fig. 4.4, an ion-ion coincidence map for nanodroplets doped with on average five to six magnesium atoms is shown. One can see that Mg_m^+/Mg_l^+ ion pairs are indeed readily produced by ETMD.

The experimental setup furthermore permits an extraction of electron-ion coincidences for a desired ion signal. The electron spectrum recorded in coincidence with the intact Mg_n^{2+} ions is shown in the Fig. 4.3. Two energetically well separated peaks appear in the spectrum. The high-energy peak at 15.4 eV can be clearly identified as the helium photoelectron peak. The low-energy peak is centered around approximately 1.0 eV; no comparable signal can be observed for nanodroplets containing one or no magnesium atoms inside (see Fig. 4.4). Hence, it can not be attributed to the scattering of photoelectrons in the droplet and is likely to occur due to ETMD. The electron spectrum correlated with the coincident Mg_m^+/Mg_l^+ ion pairs (see Fig. 4.4) exhibits a very similar structure. The only distinct feature is the shorter tail of the low-energy peak. Keeping in mind that the parent magnesium clusters yielding the Mg_m^+/Mg_l^+ ion pairs are smaller than those yielding stable Mg_n^{2+} ions, higher DIPs and slower ETMD electrons can be anticipated for the ion pairs.

The intensity of the low-energy peak in the electron spectrum correlated to Mg_m^+/Mg_l^+ ion pairs amounts to approximately 80 percent of the photoelectron peak intensity. If the ion-pairs are produced by ETMD only, equal number of ETMD electrons and photoelectrons are expected to be recorded in coincidence. However, the photoelectrons are highly abundant in the experiment as they are produced not only in coincidence with the considered ions but in *all* droplet photoionization events. Hence, a small percentage of the so-called false coincidences for the photoelectrons may be large in absolute terms and contribute considerably to the high-energy peak in the coincident electron spectrum. Taking into account this source of deviation, the electron spectrum seems to associate the appearance of Mg_m^+/Mg_l^+ ion pairs with the ETMD. To support these findings, we performed *ab initio* calculations of ETMD electron energies in small, symmetric $He{\cdot}Mg_3$ clusters mimicking the corresponding Mg_3 dopants in a helium nanodroplet. We aimed to reproduce the low-energy peak in the electron spectra correlated with the Mg^+/Mg_2^+ ion pair (see Fig. 4.4). The chosen symmetries of the $He{\cdot}Mg_3$ clusters are displayed in Fig. 4.5. Due to the weak interaction between the helium and the Mg_3 unit, the He·Mg interatomic distances are large and lie in the range of 4.2-5.2 Å. Therefore, we assumed a picosecond timescale for ETMD as in the case of the He·Mg cluster (see chapter 4.1). To account for the nuclear dynamics accompanying ETMD, we considered a symmetric movement of the light helium cation towards the heavier Mg_3 moiety after the photoionization of helium. Along this coordinate we determined the classical turning points, displayed by the structure in Fig. 4.5. The ETMD electron energies calculated at the turning point geometries are compiled in the Tab. 4.1.

The large energy range of approx. 1.4-7.6 eV covered by the ETMD electrons results from a band of doubly ionized main and satellite states of Mg_n^{2+} with distinct localization of the positive charge. The energies of the ETMD electrons are comparable for the different geometries of $He^+{\cdot}Mg_3$, which can be explained by the model used here. Within

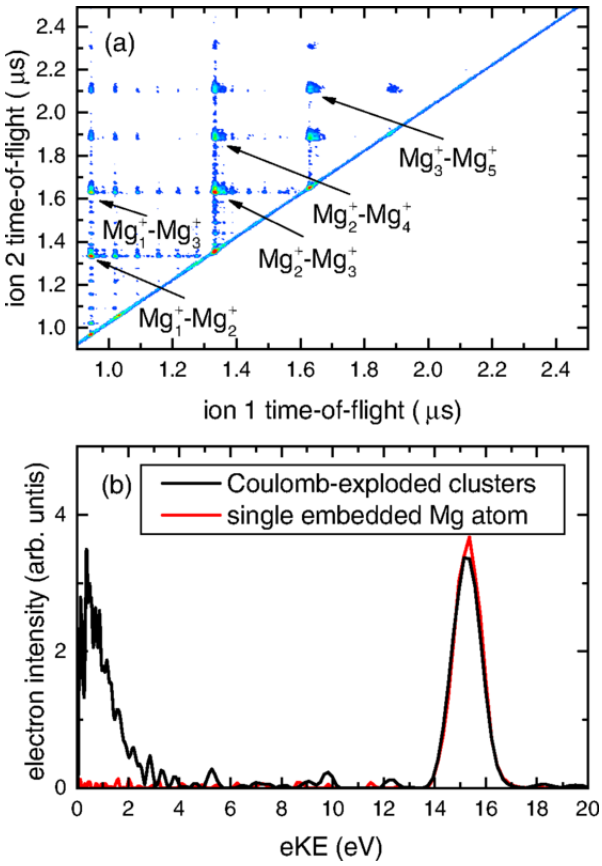

Figure 4.4: Products recorded in the ion-ion coincidence modus after photoionization (hν =40 eV) of helium nanodroplets doped with magnesium clusters. Nanodroplet size: 50000; average magnesium cluster size: 6. (a) Mg_m^+/Mg_l^+ ion pair coincidences (off-diagonal signals) indicating Coulomb explosions of doubly ionized, unstable Mg^{2+} clusters. (b) Kinetic energy spectra of electrons measured in coincidence with these ion pairs (black line). Note the difference to the spectrum obtained by photoionization of nanodroplets doped with a single magnesium atom and recorded in coincidence with the Mg^+ ion (red line). Reprinted with permission from Ref. [116]. Copyright (2016) by the American Physical Society.

our model, the energy of the initial ETMD state is determined at the turning point geometry of $He^+{\cdot}Mg_3$ and is per definition identical to the energy value at the equilibrium geometry of $He{\cdot}Mg_3$. Due to the large He·Mg equilibrium distances, the dependence of the initial state energy on the orientation of He^+ relatively to the Mg_3 unit is weak. On the other hand, the final state energies depend weakly on the orientation of helium as well, since it is only a weak perturber for the Mg_3^{2+} moiety.

The computed ETMD electron energies do not compare well with the experimental values as there is no significant contribution from electrons with energies above 3 eV in the experimental spectrum. Therefore, we have to reconsider our assumption of an inert helium environment for the $He^+{\cdot}Mg_3$ cluster embedded in the nanodroplet. It is known from earlier photoionization studies on helium nanodroplets that relaxed He_2^+ dimers can be formed in a time period as short as 60-80 fs [120]. To include such a scenario in our model, we considered ETMD of the $He_2^+{\cdot}Mg_3$ cluster (see Fig. 4.5) fixing the distance between the helium atoms at the equilibrium value of He_2^+ (R_{HeHe} = 1.08

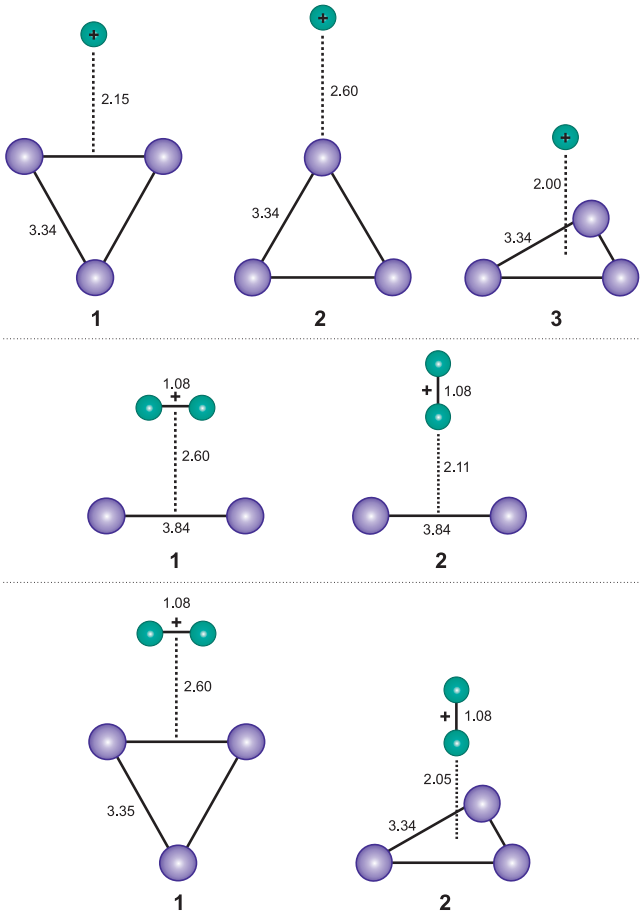

Figure 4.5: Structures of $He_m^+Mg_n$ clusters representing the classical turning point geometries for the movement of the light He^+ and He_2^+ ions towards the Mg_n moieties. Due to the high efficiency of ETMD, kinetic energies of the emitted electrons are determined at these geometries.

Å) [122]. The classical turning geometry was identified along the coordinate of the He_2^+ center of mass movement towards the center of mass of the Mg_3 moiety (see Fig. 4.5). The computed ETMD electron energies (see Tab. 4.1) are considerably lower compared to those in the $He^+{\cdot}Mg_3$ cluster. It is the very short distance between the helium atoms, which causes this energy shift. The electron affinity of He_2^+ is strongly reduced at such interatomic distances due to the strong repulsion in the neutral helium dimer. The scenario with the relaxation of the ionized helium dimer is in a better agreement to the experimental electron spectrum and should be inspected also for other sizes of the embedded magnesium clusters.

For the $He_2^+{\cdot}Mg_2$ clusters (see Fig. 4.5) the ETMD channels are open and the corresponding electron energies lie below 1 eV. Unfortunately, a comparison with the experimental spectrum is not possible since only pairs of ions having different masses can be detected in the coincidence experiment. For the $He_2^+{\cdot}Mg$ cluster the ETMD channel is closed, prohibiting the production of Mg^{2+} ions after the photoionization of helium. In the absence of open electronic decay channels the charge transfer from the

Table 4.1: ETMD electron energies of small, symmetric $He_m^+Mg_n$ clusters at geometries, where ETMD is assumed to be most efficient. For the assignment of the structures see Fig. 4.5.

Cluster	Geometry	E_{kin}(ETMD) [eV]
$He^+ \cdot Mg_3$	1	1.4-7.3
	2	1.8-7.6
	3	1.7-7.2
$He_2^+ \cdot Mg_2$	1	0.6-1.0
	2	0.6-0.9
$He_2^+ \cdot Mg_3$	1	0.4-2.3
	2	0.2-2.2

magnesium to the relaxed He_2^+ would result in a production of Mg^+ without electron emission. Interestingly, this finding explains why experimentally no low-energy electron signal has been detected in coincidence with Mg^+ ions produced by photoionization of nanodroplets doped with a single magnesium atom (see Fig. 4.4).

4.3 Conclusions

In this chapter we investigated the enhancement of the one-photon double ionization of a magnesium atom weakly bound to a helium neighbor. We demonstrated that the helium species acts as antenna, absorbing the photon and efficiently doubly ionizing the magnesium neighbor in an ETMD process. The indirect double ionization mechanism increases the double-to-single ionization ratio for the magnesium atom by three orders of magnitude.

An experimental verification of the enhanced one-photon double ionization was provided by the photoionization of helium nanodroplets doped with magnesium clusters. Intact doubly ionized Mg_n^{2+} clusters as well as coincident Mg_m^+/Mg_l^+ pairs of ions were detected above the photoionization threshold of the helium nanodroplets. Moreover, neutralization of the ionized nanodroplet via ETMD provided information about the structure of the charged helium species by measuring the kinetic energy of the emitted electron. This is in contrast to previous charge transfer studies in ionized helium nanodroplets [120] where the species carrying the excess energy (e.g. a photon in RCT) were not recorded.

5 ETMD of multiply charged cations produced via Auger decay in rare gas clusters

5.1 ETMD of Ne cations after KLL Auger decay in Ne·Xe

Interaction of X-Rays with atoms predominantly leads to the ionization of core electrons if the energy of the photons exceeds the core ionization threshold. The preference for the core ionization is a consequence of the low valence ionization cross sections at high photon energies [123]. The core-ionized states are highly energetic, metastable and undergo fast relaxation. For light chemical elements, the non-radiative Auger decay is the dominant relaxation pathway. It involves a reorganization of electrons in the occupied orbitals and the emission of a fast electron on a timescale of a typically few femtoseconds. As the result a doubly charged cation is formed, although emission of more than two electrons in the double Auger process is also possible [124]. In heavier atoms with several electronic shells removal of a core electron may initiate a cascade of Auger steps, where several electrons are emitted and a higher positive charge is accumulated. A conspicuous feature of both X-ray absorption and the Auger decay is that they are local in nature and occur mostly on a selected atom or molecule, even if this atom or molecule is in a cluster or solution.

Most of the cationic states populated in the Auger decay have vacancies in the outer-valence orbitals. We will inspect more closely the Auger decay in the neon atom which takes place after its $1s$ ionization (see Tab. 5.1). We neglect the competing relaxation of the core hole via photon emission due to the low branching ratio (≈ 1 % [126]). Both the Auger (94%) and the double Auger (6%) processes occur resulting in Ne^{2+} and Ne^{3+} ions [126]. The dicationic ground state $Ne^{2+}(2p^{-2}\ ^3P)$ is not populated in the Auger decay due to symmetry restrictions, therefore, the populated Ne^{2+} states possess excess energy and are metastable. When isolated, these neon dications can only de-excite via photon emission, which takes place on a timescale of 0.1 ns or slower [111]. The dications embedded into a chemical environment, for example if produced them in a cluster, may decay in an efficient, electronic pathway. Dications with a sufficiently high excess energy, i.e. those being in the $Ne^{2+}(2s^{-1}2p^{-1}\ ^1P)$, $Ne^{2+}(2s^{-1}2p^{-1}\ ^3P)$ and $Ne^{2+}(2s^{-2}\ ^1S)$ states may decay by ICD. ICD typically occurs on a femtosecond timescale and is able to

Parts of this chapter have been already published in
V. Stumpf, S. Scheit, P. Kolorenč and K. Gokhberg, Chem. Phys.,
http://dx.doi.org/10.1016/j.chemphys.2016.08.018 (2016).

Table 5.1: Relative populations of the Ne^{q+} cationic states produced in the KLL Auger [125] and KLLL double Auger [124, 126] decay of Ne. For cations embedded into a chemical environment the excess energies (EE) and maximum electron affinities (EA) provide information about available interatomic relaxation mechanisms. Highly excited cations efficiently decay via ICD, energetically low-lying dications may decay by ETMD due to the high electron affinity.

Ne^{q+}	El. State	Auger Pop. [%]	EE [eV]	EA [eV]	Decay mode
Ne^{3+}	$2p^{-3}$ (^{4}S, ^{2}D, ^{2}P)	2.5	0.0-7.7	63.4-71.1	ETMD
	$2s^{-1}2p^{-2}$ (^{4}P, ^{2}D, ^{2}S, ^{2}P)	3.0	22.8-39.7	86.2-103.1	ETMD, ICD
	$2s^{-2}2p^{-1}$ ^{2}P	0.5	60.2	123.6	ICD
Ne^{2+}	$2p^{-2}$ ^{3}P	0.0	0.0	41.0	ETMD
	$2p^{-2}$ ^{1}D	57.5	3.2	44.1	ETMD
	$2p^{-2}$ ^{1}S	9.1	6.9	47.8	ETMD
	$2s^{-1}2p^{-1}$ ^{3}P	5.7	25.3	66.3	ICD
	$2s^{-1}2p^{-1}$ ^{1}P	16.0	35.9	76.8	ICD
	$2s^{-2}$ ^{1}S	5.7	59.3	73.4	ICD

quench the slower photon emission. The Auger-ICD cascade was theoretically predicted by Santra et al. [31] and later verified in coincidence experiments in core-ionized rare gas dimers [32].

For the majority of the dications which are in $Ne^{2+}(2p^{-2}\ ^1D)$ and $Ne^{2+}(2p^{-2}\ ^1S)$ electronic states the excess energy is so small that the ICD channel is closed for any realistic environment. Nevertheless, due to the high positive charge, these low-lying states are characterized by a high electron affinity of more than 44 eV. Hence, in a chemical environment an electron transfer to the dications follows the Auger decay. This process releases an excess energy which has to be given to a third body to ensure energy conservation and to render the process irreversible. Therefore, the electron transfer is typically coupled either to the emission of a photon (radiative charge transfer [127]) or to the movement of the nuclei (Marcus electron transfer [3]). An alternative, purely electronic dissipation mechanism is provided by ETMD. The energy released by the transfer of the first electron is utilized to remove a second electron from the environment into the electronic continuum. From the dications' point of view ETMD, as any other electron transfer mechanism, leads to its partial *neutralization* reducing its charge by one. For the system as a whole the total charge increases by one but it becomes less localized.

To gain better understanding of this ETMD driven neutralization mechanism we would like to study it in a system where it can be investigated in detail by both computational and experimental techniques. A suitable class of systems for this purpose are the rare gas clusters which have been widely used in studies of the interatomic electronic decay [128]. They are produced by the ultrasonic expansion of the pure gases or gas mixtures, a technique which allows to control the cluster size distribution and composition. In contrast to molecular clusters, in rare gas clusters the products of Coulomb explosions which follow the interatomic decay are mostly atomic, reducing the complexity of

the coincidence spectra. Given the weak interactions between the rare gas atoms the clusters largely retain the closed-shell electronic structure in the neutral ground state. From the computational point of view, single-determinant based approaches, such as the ADC method, can be efficiently applied to calculating ionized and excited states involved in the electronic decay.

Rare gas dimers are the smallest such clusters and for them the observables of the interatomic decay can be determined with the highest possible level of accuracy both computationally and experimentally. The most prominent example is the investigation of ICD in the neon dimer. A detailed theoretical study [86] motivated a coincidence experiment [10], which verified the mechanism. On the other hand, the experimental results revealed discrepancies with the computed spectra and led to refined calculations [34]. Thus, the collaboration between the experimentalists and the theoreticians helped to understand basic features of ICD and to improve the computational methods. Importantly, this well studied dimer provided later an ideal system for complicated optical pump-probe experiments designed to follow ICD as it progressed in time [25].

The only rare gas dimer where ETMD is energetically allowed after a single step Auger decay is Ne·Xe:

$$\begin{aligned} &\mathrm{Ne}\cdot\mathrm{Xe} + h\nu \rightarrow \mathrm{Ne}^{+}(1s^{-1})\cdot\mathrm{Xe} \xrightarrow{Auger} \mathrm{Ne}^{2+}(2p^{-2})\cdot\mathrm{Xe} \\ &\xrightarrow{ETMD} \mathrm{Ne}^{+}(2p^{-1})\cdot\mathrm{Xe}^{2+}(5p^{-2}) + \mathrm{e}_{ETMD}. \end{aligned} \tag{5.1}$$

We do not wish to consider multistep Auger cascades in rare gas dimers since the corresponding product distribution is more complex. This would noticeably reduce the populations of individual states and complicate the analysis of the experimental spectra. From the computational point of view it also implies analysis of triply and higher ionized states, for which no methods to compute the decay widths are currently available. Therefore, we think that the Ne·Xe dimer is the simplest system where ETMD after Auger decay can be investigated in detail.

The products of ETMD in Ne^{2+}·Xe undergo a Coulomb explosion and offer a possibility to detect in an experiment the charged Ne^{+} and Xe^{2+} nuclei in coincidence with the ETMD and photoelectrons. In this way ETMD and ICD events which follow the Auger decay can be discriminated since in the latter Ne^{2+}/Xe^{+} pairs of ions are produced. Our aim is to motivate an experimental study of the ETMD-driven neutralization. To this end we compute the kinetic energy spectra of the ETMD electrons and the nuclei in the Ne·Xe dimer. In our calculations presented below we disregard the ETMD of Ne^{3+} cations produced by the double Auger decay of the core ionized neon due to the low population [126].

5.1.1 Potential energy curves

The non-relativistic PECs of the doubly ionized states of Ne·Xe which correlate with the decaying $Ne^{2+}(2p^{-2}\ {}^1\mathrm{D})$·Xe and $Ne^{2+}(2p^{-2}\ {}^1\mathrm{S})$·Xe state multiplets are shown in Fig. 5.1. The five PECs of Σ, Π and Δ symmetries which correspond to the former multiplet are virtually degenerate for all interatomic distances but the shortest. The PECs are bound and have the binding energies of 0.92 eV to 0.95 eV and the equilibrium distances ≈2.85 Å. The PEC of the $Ne^{2+}(2p^{-2}\ {}^1\mathrm{S})$·Xe ($\Sigma$) state has the binding energy

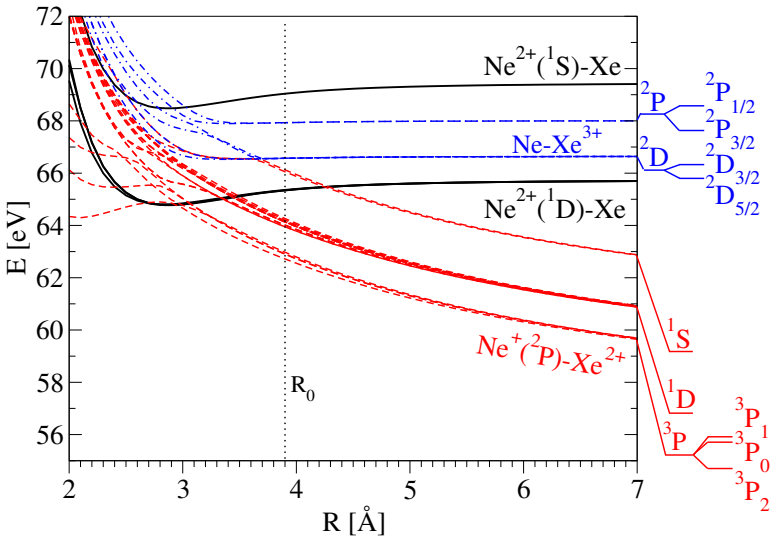

Figure 5.1: Non-relativistic *ab initio* diabatic PECs of the decaying $Ne^{2+}(2p^{-2})$·Xe states and adiabatic PECs of the final Ne^{+}·Xe^{2+} (dashed lines) and Ne·Xe^{3+} (dashed-dotted lines) states of ETMD. The PECs of the decaying states were shifted so as to match the experimental atomic energies as given in Ref. [111] at asymptotic separations. All final states were uniformly shifted so that the PECs of the $Ne^{+}(2p^{-1}\ ^2P)$·$Xe^{2+}(5p^{-2}\ ^1D)$ match the asymptotic value available experimentally. The errors in the asymptotic energies of other states were < 0.54 eV. Note, that ETMD of the $Ne^{2+}(2p^{-2}\ ^1D)$·Xe state leads only to the appearance of the Ne^{+} and Xe^{2+} ions. The decay of the $Ne^{2+}(2p^{-2}\ ^1S)$·Xe state can also produce the Ne, Xe^{3+} pair. The dotted vertical line denotes the equilibrium distance R_0 of the Ne·Xe ground state. Reprinted from Ref. [129]. Copyright (2016), with permission from Elsevier.

of 0.95 eV at 2.90 Å. The photoionization and the subsequent Auger decay ($\tau_{Auger} = 2.7$ fs [125]) promote the vibrational wavepacket of the neutral ground state vertically into the decaying dicationic states. The minima of the PECs of both decaying state multiplets lie at shorter interatomic distances than the equilibrium distance $R_0 = 3.90$ Å in the electronic ground state of Ne·Xe. Therefore, we expect ETMD to be accompanied by nuclear dynamics leading to the contraction of the average interatomic distance.

The non-relativistic final states of ETMD correlate at large interatomic distances with the $Ne^{+}(2p^{-1}\ ^2P)$·$Xe^{2+}(5p^{-2}\ ^3P)$, $Ne^{+}(2p^{-1}\ ^2P)$·$Xe^{2+}(5p^{-2}\ ^1D)$ and $Ne^{+}(2p^{-1}\ ^2P)$·$Xe^{2+}(5p^{-2}\ ^1S)$ states. These states form three energetically well separated groups (see Fig. 5.1). Both $Ne^{2+}(2p^{-2}\ ^1D)$·Xe and $Ne^{2+}(2p^{-2}\ ^1S)$·Xe states decay into this manifold of final states emitting an electron and setting off the Coulomb explosion of the Ne^{+} and Xe^{2+} nuclei. Under the effect of the spin-orbit coupling the lowest group corresponding to the $Ne^{+}(2p^{-1}\ ^2P)$·$Xe^{2+}(5p^{-2}\ ^3P)$ states splits into three corresponding to the three atomic terms of $Xe^{2+}(5p^{-2})$: $^3P_2$, $^3P_0$ and $^3P_1$ (see Fig. 5.2).

The manifold of the final states of ETMD is made complicated by the appearance of the states of Ne·$Xe^{3+}(5p^{-3})$ character. Asymptotically these states lie only about 10 eV higher than the Ne^{+}·Xe^{2+} states. Their PECs lie above the ones of the $Ne^{2+}(2p^{-2}\ ^1D)$·Xe decaying state and are inaccessible from it in the electronic decay; however, the $Ne^{2+}(2p^{-2}\ ^1S)$·Xe state can electronically decay into these states. Such decay may be termed double ETMD, since two electrons are transferred from Xe to Ne, while the third one is emitted into continuum. Double ETMD which involves three electrons

of which two are transferred between atoms should be much slower than the normal ETMD which suggests that this channel might be neglected. However, the fast growing repulsive $Ne^+ \cdot Xe^{2+}$ states states cross and interact with the $Ne \cdot Xe^{3+}$ states leading to the appearance of a series of avoided crossings between 2 Å and 4 Å, i.e. exactly at interatomic distances where ETMD takes place. Thus ETMD might efficiently proceed into a $Ne^+ \cdot Xe^{2+}$ state to be followed by the separation of the nuclei on an adiabatic PEC such that it is Ne and Xe^{3+} which are produced and not Ne^+ and Xe^{2+}.

This shows that if high precision is desired in the description of ETMD spectra of the $Ne^{2+}(2p^{-2}\ ^1S) \cdot Xe$ state one needs the accurate knowledge of the positions of and coupling strengths at the avoided crossings between $Ne^+ \cdot Xe^{2+}$ and $Ne \cdot Xe^{3+}$ final states which can be obtained only in high level relativistic calculations. Moreover, to find accurate branching ratio of the decay into each of these two classes of final states calculation of the non-adiabatic nuclear dynamics in the final state is necessary. However, the decay of the $Ne^{2+}(2p^{-2}\ ^1S) \cdot Xe$ state proceeds mostly into the $Ne^+ \cdot Xe^{2+}$ manifold; the decay to the $Ne \cdot Xe^{3+}$ states remains weak. Therefore, in our computations of the spectra we rely on a model $Ne^+ \cdot Xe^{2+}$ final state manifold introduced in the next paragraph, while the decay into $Ne \cdot Xe^{3+}$ states will be discussed only qualitatively.

The PECs of the $Ne^+ \cdot Xe^{2+}$ final states behave very nearly as $2/R$ for the interatomic distances at which ETMD of the $Ne^{2+}(2p^{-2}\ ^1D) \cdot Xe$ multiplet takes place. Therefore, we replace the respective PECs via the $2/R$ curves and shift the latter individually so that each matches the respective experimental energies at the separated atoms limit (see Fig. 5.2). For the interatomic distances where ETMD into the respective final states is allowed the approximation works best for the PECs deriving from the $Ne^+(2p^{-1}\ ^2P) \cdot Xe^{2+}(5p^{-2}\ ^1S)$ states (cf. Figs. 5.1 and 5.2). The group of PECs corresponding to the $Ne^+(2p^{-1}\ ^2P) \cdot Xe^{2+}(5p^{-2}\ ^1D)$ state, which are degenerate at large interatomic distances, are not degenerate anymore at the distances where the ETMD of $Ne^{2+}(2p^{-2}\ ^1D) \cdot Xe$ takes place. However, the energy splitting amounts to a few hundred meV at most and will result in small changes of the spectral shape. Finally, for the $Ne^+(2p^{-1}\ ^2P) \cdot Xe^{2+}(5p^{-2}\ ^3P)$ state a similar degeneracy lifting and the appearance of the avoided crossing with a $Ne \cdot Xe^{3+}$ state should similarly have a small impact on the ETMD spectra. The spin-orbit interaction in the $Ne^+(2p^{-1}\ ^2P) \cdot Xe^{2+}(5p^{-2}\ ^3P)$ multiplet is the most important relativistic effect in the final states manifold. Since the overall shape of the PECs will be mostly determined by the Coulomb repulsion between Ne^+ and Xe^{2+} in the range of R relevant for ETMD, the impact of this interaction will be to split the corresponding group of states into three. We can also use this model to estimate the ETMD spectra obtained in the decay of the $Ne^{2+}(2p^{-2}\ ^1S) \cdot Xe$ state, although the expected result will be less accurate due to the more complex structure of accessible final state manifold.

We can immediately use the phenomenological model of the ETMD final states in Fig. 5.2 for a qualitative discussion of the ETMD spectra. Thus, ETMD of the $Ne^{2+}(2p^{-2}\ ^1D) \cdot Xe$ state into the $Ne^+(2p^{-1}\ ^2P) \cdot Xe^{2+}(5p^{-2}\ ^1S)$ channel becomes forbidden at $R = 4.5$ Å. Since the initial vibrational wavepacket is centered about $R_0 = 3.90$ Å, and the dynamics in the decaying state leads to the shortening of the average interatomic distance, the ETMD into this channel will be limited only to the exponential tail of the wavepacket and, thus, will be negligible. Therefore, ETMD proceeds mostly into the $Ne^+(2p^{-1}\ ^2P) \cdot Xe^{2+}(5p^{-2}\ ^1D)$ and $Ne^+(2p^{-1}\ ^2P) \cdot Xe^{2+}(5p^{-2}\ ^3P)$ channels which become closed at 3.45 Å and 3.05 Å, respectively. From the positions of the thresholds we

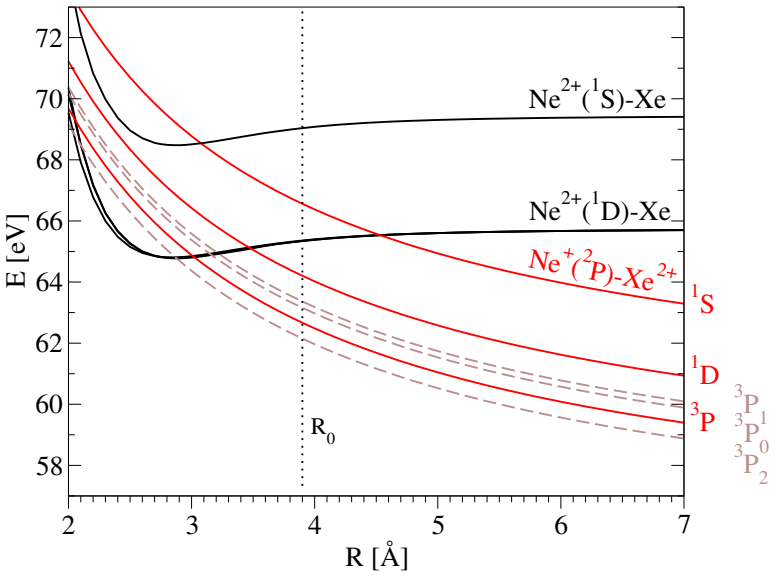

Figure 5.2: (Solid lines) Non-relativistic diabatic PECs of the decaying $Ne^{2+}(2p^{-2})$·Xe states and the PECs of the final Ne^{+}·Xe^{2+} states obtained using a phenomenological model. The final states are approximated by $2/R$ curves which have correct non-relativistic energies at the limit of the separated atoms. (Dashed lines) The $2/R$ curves corresponding to the spin-orbit split $Ne^{+}(2p^{-1}\ ^2P)$·$Xe^{2+}(5p^{-2}\ ^3P)$ states. The dotted vertical line denotes the equilibrium distance R_0 of the Ne·Xe ground state. Reprinted from Ref. [129]. Copyright (2016), with permission from Elsevier.

conclude that the electron spectra cut-off lies at 0 eV, while the maximum kinetic energy release (KER) for the nuclei available in the system is about 9.60 eV (10.10 eV if the spin-orbit splitting of the $Xe^{2+}(5p^{-2}\ ^3P)$ term is taken into account).

The decay from the $Ne^{2+}(2p^{-2}\ ^1S)$·Xe state is possible into all three ETMD channels. Only the $Ne^{+}(2p^{-1}\ ^2P)$·$Xe^{2+}(5p^{-2}\ ^1S)$ channel becomes closed at 3.05 Å, while the two other channels remain open for all interatomic distances of interest. Therefore, a large proportion of ETMD events will take place at the inner turning point $R_{in} \approx 2.45$ Å. The minimum electron energy expected in the decay of this state is, thus, about 0.55 eV, while the maximum KER is about 11.66 eV. The larger maximum KER in this case indicates that ETMD might take place at shorter interatomic distances compared to the case of the $Ne^{2+}(2p^{-2}\ ^1D)$·Xe state.

5.1.2 Total and partial ETMD widths

To obtain the full shape of the electron and KER spectra we first need to know the values of the total and partial ETMD widths for each decaying state. The total ETMD widths of the $^1\Sigma$, $^1\Pi$ and $^1\Delta$ terms which derive from the $Ne^{2+}(2p^{-2}\ ^1D)$·Xe multiplet are shown in Fig. 5.3. First we observe that for all but the shortest interatomic distances the widths show exponential behavior characteristic for the charge transfer driven processes. The sudden jumps at 4.55 Å, 3.45 Å, and 3.05 Å occur due to the closing of the $Ne^{+}(2p^{-1}\ ^2P)$·$Xe^{2+}(5p^{-2}\ ^1S)$, $Ne^{+}(2p^{-1}\ ^2P)$·$Xe^{2+}(5p^{-2}\ ^1D)$ and $Ne^{+}(2p^{-1}\ ^2P)$·$Xe^{2+}(5p^{-2}\ ^3P)$ channels. The total widths of the $^1\Sigma$ and $^1\Pi$ terms are very similar for all R in question and are up to two orders of magnitude larger than the width of the $^1\Delta$ term.

This ordering of the total decay widths can be explained by the different extent of the overlap between the hole density in Ne^{2+} and the valence electrons of Xe which determines the efficiency of the charge transfer. Thus, Ne^{2+} (p_σ^{-2}) and $(p_\sigma^{-1}p_\pi^{-1})$ are the leading configurations in the $^1\Sigma$ and $^1\Pi$ terms, respectively. The hole in the p_σ orbital overlaps well with the valence electrons on Xe facilitating ETMD. On the contrary, the hole density in the $^1\Delta$ term is described by the (p_π^{-2}) configuration and overlaps much less with the electron density on Xe.

We next consider more closely the behavior of the total widths in the region where the dynamics during ETMD takes place. The total widths of the three terms at R_0 are 0.298 meV (2.18 ps), 0.308 meV (2.11 ps), and 0.042 meV (15.47 ps) for the $^1\Sigma$, $^1\Pi$ and $^1\Delta$ terms, respectively. We notice that these ETMD lifetimes are at least an order of magnitude shorter than the lifetime of He^+-Mg at the respective equilibrium distance discussed in chapter 4.1. The lifetime reduction can be explained by a smaller interatomic equilibrium distance and an increased number of electrons on the neighbor which can participate in ETMD.

With the decreasing distance the ETMD widths grow, indicating that the neutralization process is expected to be enhanced by nuclear dynamics and to proceed on a picosecond to hundreds of femtoseconds timescale depending on the leading hole configuration in the decaying state. However, they do so non-monotonically due to the closing of the $Ne^+(2p^{-1}\ ^2P)\cdot Xe^{2+}(5p^{-2}\ ^1D)$ channel at 3.45 Å. This behavior leads to an interesting result that for the $^1\Pi$ and $^1\Delta$ terms the width reaches maximum not at the shortest distance at which the decay is possible but at the $Ne^+(2p^{-1}\ ^2P)\cdot Xe^{2+}(5p^{-2}\ ^1D)$ threshold. For the $^1\Sigma$ term the values of the width at both thresholds (denoted (3) and (2) in Fig. 5.3) are very close. Therefore, due to the closing of the channels the total width oscillates in the range of R where the nuclear dynamics takes place during ETMD.

The behavior of the partial decay width will be discussed only briefly. Since our methods do not always allow the construction of channel projection operators, one often approximates the partial decay width by dividing the total width through the number of available final states. This approximation may lead to noticeable errors; however, their impact on the measurable spectra will be small if the final states are nearly degenerate and do not interact with other states. Therefore, in our case it is sufficient to compute only the partial decay widths into the groups of nearly degenerate states correlating with the $Ne^+(2p^{-1}\ ^2P)\cdot Xe^{2+}(5p^{-2}\ ^1S)$, $Ne^+(2p^{-1}\ ^2P)\cdot Xe^{2+}(5p^{-2}\ ^1D)$ and $Ne^+(2p^{-1}\ ^2P)\cdot Xe^{2+}(5p^{-2}\ ^3P)$ multiplets. We could carry out such calculation of the partial widths only for the $Ne^{2+}(2p^{-2}\ ^1D)\cdot Xe$ decaying state. Interestingly, at $R \geq 4.55$ Å where all three channels are open the ratio of partial widths is 3.3:4.0:1.0 (averaged over the initial $Ne^{2+}(2p^{-2}\ ^1D)\cdot Xe$ multiplet) which should be compared to the ratio of final states multiplicities 9:5:1. At R_0 where the decay into the $Ne^+(2p^{-1}\ ^2P)\cdot Xe^{2+}(5p^{-2}\ ^1S)$ channel is forbidden the ratio of the partial decay widths into the two remaining channels is 6:5 compared to the 9:5 ratio of their multiplicities.

The behavior of the total ETMD width of the $^1\Sigma$ term deriving from the $Ne^{2+}(2p^{-2}\ ^1S)\cdot Xe$ state is also shown in Fig. 5.3. An important difference between the $\Gamma(R)$ which corresponds to this state and the states considered previously is that ETMD channels remain open for all R where the nuclear dynamics during ETMD takes place. This state is dominated by the (p_σ^{-2}) and (p_π^{-2}) configurations and, therefore, at larger R exhibits

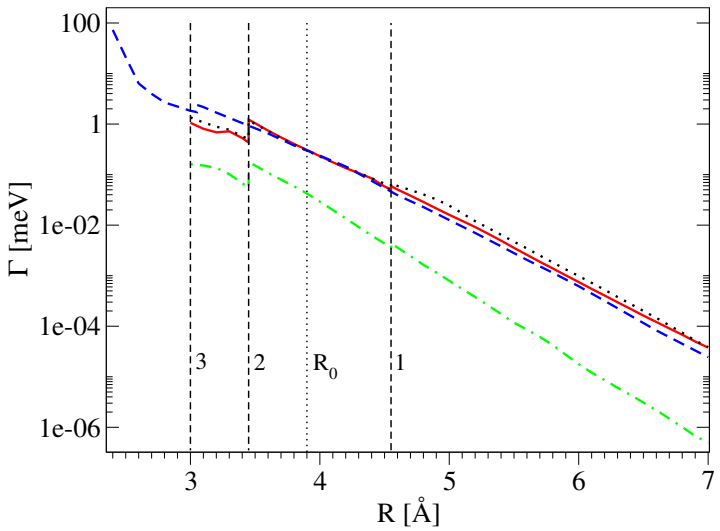

Figure 5.3: Total ETMD widths of the terms deriving from the $Ne^{2+}(2p^{-2}\ ^1D)$·Xe and $Ne^{2+}(2p^{-2}\ ^1S)$·Xe decaying states. (Dashed line) $^1\Sigma$ term derived from the $Ne^{2+}(2p^{-2}\ ^1S)$·Xe, (Dotted line) $^1\Sigma$ term, (Solid line) $^1\Pi$ term, (Dashed-dotted line) $^1\Delta$ term derived from the $Ne^{2+}(2p^{-2}\ ^1S)$·Xe multiplet. The numbered dashed vertical lines enumerate different channel thresholds in the decay of the $Ne^{2+}(2p^{-2}\ ^1D)$·Xe multiplet: (1) $Ne^+(2p^{-1}\ ^2P)$·$Xe^{2+}(5p^{-2}\ ^1S)$, (2) $Ne^+(2p^{-1}\ ^2P)$·$Xe^{2+}(5p^{-2}\ ^1D)$, (3) $Ne^+(2p^{-1}\ ^2P)$·$Xe^{2+}(5p^{-2}\ ^3P)$. The dotted vertical line denotes the equilibrium distance R_0 of the Ne·Xe ground state. Reprinted from Ref. [129]. Copyright (2016), with permission from Elsevier.

an overlap of Ne^{2+} with Xe and the total decay width slightly lower than the ones of the $^1\Sigma$, $^1\Pi$ terms of the $Ne^{2+}(2p^{-2}\ ^1D)$·Xe state. Up to the threshold at 3.05 Å the width behaves nearly exponential, while at shorter distances it is strongly enhanced due to the admixture of configurations of the $Ne^+(2p^{-1})$·$Xe^+(5s^{-1})$ character. At R_0 the total width is 0.30 meV (2.17 ps), however, at $R = 2.4$ Å the combined effect of the shorter interatomic distance and the electron delocalization between Xe and Ne^{2+} leads to the ETMD width of 72.91 meV (8.92 fs). To compute the partial widths in the decay of the $Ne^{2+}(2p^{-2}\ ^1S)$·Xe state we had to resort to dividing the total ETMD width through the weights of the final states multiplets. The definition of the channel projectors becomes difficult in this case due to the mixing of the Ne^+·Xe^{2+} and Ne·Xe^{3+} states. The computed partial widths ratios in the case of the $Ne^{2+}(2p^{-2}\ ^1\ )$·Xe multiplet allow us to estimate the errors incurred.

5.1.3 ETMD electron and KER spectra

Using the ETMD widths in Fig. 5.3 and the non-relativistic phenomenological PECs shown in Fig. 5.2 we computed ETMD electron and KER spectra plotted in Figs. 5.4 and 5.5, respectively. We also estimated the effect of the spin-orbit splitting on the spectra and found it to be limited as discussed in the last paragraphs of this section.

The easiest to interpret are the spectra of the $Ne^{2+}(2p^{-2}\ ^1S)$·Xe state.The KER spectrum (see Fig. 5.5(a)), which shows what is the probability for the decay to take place at a specific R, appears as a single narrow peak at 12 eV indicating that ETMD occurs predominantly at the inner turning point of the decaying state PEC at 2.45 Å.

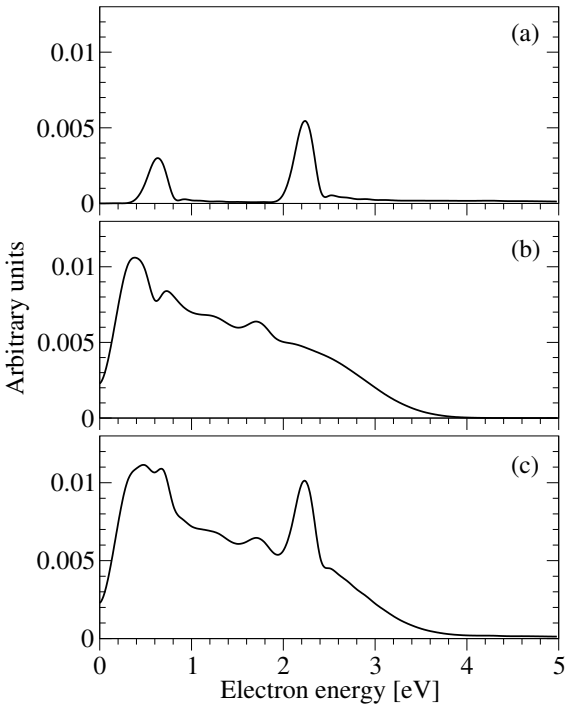

Figure 5.4: ETMD electron spectra computed using the final state manifold in Fig. 5.2. (a) Electron spectrum corresponding to the decay of the $Ne^{2+}(2p^{-2}\ ^1S)\cdot Xe$ state. (b) Electron spectrum corresponding to the decay of the $Ne^{2+}(2p^{-2}\ ^1D)\cdot Xe$ state. (c) Total electron spectrum obtained by summing the spectra in (a) and (b). The ratio of the integrated spectra in panels (a) and (b) corresponds to the ratio of the respective populations (1:6) of the ETMD decaying states reached in the Auger decay. Reprinted from Ref. [129]. Copyright (2016), with permission from Elsevier.

ETMD proceeds almost exclusively into the $Ne^+(2p^{-1}\ ^2P)\cdot Xe^{2+}(5p^{-2}\ ^1D)$ and $Ne^+(2p^{-1}\ ^2P)\cdot Xe^{2+}(5p^{-2}\ ^3P)$ channels which are open for all R of interest, while the decay into the $Ne^+(2p^{-1}\ ^2P)\cdot Xe^{2+}(5p^{-2}\ ^1S)$ channel is negligible. The decay into these two energetically separated channels is well visible in the ETMD electron spectrum (see Fig. 4(a)) as two sharp peaks at 0.7 eV and 2.2 eV, respectively. The narrow width of the peaks in both electron and KER spectra is due to the behavior of the total ETMD width which grows almost tenfold between the minimum of the decaying states PEC and the inner turning point.

The electron spectrum due to ETMD of the $Ne^{2+}(2p^{-2}\ ^1D)\cdot Xe$ state (see Fig. 5.4(b)) appears as one broad peak between 0 eV and 4 eV. The overwhelming contribution to this peak comes again from the decay into the $Ne^+(2p^{-1}\ ^2P)\cdot Xe^{2+}(5p^{-2}\ ^1D)$ and $Ne^+(2p^{-1}\ ^2P)\cdot Xe^{2+}(5p^{-2}\ ^3P)$ channels which become closed at distances smaller than R_0. The appearance of this spectrum which is so different from the spectra of the $Ne^{2+}(2p^{-2}\ ^1S)\cdot Xe$ state is due to the fact that none of the ETMD channels remains open for all R where nuclear dynamics take place. It leads to the behavior of the total width which we noted above - instead of reaching a maximum at the smallest available R it exhibits two maxima - one at each threshold.

Since the probability of the decay does not vary much in the interval of R where the nuclei move, it results in a broad distribution of the energies of the emitted electrons. Another consequence of this behavior of Γ is the appearance of the vibrational structure in the spectrum with the peaks at 0.4 eV and 1.8 eV corresponding to the decay close to the ETMD thresholds. Our calculations show that this structure is due to the decay into the $Ne^+(2p^{-1}\ ^2P)\cdot Xe^{2+}(5p^{-2}\ ^3P)$ channel (see Fig. 5.6). The KER spectrum due to the ETMD of the $Ne^{2+}(2p^{-2}\ ^1D)\cdot Xe$ state lies between 6.5 and 10.5 eV (see Fig. 5.5(b)) and is also quite structured. The peaks at approximately 8.6 and 10.2 eV correspond to the thresholds of the $Ne^+(2p^{-1}\ ^2P)\cdot Xe^{2+}(5p^{-2}\ ^1D)$ and $Ne^+(2p^{-1}\ ^2P)\cdot Xe^{2+}(5p^{-2}\ ^3P)$ channels, respectively. We see prominent peaks marking the channel thresholds due

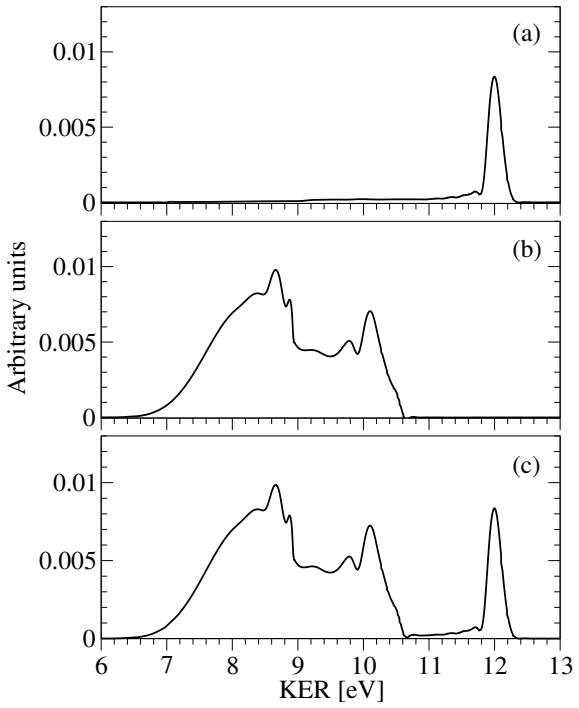

Figure 5.5: KER spectra computed using the final state manifold in Fig. 5.2. (a) KER spectrum corresponding to the decay of the $Ne^{2+}(2p^{-2}\ ^1S)\cdot Xe$ state. (b) KER spectrum corresponding to the decay of the $Ne^{2+}(2p^{-2}\ ^1D)\cdot Xe$ state. (c) Total KER spectrum obtained by summing the spectra in (a) and (b). The ratio of the integrated spectra in panels (a) and (b) corresponds to the ratio of the respective populations (1:6) of the ETMD decaying states reached in the Auger decay. Reprinted from Ref. [129]. Copyright (2016), with permission from Elsevier.

to the non-monotonic behavior of the total ETMD width which has maxima at the respective R. Moreover, these peaks are distinguishable in the KER spectra, since the thresholds lie at different values of the interatomic distance. Again a vibrational structure is visible in the spectrum due to the decay into the $Ne^+(2p^{-1}\ ^2P)\cdot Xe^{2+}(5p^{-2}\ ^3P)$ state.

Adding up the ETMD spectra of the $Ne^{2+}(2p^{-2}\ ^1D)\cdot Xe$ and $Ne^{2+}(2p^{-2}\ ^1S)\cdot Xe$ states we obtain the total ETMD electron (Fig. 5.4 (c)) and KER (Fig. 5.5(c)) spectra which should be observable in Ne·Xe following the Auger decay of the 1s-vacancy on Ne. One may immediately see that the two electron spectra overlap making it difficult to discern the contributions of ETMD from the different decaying states. The KER spectra, on the contrary, are well separated energetically with the sharp peak due to the ETMD of the $Ne^{2+}(2p^{-2}\ ^1S)\cdot Xe$ state clearly visible at 12 eV. This spectral structure offers a convenient opportunity to investigate the ETMD of the two decaying states independently. Thus, a measurement of slow electrons coincident with the Ne^+ and Xe^{2+} nuclei which have 12 eV of KER should give the electron spectrum in Fig. 5.5(a). The electron spectrum corresponding to the ETMD of $Ne^{2+}(2p^{-2}\ ^1D)\cdot Xe$ state can be obtained by collecting slow electrons coincident with the nuclei having 6 to 10.5 eV of KER.

We would also like to note that the PECs of Σ and Π symmetries corresponding to the lower lying $Ne^{2+}(2p^{-2}\ ^1D)\cdot Xe$ state multiplet cross at about 3.5 Å the respective PECs of the $Ne^+(2s^{-1}\ ^2S)\cdot Xe^+(5p^{-1}\ ^2P)$ state which is not populated directly in the Auger decay. Therefore, nuclear dynamics which is set off by the Auger decay may lead to the electron transfer and population of the $Ne^+(2s^{-1}\ ^2S)\cdot Xe^+(5p^{-1}\ ^2P)$ state. The latter is electronically unstable and decays by ICD into the same final states as ETMD. In addition to ICD, populating the $Ne^+(2s^{-1}\ ^2S)\cdot Xe^+(5p^{-1}\ ^2P)$ state leads to the Coulomb explosion of the cluster. Since ICD rate decreases fast with the interatomic distance the majority of ICD events will take place close to the crossing point resulting

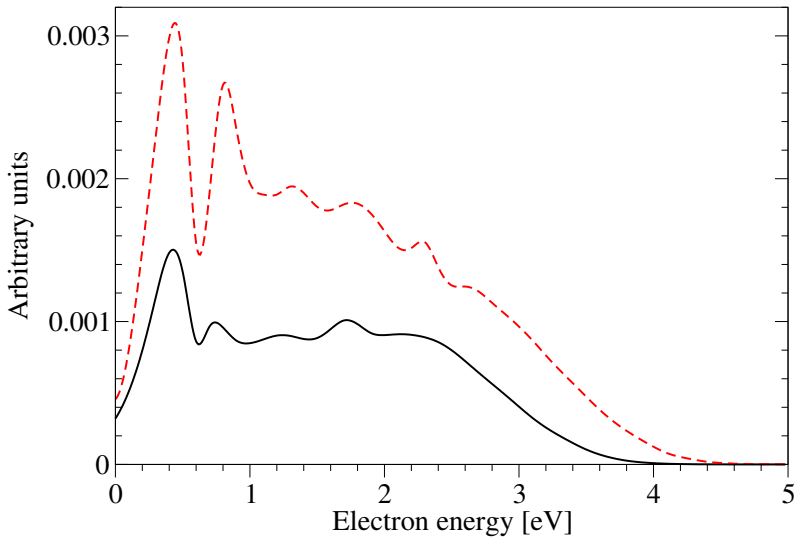

Figure 5.6: Comparison of the electron spectra obtained in ETMD of the $Ne^{2+}(2p^{-2}\ ^1S)\cdot Xe\ ^1\Sigma$ term into the $Ne^{+}(2p^{-1}\ ^2P)\cdot Xe^{2+}(5p^{-2}\ ^3P)$ channel with (dashed line) and without (solid line) taking into account the spin-orbit splitting of the $Xe(^{2+}5p^{-2}\ ^3P)$ multiplet. Note the vibrational structure visible in both spectra. Reprinted from Ref. [129]. Copyright (2016), with permission from Elsevier.

in the electrons of 0 to 1.6 eV and KER of about 8.2 eV. These values lie within the ETMD electron and KER spectra. Although the energy splitting due to the crossing was found to be 0.04 to 0.1 eV we assume the non-adiabatic coupling to be weak, since electron transfer is accompanied by the excitation of a $2s$ electron of Ne. Therefore, we do not expect that the signal from this sequential electron transfer-ICD process will be discernible in the experimental spectra. In general, non-adiabatic coupling to charge transfer states as discussed above is likely to appear for the multiply charged states decaying by ETMD and characterized by a large localized positive charge. However, the charge transfer state has necessarily to be highly excited since the non-adiabatic coupling occurs in the electronic continuum corresponding to the open channels. Thus, a charge transfer state is likely to decay via autoionization or ICD, yielding the same products as in the ETMD decay. We will return to this phenomenon in chapter 7, discussing interatomic decay of highly charged metal ions.

To estimate the effect that the spin-orbit splitting of the final state would have on the ETMD $Ne^{+}(2p^{-1}\ ^2P)\cdot Xe^{2+}(5p^{-2}\ ^3P)$ spectra of the $Ne^{2+}(2p^{-2}\ ^1D)\cdot Xe$ state multiplet we computed the electron spectra for the decay of the $Ne^{2+}(2p^{-2}\ ^1D)\cdot Xe\ ^1\Sigma$ state using the model curves for the split $Xe^{2+}(5p^{-2}\ ^3P)$ multiplet. The results shown in Fig. 5.6 indicate that the overall appearance of the spectrum remains very much the same. However, the integrated intensity of the spectrum in the spin-orbit case is larger indicating that the decay into the $Ne^{+}(2p^{-1}\ ^2P)\cdot Xe^{2+}(5p^{-2}\ ^3P)$ state becomes more probable. This is due to the shifting of the ETMD thresholds so that the contribution of the $^3P_2$ channel which closes at shorter interatomic distances outweighs the contributions of the $^3P_0$ and $^3P_1$ channels which close at longer ones. We expect the effect of the spin-orbit splitting on the spectra of the $^1\Pi$ and $^1\Delta$ terms to be similar. Importantly, the spin-orbit splitting of the final state does not destroy the vibrational structure visible in the spectra.

In the case of the $Ne^{2+}(2p^{-2}\ ^1S)\cdot Xe$ state the spin-orbit splitting will have no effect

on the KER spectrum, since the latter is defined by the value of R at which the decay predominantly takes place. However, in the corresponding electron spectrum the peak at 2.2 eV will be split into three reflecting the splitting of the $Ne^+(2p^{-1}\ ^2P)\cdot Xe^{2+}(5p^{-2}\ ^3P)$ multiplet in the final state.

We would like to conclude the discussion of the results by some qualitative consideration of ETMD into the $Ne\cdot Xe^{3+}$ channel possible from the $Ne^{2+}(2p^{-2}\ ^1S)\cdot Xe$ state. Decay onto the PECs denoted by the dashed-dotted lines in Fig. 1 will lead to the dissociation of the dimer and the production of Ne and Xe^{3+} if the adiabatic nuclear dynamics takes place on the final PEC. Assuming that the decay is the strongest at the thresholds or the inner turning point of the decaying PEC we can estimate that the ETMD electrons will have energy between 0 eV and 1 eV. The KER of Ne and Xe^{3+} lies between 1.5 eV and 3 eV. Therefore, the corresponding decay should be seen from the coincidence of an electron with energy < 1 eV with the Xe^{3+} having energy between 0.2 eV and 0.4 eV. Due to the relatively low population of $Ne^{2+}(2p^{-2}\ ^1S)\cdot Xe$ state and a small number of accessible $Ne\cdot Xe^{3+}$ states the probability of such coincident events may not be large. However, experimental observation of such events will be an important demonstration of the impact that nuclear dynamics in the final states have on the ETMD process.

In general, interactions between channels belonging to ETMD and double ETMD may increase the degree of neutralization. The latter may be populated in the course of adiabatic nuclear dynamics of nuclear dynamics following ETMD. However, the branching ratio of the double ETMD products will be low if the near-degeneracy of ETMD and double ETMD channels occurs at medium or large interatomic distances as in the case of Ne·Xe. At such geometries the interaction between the channels is weak and the splitting of the adiabitc PECs small, making adiabatic nuclear dynamics improbable. If the interaction occurs at geometries, where ETMD would be most efficient, both ETMD and double ETMD channels would be directly populated due to the channel mixing. Interestingly, near degeneracy of ETMD and Auger channels were shown to cause ETMD after the core ionization of water clusters leading to the surprising neutralization of the core ionized water [96].

5.2 ETMD of Ne cations after KLL Auger decay in $Ne\cdot Kr_2$

If the environment of a cation consists of weakly interacting monomers, e.g. solvent molecules, ETMD(2) and ETMD(3) variants of the ETMD mechanism can be distinguished. In ETMD(2) it is the same neighbor which both donates an electron to the cation and receives the energy released in electron transfer becoming doubly ionized. In ETMD(3) the electron donor and the receiver of excess energy are two distinct monomers which are singly ionized at the end of the decay. The delocalization of the positive charge over the two monomers also lowers the energy of the ETMD(3) channels compared to

Parts of this chapter have been already published in
V. Stumpf, P. Kolorenč, K. Gokhberg and L. S. Cederbaum, Phys. Rev. Lett. **110**, 258302 (2013). Copyright 2013, American Physical Society.

their ETMD(2) counterparts. Therefore, ETMD(3) as a neutralization mechanism is applicable to a broader range of systems. In particular, if the charge of the cation and correspondingly its electron affinity are low, ETMD(3) may be the only available interatomic decay channel. This property of ETMD(3) was utilized to prove the occurrence of ETMD after single inner-valence ionization of argon in mixed argon-krypton clusters [27].

The timescale of ETMD is governed by the efficiency of the Coulomb interaction between the transferred electron and the rest of the electrons on the neighboring species. The average spatial separation of these electrons is substantially smaller for ETMD(2) making it superior to ETMD(3) in systems with few neighbors. In large systems, however, ETMD(3) benefits from the scaling of its decay width with the number of neighbors N which is given by $\Gamma(N) = 0.5N(N-1)\cdot\Gamma(2)$ if the neighbors are equivalent. In contrast, the scaling of ETMD(2) is linear, $\Gamma(N) = N\cdot\Gamma(1)$. Therefore, in an extended environment ETMD(3) is expected to be able to compete with ETMD(2) and to play an important role in the neutralization of cations not only with a low but also with a high charge.

To study the neutralization process driven by ETMD(3) we chose a rare gas cluster consisting of a neon atom and two krypton neighbors. Krypton atoms have a higher double ionization potential compared to xenon, prohibiting ETMD(2) for the $Ne^{2+}(2p^{-2}\ {}^1D)$ states which are strongly populated in the Auger decay. ETMD(3) remains the only electronic decay mechanism available for these states:

$$\begin{aligned} Ne\cdot Kr_2 + h\nu \rightarrow Ne^+(1s^{-1})\cdot Kr_2 &\xrightarrow{Auger} Ne^{2+}(2p^{-2}\ {}^1D)\cdot Kr_2 \\ &\xrightarrow{ETMD(3)} Ne^+(2p^{-1})\cdot(Kr^+(4p^{-1}))_2 + e_{ETMD(3)}. \end{aligned} \tag{5.2}$$

A comprehensive study of ETMD(3) including the simulation of nuclear dynamics and the computation of the observables as it was done for Ne·Xe is not feasible for the $Ne\cdot Kr_2$ cluster. The larger number of nuclear degrees of freedom greatly complicates the electronic structure computations, since multi-dimensional potential energy surfaces should be obtained. To reduce the computational demand, we considered only the nuclear coordinates which preserve the equilibrium symmetry of the cluster and performed classical simulations of the nuclear dynamics accompanying ETMD(3). As will become evident from the following this allows us to qualitatively estimate the energies of ETMD electrons and KER of the nuclei, as well as the duration of the decay.

5.2.1 Discussion

The equilibrium geometry of the $Ne\cdot Kr_2$ cluster, which belongs to the C_{2v} symmetry group, is shown in the inset to Fig. 5.9. As in the case of Ne·Xe, the transition from the neutral ground state into the $Ne^{2+}\cdot Kr_2$ by photoionization and the subsequent Auger decay is vertical. Figures 5.7 and 5.8 show cuts of the potential energy surface (PES) of the $Ne^{2+}(2p^{-2})\cdot Kr_2$ states along the coordinates corresponding to the symmetric stretch and bend starting from the equilibrium geometry of $Ne\cdot Kr_2$. The behavior along the stretch coordinate r (see Fig. 5.7) resembles that observed in Ne·Xe: the interaction between Ne^{2+} and the krypton neighbors is attractive, while the energies of the $Ne^{2+}(2p^{-2}\ {}^1D)\cdot Kr_2$ multiplet split only weakly in the considered range of r. The PEC

of the $Ne^{2+}(2p^{-2}\ ^1S)\cdot Kr_2$ state is similar to the PECs of the $Ne^{2+}(2p^{-2}\ ^1D)\cdot Kr_2$ states. Along the bend coordinate (see Fig. 5.8) the $Ne^{2+}(2p^{-2})\cdot Kr_2$ PECs are flat, displaying the weak interaction between the krypton atoms polarized by the neon dication. For all $Ne^{2+}(2p^{-2})\cdot Kr_2$ states a shortening of r due to nuclear dynamics can be expected. The movement along the bend coordinate is expected to be slower, due to both the lower gradient and the high mass of the krypton atoms.

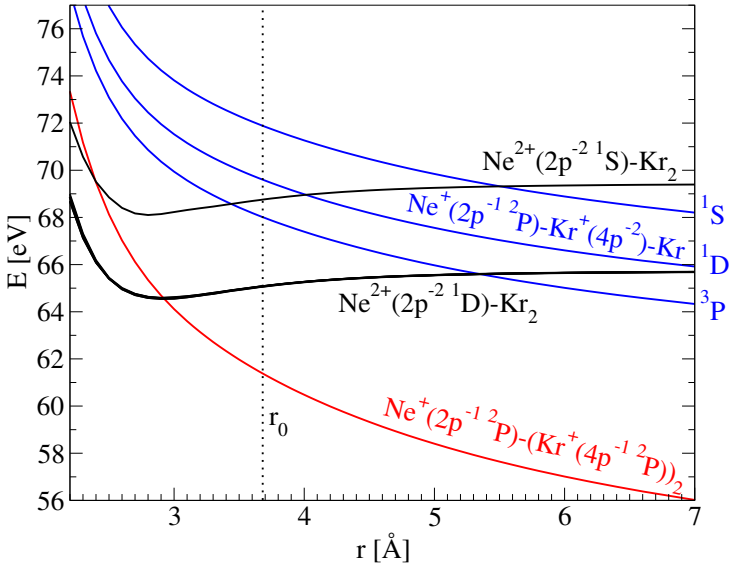

Figure 5.7: Non-relativistic diabatic PECs of the decaying $Ne^{2+}(2p^{-2})\cdot Kr_2$ states (black lines) and the PECs of the final states of ETMD along the symmetric stretch coordinate r. The Ne^+-$(Kr^+)_2$ final states of ETMD(3) (red line) are approximated using an analytic triple ionization potential (TIP): $TIP = IP(Ne) + 2IP(Kr) + 2/R_{NeKr} + 1/R_{KrKr}$. The Ne^+-$(Kr^{2+})\cdot Kr$ final states of ETMD(2) are approximated using $TIP = IP(Ne) + DIP(Kr) + 1/R_{NeKr}$. The atomic ionization potentials correspond to experimental values averaged over fine structure components [111]. The dotted vertical line denotes the equilibrium value r_0 along the symmetric stretch coordinate of the $Ne\cdot Kr_2$ ground state.

The tricationic $Ne^+(2p^{-1})\cdot(Kr^+(4p^{-1}))_2$ final states of ETMD(3) are represented by a single PES since the spin-orbit splitting present in the $Kr^+(4p^{-1}\ ^2P)$ cation is not taken into account. All atoms are positively charged in this state making it purely repulsive along the r coordinate (see Fig. 5.7). Therefore, the ETMD channel closes for the $Ne^{2+}(2p^{-2}\ ^1D)\cdot Kr_2$ states at intermediate values of r which will be accessed by nuclear dynamics in the decaying states. On the contrary, opening of the angle θ decreases the final state energy by minimizing the repulsion between the krypton cations and may open the closed ETMD channel. For the $Ne^{2+}(2p^{-2}\ ^1S)\cdot Kr_2$ state a faster neutralization via ETMD(3) is possible since this channel is open also at small values of r. In addition, ETMD(2) channels are available for this state, however, they are open only at r values close to r_0 or larger (see Fig. 5.7) and thus can be only weakly populated.

The ETMD(3) lifetimes of the $Ne^{2+}(2p^{-2})\cdot Kr_2$ states at the equilibrium geometry lie in the range of 7.7-32.3 ps. The values of the ETMD lifetimes for individual $Ne^{2+}(2p^{-2}\ ^1D)\cdot Kr_2$ states reflect the varying efficiency of the orbital overlap between Ne^{2+} and Kr arising from the different spatial orientation of the orbitals where the holes are located. The

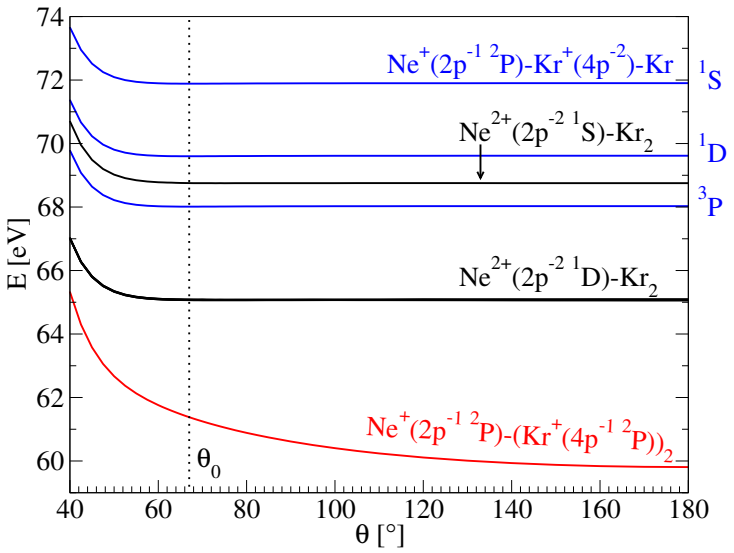

Figure 5.8: Non-relativistic diabatic PECs of the decaying $Ne^{2+}(2p^{-2})\cdot Kr_2$ states (black lines) and the PECs of the final states of ETMD along the symmetric bend coordinate θ. The Ne^{+}-$(Kr^{+})_2$ final states of ETMD(3) (red line) are approximated using an analytic triple ionization potential (TIP): $TIP = IP(Ne) + 2IP(Kr) + 2/R_{NeKr} + 1/R_{KrKr}$. The Ne^{+}-$(Kr^{2+})Kr$ final states of ETMD(2) are approximated using $TIP = IP(Ne) + DIP(Kr) + 1/R_{NeKr}$. The atomic ionization potentials correspond to experimental values averaged over fine structure components [111]. The dotted vertical line denotes the equilibrium value θ_0 along the symmetric bend coordinate of the $Ne\cdot Kr_2$ ground state.

shortest lifetime of 7.7 ps is observed for the state of b_1 symmetry, where the leading two-hole configuration is of $Ne^{2+}(2p_x^{-1}2p_z^{-1})$ character and both orbitals with holes lie in the plane of the trimer. Conversely, the state of a_1 symmetry, where the leading two-hole configuration has out-of-plane $(2p_y^{-2})$ character and, hence, the smallest overlap with the occupied orbitals of Kr, shows the longest lifetime (32.3 ps). The lifetime of the $Ne^{2+}(2p^{-2}\ {}^1S)\cdot Kr_2$ state lies at 34 ps.

A meaningful comparison with ETMD(2) lifetimes is not possible for the $Ne^{2+}(2p^{-2})\cdot Kr_2$ states since either no or only few ETMD(2) channels are open at the equilibrium geometry of $Ne\cdot Kr_2$. Compared to ETMD(2) in $Ne^{2+}\cdot Xe$, ETMD(3) in $Ne\cdot Kr_2$ is less efficient in spite of shorter internuclear distances and twice the number of electrons available for ETMD. The superiority of ETMD(2) in Ne·Xe can be attributed to the smaller average distance between the electrons of Xe participating in ETMD(2) and to the stronger polarization of the "softer" xenon atom by the neon dication, which enhances the overlap with the hole orbitals on Ne^{2+}.

As in previously discussed systems (He^{+}-Mg, $Ne^{2+}\cdot Xe$), the vibrational motion is faster than ETMD at the equilibrium geometry and accompanies the electronic decay. Due to the vibrational motion, regions of small r can be accessed enhancing the efficiency of ETMD(3). To visualize the impact of nuclear dynamics on the timescale of ETMD(3) we computed a classical trajectory corresponding to the nuclear motion in the $Ne\cdot Kr_2$ cluster after the vertical core photoionization and the Auger decay (see Fig. 5.9). The motion takes place on the PES of the $Ne^{2+}(2p^{-2})\cdot Kr_2$ b_1 state. We expect the PES of other $Ne^{2+}(2p^{-2}\ {}^1D)\cdot Kr_2$ states and the corresponding trajectories of nuclear motion to be of similar shape given the weak splitting of the PECs discussed above. For the b_1

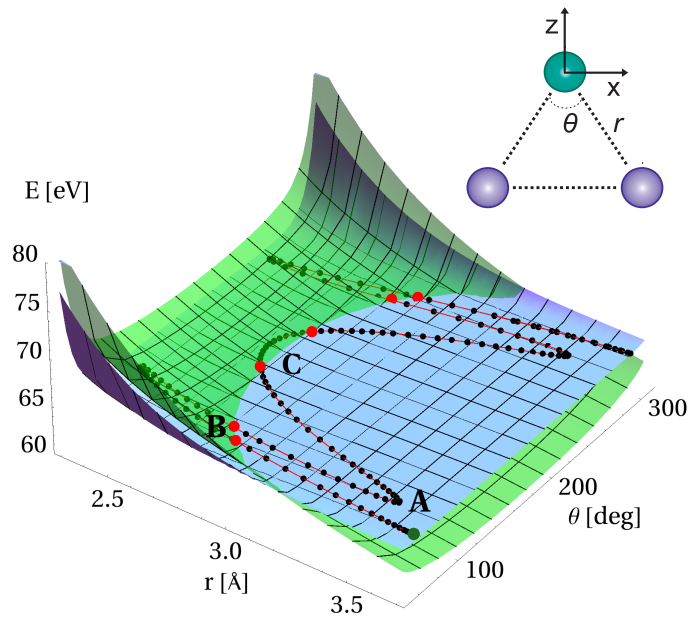

Figure 5.9: Potential energy surfaces of the decaying $Ne^{2+}(2p^{-2}\ ^1D)\cdot Kr_2$ b_1 state (blue) and of the $Ne^+(2p^{-1})$-$(Kr^+(4p^{-1}))_2$ ETMD(3) final state (green). The classical trajectory (red line) describes the movement of the nuclei initiated by a vertical transition from the neutral ground state into the b_1 dicationic state (point A). Red dots, including points B and C, denote the positions of ETMD(3) thresholds along the trajectory. Reprinted with permission from Ref. [130]. Copyright (2013) by the American Physical Society.

state we calculated the ETMD(3) rate (inverse ETMD(3) lifetime) along the classical trajectory (see Fig. 5.10).

The attractive interaction between the neon dication and the krypton neighbors leads to the reduction of the Ne·Kr interatomic distances. At the same time the the angle θ grows, indicating that the light neon dication moves towards the Kr_2 moiety. During this movement the decay rate increases steeply until the ETMD(3) channel becomes closed (see the interval between A and B). The backwards movement of Ne^{2+} opens the decay channel again at a smaller value of r and resulting in a higher maximum value of the ETMD(3) rate. This can be explained by the slow increase of the angle θ, which reduces the repulsion between the krypton cations in the final state of ETMD(3). Due to the further opening of θ the neon dication can pass between the krypton neighbors in the second oscillation (215-450 fs). Around the linear configuration of the cluster the repulsion in the final state is further lowered and the ETMD(3) channel remains open up to the Ne·Kr distances of 2.7 Å (see the threshold marked C in Fig. 5.9). The ETMD(3) lifetime at this configuration is two orders of magnitude lower compared to the equilibrium geometry (87 fs).

We computed the cumulative ETMD(3) yield for the movement of the nuclei along the classical trajectory (see Fig. 5.10). After 650 fs approximately half of the b_1 population has decayed electronically, i.e. the average ETMD(3) lifetime taking into account the nuclear dynamics lies at around 1 ps. The attractive interaction with the neighbors and the opening of the angle θ due to this attraction increased the efficiency of ETMD by almost an order of magnitude. We expect this effect of nuclear dynamics to be of general importance for cations neutralized in a polarizable host environment.

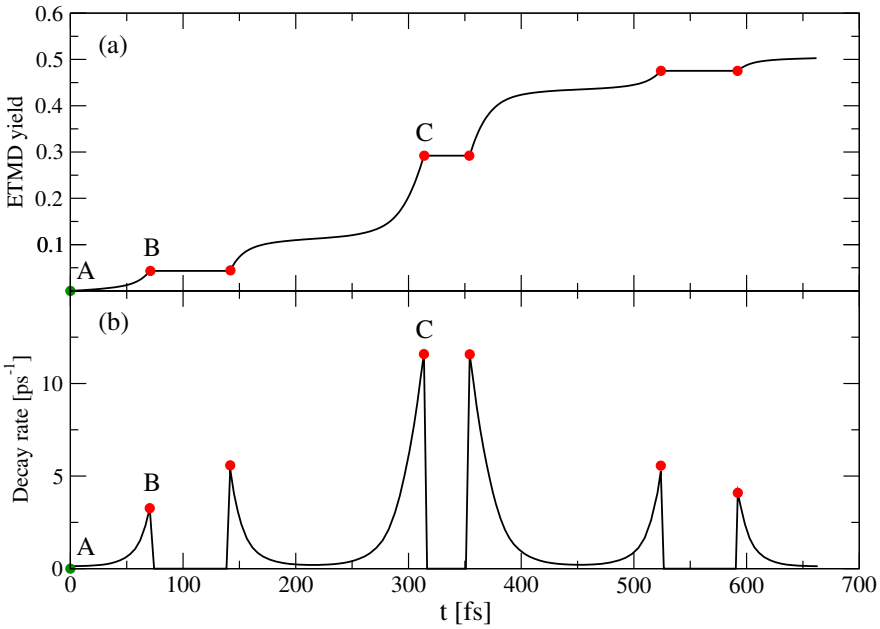

Figure 5.10: Effect of nuclear dynamics on the ETMD(3) process in Ne·Kr_2 cluster. Lower panel: the ETMD(3) rate along the trajectory given in Fig. 5.9. Note the rapid exponential increase in the rate with the decreasing Ne·Kr distance (e.g section A-B). The maximum rate achieved along the trajectory (point C) is about ninety times larger than the rate at the equilibrium geometry of the Ne·Kr_2 cluster. Upper panel: the ETMD yield accumulated along the trajectory. The majority of the decay events takes place between 210 and 450 fs at nuclear configurations close to the D_{2h} Ne·Kr_2 geometry. Reprinted with permission from Ref. [130]. Copyright (2013) by the American Physical Society.

5.3 ETMD of Ne cations after KLL Auger decay in mixed neon-krypton clusters

Triatomic rare gas clusters such as Ne·Kr_2 are seemingly ideal systems for experimental studies of the Auger-ETMD(3) cascades, since a slow electron and three positively charged ions are produced. All these particles can be recorded in coincidence experiments, as discussed for ETMD(2) in the Ne·Xe cluster, where the energy conservation should provide an unambiguous proof of the ETMD process. However, experimental production of triatomic rare gas clusters with a specific composition and sufficiently high yield is a non-trivial task. On the contrary, large mixed neon-krypton clusters are readily available and have been already utilized in experimental studies of ICD [131]. The Auger-ETMD(3) cascade is expected to occur at the neon-krypton interface of such clusters and to release considerable amounts of coincident $Ne^+/Kr^+/Kr^+$ triples as in the case of Ne·Kr_2. Unfortunately, the large size of the mixed clusters complicates the matters, since due to their size not only a simple Auger-ETMD cascade but more complicated cascades involving several interatomic steps become possible. Moreover, other processes such as electron impact ionization or RCT which are irrelevant in the triatomic cluster severely complicate the the interpretation of the experimental data and assignment of the observed events to specific interatomic decay processes. In what follows we briefly discuss possible de-excitation mechanisms in larger mixed neon-krypton clusters

after the ionization above the K-edge of neon (870 eV).

The structure of the large mixed rare gas clusters is determined by the method of their preparation. In co-expansion experiments mixed clusters with a so-called core-shell structure are usually produced [15]. They consist of a core of the heavier atoms surrounded by layers of the lighter ones. Therefore, separate regions of neon and krypton as well as an interface layer can be defined within such clusters. Due to the different local environment, the electronic relaxation pathways initiated by the interaction of the cluster with X-Rays will be different for these regions. For instance, core ionization of an atom in the Ne region would lead to ICD involving Ne neighbors, while core ionizations at the interface would also initiate ICD and ETMD with Kr atoms. Hence, by changing the size of the Kr core and the number of the Ne layers in an experiment the observable electron and ion may be modified.

We assume that the atomic Auger populations of Ne^{2+} dications will be only weakly influenced by the cluster environment [33]. If such dications are located at the Ne-Kr interface they will undergo ICD processes with Ne and Kr as well as ETMD processes with Kr neighbors, as would be the case in the smaller diatomic and triatomic clusters. The estimated electron energies for these relaxation processes in Ne·Ne, Ne·Kr and $Ne{\cdot}Kr_2$ are shown in Tab. 5.2. Due to the different degree of stabilization for the initial and final states of decay by the polarizable environment inside a larger cluster these energies will be shifted. In ICD between Ne^{2+} and Kr the charge on Ne remains the same and in a first approximation does not contribute to the shift. The shift due to the outer-valence ionization of Kr can be taken from the photoelectron spectra in Kr clusters [132] and is equal to 0.7-1.1 eV depending on the state's multiplet. Therefore, the ICD electrons are expected to be faster by about 0.7-1.1 eV in larger neon-krypton clusters compared to Ne·Kr. The energies of the ICD electrons from neon-neon pairs compared to Ne·Ne will be shifted by a considerably smaller value due the lower polarizability of neon. In ETMD(3), two Kr^+ cations appear, while positive charge on Ne charge is reduced from 2 to 1. We estimated the stabilization energy of Ne^{2+} on the Ne-Kr interface from the pair binding energies of $Ne^{2+}{\cdot}Ne$ and $Ne^{2+}{\cdot}Kr$. For the sake of simplicity we assumed fcc structure, typical for large rare gas clusters ($>10^3$ atoms), in both Ne layers and Kr core. The Ne^{2+} cation has 9 nearest Ne neighbors. It also has 3 nearest, 3 next nearest and 6 next-next nearest Kr neighbors. Using the pairwise approximation we estimated the corresponding stabilization energy of Ne^{2+} as 3.0 eV. For Ne^+ assuming 9 nearest Ne neighbors and 1 nearest, 3 next nearest and 6 next-next nearest Kr neighbors we obtained a stabilization of 0.8 eV. Together with the shift due to the production of two Kr^+ cations we expect a shift of the ETMD(3) electron energies in the range of -0.8 to 0.1 eV.

In small Ne·Ne, Ne·Kr and $Ne{\cdot}Kr_2$ clusters the relaxation of Ne^{2+} cations via ICD and ETMD(3), respectively, ultimately leads to Coulomb explosions and cluster disintegration. In larger neon-krypton clusters the situation is more complex. The excited Ne^{2+} cations decay via ICD which populates doubly outer-valence ionized states (see decay steps 4-6 in Tab. 5.2). If neutral krypton neighbors are present, these states may continue decaying by ETMD(3) (decay steps 1-2). This is also true for the $Ne^{2+}(2p^{-2}\ {}^3P)$ states (decay step 3) which are not populated directly in the Auger decay but by ICD of the $Ne^{2+}(2s^{-1}2p^{-1}\ {}^3P)$. Thus, *cascades* of interatomic decay processes are possible after the Auger decay in larger clusters.

Table 5.2: Kinetic energies of electrons emitted in the interatomic relaxation of neon dications in Ne·Ne, Ne·Kr and Ne·Kr_2 clusters. ETMD(3) electron energies were calculated as described in chapter 3.4.2. ICD electron energies for the Ne^{2+}·Kr were calculated at the equilibrium geometry of the Ne·Kr cluster using analytic double ionization potential (DIP): $DIP = IP(Ne) + IP(Kr) + 1/R_{NeKr}$ and experimental atomic ionization energies [111]. The ICD electron energies for Ne^{2+}·Ne were adapted from Ref. [33].

Nr.	Decay step	E_{kin} [eV]
1	$Ne^{2+}(2p^{-2}\ ^1D) \cdot Kr_2 \xrightarrow{ETMD(3)} Ne^+(2p^{-1}) \cdot Kr^+(4p^{-1}))_2 + e_{ETMD(3)}$	0-4.5
2	$Ne^{2+}(2p^{-2}\ ^1S) \cdot Kr_2 \xrightarrow{ETMD(3)} Ne^+(2p^{-1}) \cdot Kr^+(4p^{-1}))_2 + e_{ETMD(3)}$	1-8.5
3	$Ne^{2+}(2s^{-1}2p^{-1}\ ^3P) \cdot Kr \xrightarrow{ICD} Ne^{2+}(2p^{-2}\ ^3P) \cdot Kr^+(4p^{-1}) + e_{ICD}$	0-3.5
4	$Ne^{2+}(2s^{-1}2p^{-1}\ ^1P) \cdot Kr \xrightarrow{ICD} Ne^{2+}(2p^{-2}\ ^1D) \cdot Kr^+(4p^{-1}) + e_{ICD}$	8-11
5	$Ne^{2+}(2s^{-1}2p^{-1}\ ^1P) \cdot Ne \xrightarrow{ICD} Ne^{2+}(2p^{-2}\ ^1D) \cdot Ne^+(2p^{-1}) + e_{ICD}$	0-3
6	$Ne^{2+}(2s^{-1}2p^{-1}\ ^1P) \cdot Kr \xrightarrow{ICD} Ne^{2+}(2p^{-2}\ ^1S) \cdot Kr^+(4p^{-1}) + e_{ICD}$	5-7.5
7	$Ne^{2+}(2s^{-2}\ ^1S) \cdot Kr \xrightarrow{ICD} Ne^{2+}(2s^{-1}2p^{-1}\ ^1P) \cdot Kr^+(4p^{-1}) + e_{ICD}$	0-2

The prerequisite for the appearance of such cascades is the ability of the following interatomic decay steps to compete with repulsive nuclear dynamics initiated by the previous ones. Alternatively, the cascades might be realized if the Coulomb explosion after the initial interatomic decay step leads to the fission of the cluster which produces Ne^{2+} cations surrounded by several neutral krypton neighbors. Taking into account the timescale of ETMD (we estimate the lifetimes to be of the order of hundreds of fs to few ps in large mixed neon-krypton clusters) the impact of such cascades on the electron and KER spectra is expected to be limited. A presumably more efficient ICD-ICD cascade is possible for $Ne^{2+}(2s^{-2}\ ^1S)$ cations (decay step 7). If ICD-ETMD or ICD-ICD-ETMD cascades occur, both ICD and ETMD electrons can be observed in coincidence with $Ne^+/Kr^+/Kr^+$ triples of nuclei, yielding electron spectra different from those in Ne·Kr_2. The positive charge created in the first cascade step may lead to the deceleration of the electrons in a subsequent step and ultimately to the closing of the decay channels [133]. Hence, the energies of electrons produced by the second or later steps of the interatomic cascades might be lower than the energies shown in Tab. 5.2 corrected for the polarizable cluster environment.

Additional complication in the experimental studies of electronic decay following X-Ray absorption in neon-krypton clusters is the high photoabsorption cross section of krypton at photon energies above the K-edge of neon [123]. In this energy range mostly $3s$, $3p$ and $3d$ electrons are removed, which gives rise to Auger, double Auger and Coster-Kronig decays as well as complicated cascades of these decays [134–136]. Moreover, the excited states produced by these decay mechanisms, may also undergo ICD in neon-krypton clusters. In addition to ICD, secondary processes which follow the electronic decay, such as radiative charge transfer, could also produce $Ne^+/Kr^+/Kr^+$ triples after the photoionization of krypton. Together with the slow electrons emitted in the decay of krypton, these ion signals would appear in the coincidence spectra recorded for the analysis of ETMD(3) events of Ne^{2+}.

Indeed, such events are very prominent as recent coincidence experiments demonstrate

[137]. Therefore, in order to determine the number of the ETMD(3) events, a subtraction of the signal produced by the photoionization of krypton had to be performed. The resulting electron spectrum recorded in coincidence with the $Ne^+/Kr^+/Kr^+$ signal is shown in Fig. 5.11. The electron signal in the range of 0-10 eV gives the first evidence for the occurrence of the Auger-ETMD(3) cascade after the core ionization of neon in mixed neon-krypton clusters. Signals at energies > 10 eV can be interpreted as a signature of ICD involved in the ICD-ETMD cascades.

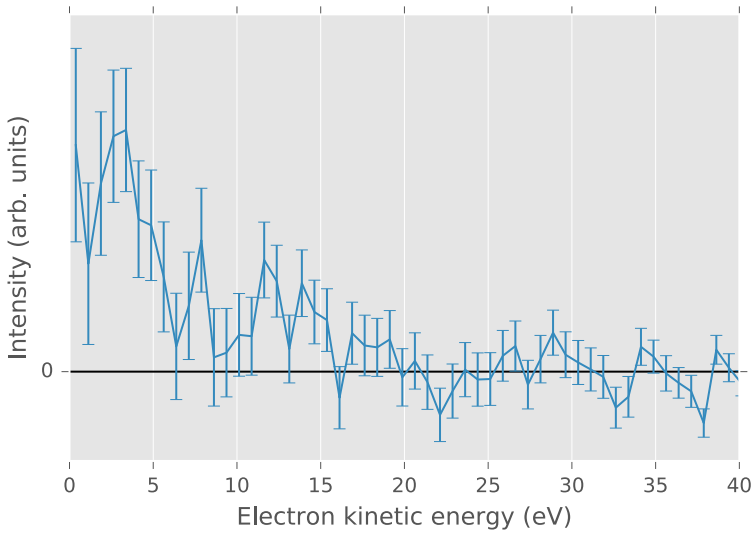

Figure 5.11: Electron spectrum recorded at 878 eV photon energy in coincidence with $Ne^+/Kr^+/Kr^+$ nuclei in mixed neon-krypton clusters [137]. The photoelectron signal of neon at (≈ 8 eV) and signal stemming from the photoionization of krypton were subtracted.

5.4 Conclusions

In this chapter we investigated the partial, ETMD-driven neutralization of dications produced by the Auger decay of neon. We demonstrated that neutralization both via ETMD(2) and ETMD(3) proceeds on a picosecond timescale in small rare gas clusters. The nuclear dynamics triggered by the creation of the positive charge on neon increase the average rate of the neutralization. This phenomenon is expected to be of general importance for the neutralization of cations embedded in a polarizable environment. Experimental evidence for the neutralization of neon dications driven by ETMD(3) was given by coincidence measurements of electrons and $Ne^+/Kr^+/Kr^+$ nuclei in mixed neon-krypton clusters after X-Ray absorption. The corresponding electron spectra furthermore indicate occurrence of cascades of interatomic decay steps following the Auger decay of neon.

6 X-Ray induced electronic cascades in microsolvated metal ions

Metals play an essential role in the biochemistry of living organisms. They mostly appear as cations bound either by electrostatic or coordinative interactions to their environment. In the former case the metal ions (Na, K, Mg, Ca) bear such important functions as signaling and stabilizing or controlling the structure of the multiply negatively charged biomolecules such as DNA, proteins, ATP etc. In the metalloenzymes and metal cofactors the strongly bound metals (Fe, Zn, Cu etc.) directly participate in the catalytic processes, acting as Lewis acids and facilitating electrons transfer, group transfer and further important types of reaction steps [44].

The positive charge, already present on the metal atoms in the electronic ground state can be further increased if the metal undergoes Auger decay. The electron affinities associated with these highly charged ions indicate that they will most probably undergo ETMD-driven neutralization processes after X-Ray absorption. Recalling that the X-Rays are a cause of radiation damage in biological systems, the question arises whether X-Ray absorption at the metal sites and the subsequent ETMD may play a role in producing damage to biomolecules. We have seen in the last chapter that the neutralization process mediated by ETMD involves ionization or double ionization of the cations' neighbors and emission of slow electrons. Considering a particular biomolecule, such as DNA, radiation damage can be classified either as direct, i.e. targeting the biomolecule itself and indirect, i.e. targeting neighboring molecules which harm the biomolecule in a subsequent step. Within this classification scheme the release of slow electrons is an indirect damage since they are known to induce breaking of chemical bonds in biomolecules [38]. The ionization of the neighbors can be classified as direct damage if the metal atom is attached to a biomolecule and causes its ionization in the ETMD process. On the other hand, a solvated metal ion in the proximity of a biomolecule could introduce indirect damage by ionizing the solvent molecules and thereby releasing reactive radicals which can attack the biomolecule in the subsequent chemical reactions [39].

Experimental insight into the radiation damage in biomolecules containing metals comes from the X-Ray crystallography. The radiation damage which accumulates in the course of the measurements causes a blurring of the diffraction images [45]. The damage is often non-random,the metal site being one of the weak spots [47, 48] and is modified already at a relatively low radiation dose. One of the most frequent indications of this damage is the reduction of the metal and elongation of the metal-ligand distances [47,49]. It is usually explained by the ionization elsewhere in the protein and a subsequent

Parts of this chapter have been already published in
V. Stumpf, K. Gokhberg and L. S. Cederbaum, Nat. Chem. **8**, 237 (2016). Copyright 2016, Nature Publishing Group.

electron attachment to the metal. Interestingly, X-Ray absorption spectroscopy of metal complexes shows that the metal may also become oxidized or remain in the original charge state depending on the nature of the ligand [138, 139]. So far neither a unified picture of radiation damage nor detailed molecular mechanisms of how it is incurred have been established with certainty. In the following we contribute to the ongoing discussion and present an electronic decay cascade which can be particularly effective at damaging the metal containing sites in biomolecules.

We chose a microsolvated $Mg^{2+}\cdot(H_2O)_6$ cluster to study the processes taking place after the X-Ray absorption by a metal embedded in an extended environment. Microsolvated clusters consist of ions surrounded by a finite number of solvent molecules and play an important role in such research fields as surface, atmospheric and biophysical chemistry (see [140] and references therein). On the other hand, small microsolvated clusters are utilized to study interactions between the ions and solvents molecules [141] while studying the larger ones allows to trace the transition to the liquid state [142]. Experimentally, microsolvated clusters can be produced by a pick-up procedure, where neutral atoms are accommodated in a solvent microcluster and subsequently ionized by electron impact [141]. Alternatively, such clusters are generated by electrospray ionization of the ionic solutions [143].

First computational studies of ICD and ETMD in microsolvated clusters were conducted by Müller et al. [93]. The authors predicted appearance of ETMD(2) and ETMD(3) processes after the photoionization of microhydrated lithium cations, which was recently verified by electron spectroscopy of LiCl aqueous solutions [144]. In a further experimental study Pokapanich et al. determined the ICD lifetimes of Ca^{2+} and K^+ in aqueous solutions after the $2p$ photoionization by comparing the corresponding electron signals to the signals of the competing Auger process [95]. The observation of the ICD signal implies that this process is sufficiently fast for metal ions in aqueous solutions to escape quenching by the Auger process which occurs on a timescale of few femtoseconds. The ordering of the experimental ICD lifetimes of Ca^{2+} and K^+ and their magnitude has been reproduced by *ab initio* computations of microsolvated clusters consisting of the metal ions and the first coordination shell. The interatomic decay widths drop sharply with the growing interatomic distance and it is the first coordination shell which contributes at most to the decay of the metal cation. This feature explains the success of the microsolvated cluster models in the description of the interatomic decay in solutions. The $Mg^{2+}\cdot(H_2O)_6$ cluster closely resembles ($R_{MgO} = 2.08$ Å) the most probable structure of the metal's first coordination shell in diluted aqueous solutions ($R_{MgO} = 2.00 - 2.15$ Å) [101]. Hence the properties of the decay processes in $Mg^{2+}\cdot(H_2O)_6$ such as total or partial decay widths are expected to reproduce those in an aqueous solution. More generally, the results should also provide a qualitative picture for other metals in a non-covalent environment as is common for biological systems.

The absorption of an X-Ray photon by the Mg^{2+} cation predominantly removes the $1s$ electrons of magnesium. After the core ionization the magnesium dication undergoes mainly a single-step Auger decay increasing the charge of the metal to four:

$$Mg^{2+}\cdot(H_2O)_6 \xrightarrow{h\nu} Mg^{3+}(1s^{-1})\cdot(H_2O)_6 \xrightarrow{Auger} Mg^{4+}\cdot(H_2O)_6 \tag{6.1}$$

As in the case of the isoelectronic neon atom, the interatomic decay of Mg^{4+} comprises not only the neutralization steps via ETMD but also the energy transfer steps from

the electronically excited metal cation to the environment via ICD. These processes are visualized in the Fig. 6.1. Obviously, the charge of the Mg^{3+} cation which was partially neutralized via an ETMD process is still very high ($EA \approx 80$ eV for the isolated cation [111]). This large electronic affinity is sufficient for an additional neutralization step. Therefore, it is not a single interatomic decay step which follows the Auger decay of Mg^{3+} but rather a *cascade* of interatomic decay steps.

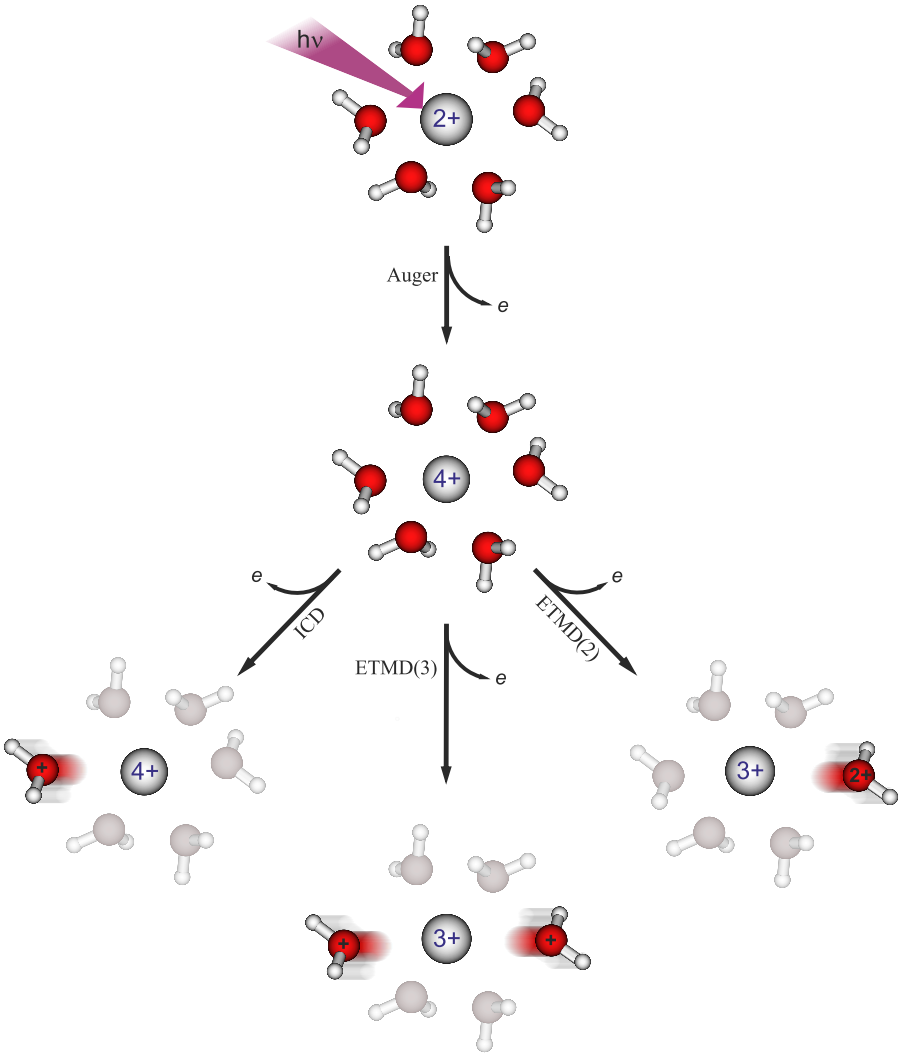

Figure 6.1: Electronic relaxation processes possible in the microsolvated Mg^{4+} cation created by core ionization of Mg^{2+} (photoelectron not shown) and subsequent Auger decay. Excited states of Mg^{4+} transfer the excess energy to the environment singly ionizing a water neighbor (ICD process). Energetically low lying states of Mg^{4+} accept an electron from a water neighbor, transferring the excess energy either to the same water molecule (ETMD(2) process) or to a different one (ETMD(3) process). In small microsolvated clusters the described modes of interatomic electronic relaxation are followed by Coulomb explosion. In larger clusters the water cations are likely to decompose preferentially by proton transfer to the next solvation shell either directly or in the collision of the flying away cation with that shell [36, 145, 146].

We determined the sequence of the electronic decay processes involved in the cascade as well as the duration of the individual steps. We furthermore estimated the contribution of this cascade to the X-Ray induced radiation damage by calculating the number of released electrons and radicals. The nuclear dynamics accompanying the electronic decay cascade were not treated explicitly given the large number of nuclear degrees of freedom. Only a qualitative discussion of the impact which the nuclear dynamics have on the timescale of the electronic decay and the yields of the reactive species is included.

6.1 Interatomic decay of the Mg^{4+} cations produced by Auger decay

We found in an *ab initio* calculation that the binding energy of the magnesium 1s electron in $Mg^{2+}\cdot(H_2O)_6$ is 1317 eV. Removing this electron by an X-ray photon creates a highly energetic, electronically unstable trication. In the following we discuss the fate of this unstable trication. We do not consider double Auger decay leading to $Mg^{5+}\cdot(H_2O)_6$ states, since our computational methods do not allow to obtain the normal-to-double Auger branching ratio. We expect, however, in analogy to the isoelectronic neon atom, a low population of the double Auger products. The predominant decay mechanism for the magnesium trication is the normal Auger decay, leading to the emission of a fast electron and population of $Mg^{4+}\cdot(H_2O)_6$ states. The states of Mg^{4+} mostly populated in the Auger decay are $Mg^{4+}(2p^{-2}\ {}^1D,{}^1S)$ (63%), $Mg^{4+}(2s^{-1}2p^{-1}\ {}^1P)$ (21%), $Mg^{4+}(2s^{-1}2p^{-1}\ {}^3P)$ (9%), and $Mg^{4+}(2s^{-2}\ {}^1S)$ (7%). However, while the Auger populations are comparable to those of the neon atom (see chapter 5.1), the Auger lifetime is considerably reduced from 2.7 to 1.9 fs.

All of the Mg^{4+} electronic states are unstable with respect to interatomic electronic decay in the presence of water molecules. In the microsolvated cluster both the weakly populated $Mg^{4+}(2p^{-2}\ {}^3P)$ ground state and the most populated $Mg^{4+}(2p^{-2}\ {}^1D,{}^1S)$ states, which have about 4-9 eV excess energy relative to the ground state, cannot decay by ICD. However, they efficiently decay by both ETMD(2) and ETMD(3) pathways. The computed ETMD lifetimes are about 16 fs (see Tab. 6.1), which are much shorter than the picosecond lifetimes found we obtained for the Ne·Xe and Ne·Kr_2 clusters. They are comparable to the 20 fs ETMD lifetime of the tetrahydrated Li^{2+} cations calculated by Müller et al. [93]. The high number of water neighbors and the shorter ion-neighbor distances, which facilitate the electron transfer, strongly enhance both ETMD(2) and ETMD(3) processes. The ETMD(2) to ETMD(3) branching ratio is 1.0/1.6, therefore, both H_2O^+ and H_2O^{2+} are efficiently produced in the ionization of the medium. The final products are either $Mg^{3+}(2p^{-1}\ {}^2P)\cdot(H_2O)_5H_2O^{2+}$ or $Mg^{3+}(2p^{-1}\ {}^2P)\cdot(H_2O)_4(H_2O^+)_2$: the positive charge on Mg is partially neutralized as the result of electron transfer from water (see Fig. 6.1). It is remarkable that ETMD(3) is the more efficient neutralization pathway, in contrast to ETMD(2) which is dominant in small rare gas clusters (see previous chapter). ETMD(3) strongly benefits from the $N\cdot(N-1)$ scaling of the decay width with the number of equivalent neighbors N and the reduced water-water distances in microsolvated clusters. The ETMD electrons have energies between 11 and 26 eV for ETMD(2) and between 23 and 40 eV for ETMD(3). The greater delocalization of the

Table 6.1: Lifetimes and branching ratios of competing decay processes for cationic states produced by the Auger decay of the core ionized $Mg^{3+}(1s^{-1}\ ^2S)\cdot(H_2O)_6$ cluster. Minor channels contributing less than 10 percent to the product population are neglected.

Decaying state	Lifetime [fs]	ETMD(3)	ETMD(2)	ICD
Mg^{4+} $(2p^{-2}\ ^1D)$	15.6	0.65	0.35	-
Mg^{4+} $(2p^{-2}\ ^1S)$	18.2	0.57	0.43	-
Mg^{4+} $(2s^{-1}2p^{-}\ ^3P)$	17.5	0.51	0.49	-
Mg^{4+} $(2s^{-1}2p^{-1}\ ^1P)$	0.7	-	-	1.0
Mg^{4+} $(2s^{-2}\ ^1S)$	0.9	-	-	1.0

positive charge in the final state of ETMD(3) results in faster emitted electrons.

The excited $Mg^{4+}(2s^{-1}2p^{-1}\ ^3P)$ cations also undergo ETMD(2) and ETMD(3) since the corresponding excess energy is not sufficient for ICD, the decay lifetime is 17 fs. Both the $2p$ and the $2s$ orbitals may accept the electron from a water neighbor in the ETMD process. The water electron is preferably transferred to the $2p$ orbital of Mg due its larger spatial overlap with the valence orbitals of the water neighbors. The ratio of the $Mg^{3+}(2p^{-1}\ ^2P)$ and $Mg^{3+}(2s^{-1}\ ^2S)$ cations produced by ETMD is 1.0:1.6. The magnitudes of ETMD(2) and ETMD(3) are comparable, however their branching ratio for the electron transfer into the $2s$ is higher (1.1/1.0) than the ratio for the transfer into the $2p$ orbital (1.0/1.5). In other words, the electron transfer into the compact $2s$ orbital couples more efficiently to the emission of another electron from the same water neighbor than from a more distant one, enhancing ETMD(2). For the electron transfer into the $2p$ orbital ETMD(3) is the leading relaxation pathway as observed for the $Mg^{4+}(2p^{-2}\ ^1D,^1S)$ states. The energies of the ETMD(2) and ETMD(3) electrons lie in the ranges of 3-53 and 17-66 eV, respectively. The broadness of these ranges reflects the difference in energies between the $Mg^{3+}(2p^{-1}\ ^2P)$ and $Mg^{3+}(2s^{-1}\ ^2S)$ cations in the final states of ETMD. Unlike the states considered above, microsolvated $Mg^{4+}(2s^{-1}2p^{-1}\ ^1P)$ possesses enough excess energy for the ionization of the water molecules and, therefore, can decay by ICD. Its computed ICD lifetime is extremely short, 0.7 fs, showing that this interatomic decay occurs even faster than the already very fast local Auger decay on the metal (1.9 fs). We mention that the experimentally determined ICD lifetime of $Mg^{3+}(2s^{-1}\ ^2S)$ in liquid water is 1.5 fs [14], indicating that such extremely fast interatomic decay in hydrated metal ions is the rule rather than exception, due to the short metal-water distances and a large number of open ICD channels. In this state ICD will also dominate ETMD by about an order of magnitude due to the higher efficiency of energy transfer. The energies of the ICD electrons lie below 7 eV.

The ICD of the high-lying $Mg^{4+}(2s^{-2}\ ^1S)$ into the $Mg^{4+}(2s^{-1}2p^{-1}\ ^1P)$ state is energetically forbidden. A possible decay pathway for the $Mg^{4+}(2s^{-2}\ ^1S)$ cation is the transition into the $Mg^{4+}(2s^{-1}2p^{-1}\ ^3P)$ state, which involves an electron transfer from a water neighbor due to the change in the multiplicity from singlet to triplet. This mechanism is denoted as exchange ICD [147] and is expected to be inferior to the ordinary, energy transfer driven ICD. Its lifetime should be comparable to the ETMD lifetimes of other Mg^{4+} states. Surprisingly, the calculated decay lifetime of the $Mg^{4+}(2s^{-2}\ ^1S)$ state

lies at approximately 1 fs, i.e. it is comparable to the lifetime of the $Mg^{4+}(2s^{-1}2p^{-1}\ ^1P)$ decaying by the ordinary ICD. The $Mg^{4+}(2s^{-2}\ ^1S)$ cation, which has a very high excess energy, can undergo a so-called double ICD process [148]. In the course of this three-electron decay process two electrons fill the $2s$ vacancies and the excess energy is utilized to remove a third electron from a neighbor. No rates of double ICD in other systems with double-holes on a single atom have been reported so far. However, it has been demonstrated that an intramolecular autoionization driven by two electron transition into a double-hole inner-valence state can be of a few fs duration [149]. To clarify which mechanism is responsible for the ultrafast decay of the double inner-valence hole we computed the corresponding partial widths and showed that the contribution of the double ICD is only of minor importance, the lifetime is determined by a two-electron ICD process producing $Mg^{4+}(2s^{-1}2p^{-1}\ ^3P)$. The explanation might be that at short ion-water distances the coupling in the final state between the outer-valence hole on H_2O^+ with $2s$ and $2p$ holes on Mg^{4+} is so strong that the whole notion of electron transfer driven exchange ICD process becomes untenable. Indeed, the $Mg^{4+}(2s^{-1}2p^{-1}\ ^1P)\cdot H_2O^+$ configuration becomes admixed to the leading $Mg^{4+}(2s^{-1}2p^{-1}\ ^3P)\cdot H_2O^+$ in the final state increasing the decay rate.

6.2 Cascades of interatomic decay after core ionization of Mg^{2+}

The individual interatomic decay processes considered above constitute a ramified decay cascade which follows the Auger process in $Mg^{3+}(1s^{-1}\ ^2S)\cdot(H_2O)_6$. We construct this cascade by following the fate of different states populated in the Auger decay.

We first consider the $Mg^{4+}(2p^{-2})\cdot(H_2O)_5H_2O^+$ states produced by the ICD of $Mg^{4+}(2s^{-1}2p^{-1}\ ^1P)$. These are the same states of Mg^{4+} we discussed above but now with H_2O^+ ion in its vicinity. Can they continue decaying by ETMD? The ETMD channels in the $Mg^{4+}(2p^{-2})\cdot(H_2O)_5H_2O^+$ cluster have a complicated electronic structure and require application of the computationally highly demanding MRCI method. Therefore, an explicit computation of states involved into ETMD of $Mg^{4+}(2p^{-2})\cdot(H_2O)_5H_2O^+$ was not possible. We performed model calculations instead. Since the water neighbor ionized via ICD has a significantly higher single and double ionization potentials compared to a neutral one [150,151], most of the ETMD channels involving this neighbor will be closed. Hence, we replaced the ionized water neighbor by a positive point charge. A positive charge destabilizes the final states of ETMD relatively to the initial, which may lead to the closing of decay channels. This effect was found to be responsible for the dependence of ICD lifetimes on the pH values in aqueous solutions [133]. According to our model calculations all the ETMD(2) and ETMD(3) channels available in the $Mg^{4+}(2p^{-2})\cdot(H_2O)_5$ system remain open for $Mg^{4+}(2p^{-2})\cdot(H_2O)_5H_2O^+$. The ETMD lifetime grows from 16.0 to 21.8 fs since only five neutral water neighbors are now available for the electronic decay. In the same way the lifetime of the $Mg^{4+}(2s^{-1}2p^{-1}\ ^3P)(H_2O^+)(H_2O)_5$ states, which are populated by the ICD of $Mg^{4+}(2s^{-2}\ ^1S)$, grows from 17.5 to 23.2 fs. The single step ETMD process and the ICD-ETMD cascade following the Auger decay lead to the formation of Mg^{3+} cations. Only a small portion of these cations

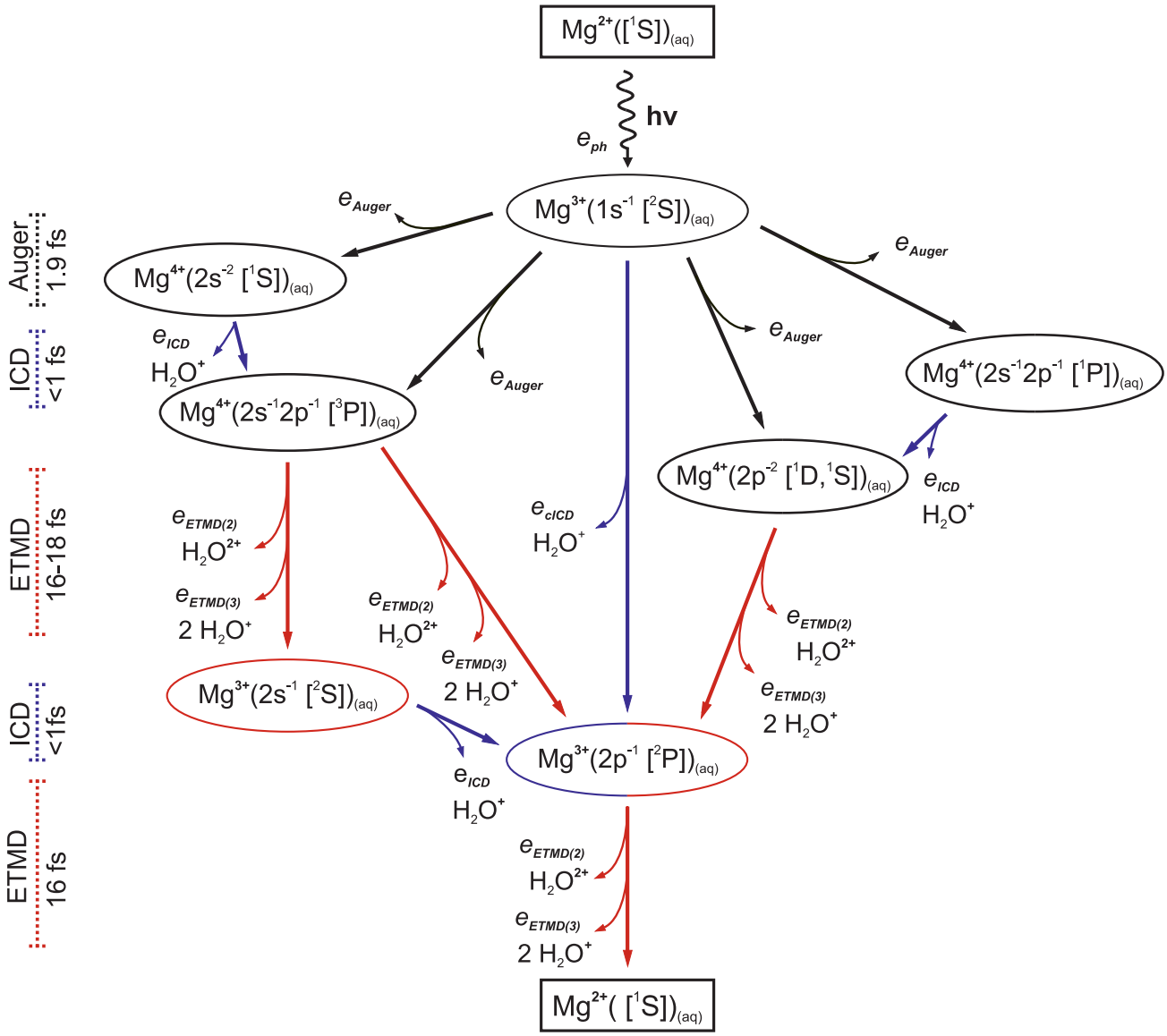

Figure 6.2: Schematic description of the electronic decay processes taking place after the core ionization of the hydrated Mg^{2+} cation. First, the intra-atomic Auger decay (black arrows) creates highly charged Mg^{4+} cations. Then, the energetic ions lose their excess energy by ICD. The Mg^{4+} ions with little excess energy undergo ETMD and become reduced. Computed electronic decay lifetimes for $Mg^{q+}(H_2O)_6$ clusters are shown on the left. The cascade continues until all Mg^{4+} and Mg^{3+} ions revert to the original Mg^{2+} state in a sequence of ultrafast, interatomic ICD (blue) and ETMD (red) steps. Estimated time for the complete cycle is 220 fs. Several reactive products such as electrons, water cations and dications are released mainly from the first coordination shell of Mg^{2+} as indicated by the side arrows.

is in the excited $Mg^{3+}(2s^{-1}\ ^2S)$ state since it can be produced solely by the ETMD of $Mg^{4+}(2s^{-1}2p^{-1}\ ^3P)$. The majority of the magnesium trications are in the electronic ground state $Mg^{3+}(2p^{-1}\ ^2P)$ (see Fig. 6.2). We wish to remark at this point that the $Mg^{3+}(2p^{-1}\ ^2P)$ species can also be obtained directly from the initial core ionized Mg ion in the presence of water ligands. Thus, a $2p$ electron of Mg may fill the $1s$ vacancy and transfer its energy not to another $2p$ electron, which would result in the Auger process on the metal, but to a valence electron on water ionizing it in a core ICD-like process [95,96,152]. This decay leads to population of $Mg^{3+}(H_2O^+)(H_2O)_5$ states. Since the positive charge in the latter is more delocalized than in the final states of the Auger decay, the electrons emitted in the core ICD-like process have larger energies (1205-1225 eV) compared to the Auger electrons (1111-1157 eV). What process will be more important? The Auger lifetime of the core ionized state was found to be 1.9 fs, while its ICD lifetime was 57 fs. Therefore, the Auger decay takes place in 97 % of $Mg^{4+}(H_2O)_6$ systems and core ICD-like only in 3%. This branching ratio, however, can be tilted much more in favor of the interatomic process for other metal ions. Thus in the case of Ca^{2+} the core ICD-like probability was found experimentally to be 10% [153].

The $Mg^{3+}(2p^{-1}\ ^2P)$ state has a high electron affinity and therefore lies in the electronic continuum of the ETMD final states if neutral water neighbors are present. To visualize the impact of the metal's charge on the ETMD lifetimes and observables, we compare these quantities for the $Mg^{3+}(2p^{-1}\ ^2P)\cdot(H_2O)_6$ and $Mg^{4+}(2p^{-2}\ ^1D,^1S)\cdot(H_2O)_6$ clusters. In the $Mg^{3+}(2p^{-1}\ ^2P)\cdot(H_2O)_6$ cluster both ETMD(2) and ETMD(3) channels are open, the corresponding lifetime is 15.5 fs. Thus, the decreased positive charge does not modify the ETMD lifetime significantly. This result is not obvious since the polarization of the water ligands is weaker in the case of Mg^{3+} compared to Mg^{4+} cations. The polarization of the ligands is expected to enhance ETMD due to the increased overlap of the ligands' electrons with the hole orbitals on magnesium. A related discussion on the charge dependence of ICD widths of microsolvated metal ions (see chapter 7) shows, however, that the ligand polarization is not the only charge dependent parameter determining the efficiency of interatomic decay. The ratio of the ETMD(2) to ETMD(3) populations does not deviate significantly from the results for the $Mg^{4+}(2p^{-2}\ ^1D,^1S)$ as well, being 1.0/1.2. In contrast, the energies of the ETMD electrons in $Mg^{3+}(2p^{-1}\ ^2P)\cdot(H_2O^{2+})_6$ are markedly reduced and lie at 0-6 and 5-19 eV, respectively. The reduction of the electron energies is due to the significantly lower electron affinity of $Mg^{3+}(2p^{-1}\ ^2P)$ (atomic value ≈ 80 eV) compared to $Mg^{4+}(2p^{-2}\ ^1D,^1S)$ ($\approx 109-119$ eV) which can not be compensated by the lower Coulombic repulsion in the final states of ETMD.

Interestingly, also the excited $Mg^{3+}(2s^{-1}\ ^2S)\cdot(H_2O)_6$ species (see Fig. 6.2) resembles the decay characteristics of its higher charged $Mg^{4+}(2s^{-1}2p^{-1}\ ^1P)\cdot(H_2O)_6$ analogue. The corresponding ICD lifetime is ultrashort with only 0.8 fs. A detailed discussion of the factors which cause the high efficiency of ICD in microsolvated clusters of metal ions is presented in chapter 7. The energies of the ICD electrons lie in the range of 4-10 eV, i.e. few eV higher than for the $Mg^{4+}(2s^{-1}2p^{-1}\ ^1P)$ cation. The difference in the excess energies of $Mg^{3+}(2s^{-1}\ ^2S)$ and $Mg^{4+}(2s^{-1}2p^{-1}\ ^1P)$ is of the same magnitude as the difference in the Coulombic repulsion in the final states, leading to an overall small shift in the ICD electron energies.

The Mg^{3+} species produced in the course of the decay cascade after the core ionization of magnesium is not surrounded by six neutral water neighbors. Some of these neighbors

are ionized or doubly ionized depending on the pathway of the Mg^{3+} production, which includes ICD-like, ETMD processes or the longer ICD-ETMD and ICD-ETMD-ICD cascades. The presence of the water cations has an impact on the lifetimes of Mg^{3+} species as discussed above. Again, by replacing previously ionized water ligands with point charges we estimated the Mg^{3+} lifetimes for each individual pathway of production. The ETMD lifetimes of the $Mg^{3+}(2p^{-1}\ ^2P)$ cations lie in the range of 43-400 fs eV. The longest lifetimes belong to cations produced by the ICD-ETMD-ICD cascade with several positively charged neighbors in the vicinity of magnesium. The shortest lifetimes are found for cations obtained by single step core ICD-like or ETMD(2) processes. The ICD lifetimes are located in the interval between 8 and 152 fs. In this case not only the lower number of the ionizable neighbors but additionally the closing of the high-lying ICD channels considerably increase the lifetime. Among the closed ICD channels are those with holes in the a_1 orbitals of water which are directed towards the metal ion. Whenever open, these ICD channels are the strongest due to the small average distance between the electrons on magnesium and those occupying the a_1 orbital of water.

We see that even in the presence of several ionized neighbors the interatomic decay steps discussed above can be glued into a continuous decay cascade (see Fig. 6.2). Taking into account the decreasing number of neutral water neighbors available for interatomic decay at each consecutive step of the cascade we find that 90 percent of the core ionized states would de-excite to the final state within only 220 fs (see Fig. 6.3). Thus, although the majority of the energy stored in the core ionized $Mg^{3+}(1s^{-1}\ ^2S)$ cation is taken away by the fast Auger electron, the remaining electronic energy of $160 - 240$ eV is sufficient to drive a long decay cascade on a femtosecond timescale. If for a specific electronic state of the metal both ICD and ETMD channels are available, ICD will be predominant. It will lead to the electronic relaxation of the metal ion without changing its charge. An ETMD step will follow reducing the charge by one. This is illustrated by the decay of $Mg^{4+}(2s^{-1}2p^{-1}\ ^1P)$ first by ICD to $Mg^{4+}(2p^{-2})$ states and further by ETMD to $Mg^{3+}(2p^{-1}\ ^2P)$. Even if the ion does not have excess energy and ICD is not possible there can still be available ETMD channels. Therefore, the cascade of the interatomic processes goes on and the ion is being reduced until no interatomic electronic decay is allowed. For our system it leads to the surprising result that Mg ends up in the same electronic state it was in initially.

All the individual electronic decay steps we discussed for the microsolvated $Mg^{2+}(H_2O)_6$ cluster will occur also in solution. The effect of the polarizable medium will be manifested in stabilizing of the positively charged ions at different stages of the cascade. Therefore, the energies of the emitted electrons will be somewhat different from the cluster's case. The presence of additional solvation shells will further increase the efficiency of ICD and ETMD(3), but their overall impact will be moderate, mainly because of their larger distance to the metal ion [16,154]. The effect of the second solvation shell is expected to be more pronounced for ETMD(3) since its contribution to the decay width is given by $\Gamma_{ETMD(3)} \propto N_D \cdot N_I$, where N_D is the number of electron donors (6 in the first solvation shell) and N_I the number of ionizable water molecules (12 in the second solvation shell [102]). In contrast, the contribution of the second solvation shell to the ICD width is $\Gamma_{ICD} \propto N_I$. We estimated the increase of the ETMD widths due to a second solvation shell to be approximately 30 percent.

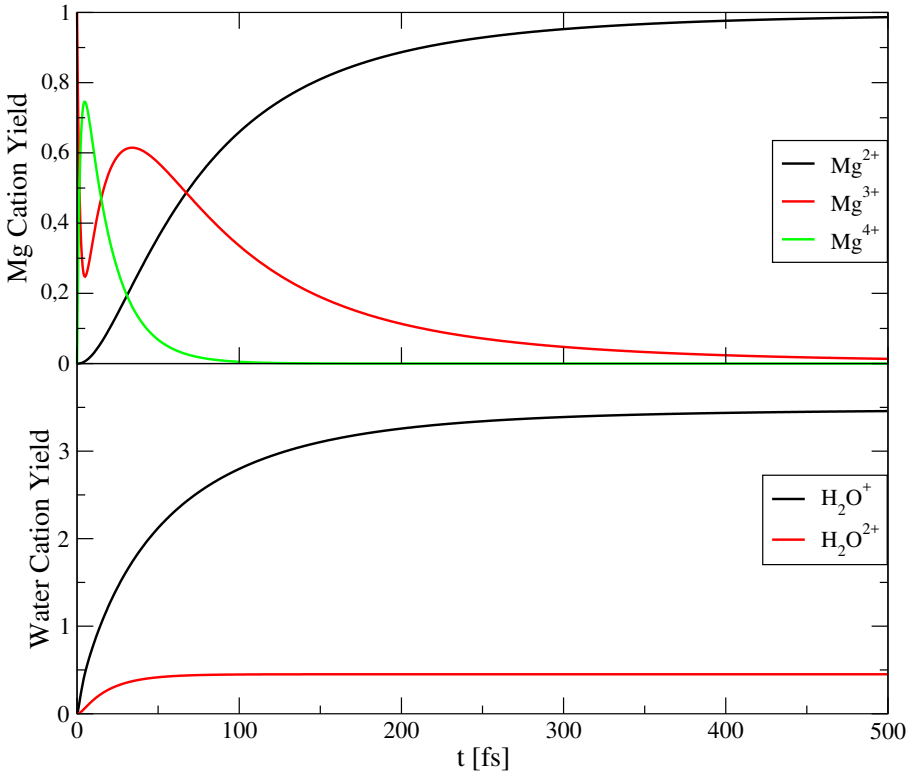

Figure 6.3: Yield of magnesium and water cations generated during the electronic decay cascade taking place after the core ionization of the $Mg^{2+}(H_2O)_6$ cluster. Repulsive nuclear dynamics occurring after the interatomic electronic decay steps are not taken into account. Reprinted with permission from Ref. [155]. Copyright (2016) by the Nature Publishing Group.

6.3 Impact of the nuclear dynamics on the electronic decay

Within the duration of the cascade a large amount of Coulombic repulsion energy (few tens of eV) is accumulated, due to the high metal charge and short distances to the ionized water neighbors. Therefore, repulsive nuclear dynamics accompany the electronic decay. Unfortunately, ascertaining the interplay between nuclear dynamics and electronic decay in microsolvated clusters by *ab initio* calculations goes beyond the scope of the present work. Therefore, we consider qualitatively the most probable nuclear dynamics scenarios and estimate their impact on the cascade duration and the branching ratios of electronic decay.

In small microsolvated clusters lacking the second solvation shell around the metal ion the nuclear dynamics is dominated by Coulomb explosions involving charged water molecules and the metal cation [141]. Its effect consists in removing the positive charge mostly as H_2O^+ from the vicinity of the metal ion. This, according to our estimates, leads to an increasing of the decay rates by as much as factor 2-2.5 when the water cations are gone. The effect is very pronounced for the $Mg^{3+}(2p^{-1}\ ^2P)$ cations, which can only decay by ETMD(3) in the presence of charged water molecules (see the tail at longer times in the Mg^{3+} population in Fig. 6.3). Removing the positive charge opens

the energetically higher lying ETMD(2) channels and increases the ETMD(2)/ETMD(3) ratio. Therefore, the production of H_2O^{2+} is increased at the expense of H_2O^+. The total numbers of electrons remain unchanged, however, their energies will be increased by up to a few eV. The speed of the Coulomb explosion can be estimated from the results obtained for H_2O^+-H_2O^+ produced by ICD of the water dimer, where a threefold increase in oxygen-oxygen distance (to 1 nm) occurs in 130 fs [156]. Due to the multiple charge of the metal the timescale of the Coulomb explosions releasing water cations from the microsolvated cluster is even shorter, presumably few tens of femtoseconds. This speed is comparable to or higher than the ETMD rates discussed above. Therefore, the Coulomb explosions set off by earlier interatomic steps of the cascade will proceed during the later ETMD steps and enhance them. ICD in the presence of positively charged neighbors is still sufficiently fast to outrun the repulsive nuclear dynamics. Nevertheless, already a moderate movement of the neighbors opens the strong ICD channels and reignites the ultrafast decay on the timescale of few femtoseconds. Hence, both ICD and ETMD at later stages of the cascade are enhanced by the Coulomb explosions.

In larger microsolvated clusters and aqueous solutions a proton transfer from a water cation to a neighboring water molecule is likely to occur [141, 146]. Highly accurate *ab initio* computations demonstrate that the onset of proton transfer in water dimers may occur already at about 5 fs and the transfer may be complete by 50 fs [145,157]. However, its prevalence and rate are sensitive to the nature of the initially ionized state. Joint theoretical and experimental investigation in liquid water put an upper boundary for the proton transfer at 40 fs [146]. Doubly ionized water molecule has been shown to lose two protons in solution within 4 fs [36]. These timescales indicate that proton transfer initiated by earlier interatomic steps of the cascade proceeds during the later ICD and ETMD steps. The protons move from the first to the second or a farther solvation shell of the metal cation. In this respect the effect of the proton transfer on the cascade will be similar to the one of Coulomb explosion discussed above: removing positive charge from the vicinity of the cation and enhancing the interatomic decay processes. Moreover, following proton transfer a neutral radical species (OH or O) remain in the vicinity of the metal cation. These radicals exhibit ionization potentials comparable to those of the water molecule (13.0 eV for OH, 13.6 eV for O) and will participate in ETMD(3). The overall result of both the charge removal and the appearance of additional radicals close to the metal ion will be to increase the decay rates of different interatomic steps by as much as a factor of 6.5. The ionization of the O and OH radicals will alter the distribution of the radical species, for example increasing the production of O (via OH^+) at the expense of OH.

We furthermore want to remark that in solutions we also may expect Coulomb explosion to occur and enhance the interatomic processes. Large Coulomb energy accumulated between Mg and water cations speaks in its favor. Hence, we expect a complicated fragmentation pattern for the cationic products of the interatomic decay involving Coulomb explosions and molecular dissociation in aqueous solutions. The fragmentation leads to the increase in ICD and ETMD rates and shortens the cascade duration. The character of the released chemical species is modified directly by the proton transfer processes and indirectly due to the sensitivity of interatomic decay rates to the presence of the positive charge.

6.4 Contribution of the decay cascade to the radiation damage

The electronic decay cascade initiated by the absorption of an X-Ray photon by the metal cation may be viewed from two different angles: the one of the cation itself, and the other one of the nearest neighbors or ligands. From the point of view of the nearest neighbors the probability of their damage by the ≈1150 eV Auger electrons is small. However, they are directly damaged in the interatomic processes becoming either singly or doubly ionized. In the case of water solutions the single ionization will lead to proton transfer reaction producing OH radical, while doubly ionized water is expected to produce atomic oxygen* [36]. The hydroxyl radical is highly reactive and causes oxidative damage to other molecules present in the solution (see e.g. [158]). Atomic oxygen is reactive as well and is admittedly a source of further damaging species such as H_2O_2 [159]. In addition to such direct damage to the nearest neighbors and the production of radicals, the interatomic processes result in the emission of electrons having energies <40 eV. Such electrons can be resonantly captured by the molecules in the near environment initiating efficient bond breaking reactions [38]. In total, the interatomic decay processes massively degrade the molecules in the immediate vicinity of the metal species through multiple ionizations releasing in their course both reactive electrons and radicals. If we are to neglect the interatomic processes, the decay of the $1s$ vacancy on Mg^{2+} would result in one (Auger) electron. Taking them into account and counting the damaging particles released in the complete cascade one would obtain on average 2.4 slow electrons in addition to a fast Auger electron and 4.3 radicals per each $1s$ vacancy. These values are supposed to further increase if one considers also the interatomic relaxation of the Mg^{5+} cations produced by the double Auger decay. Following our argumentation longer decay cascades with a higher number of reactive products can be anticipated for these cations.

In the decay cascade presented above the Mg ion which absorbs the X-ray photon reverts back to its initial electronic state within few hundreds of femtoseconds. At the same time the nearest environment of this ion is multiply ionized implying the production of a large number of reactive particles (radicals and slow electrons) at the metal's location. This shows that no change of the metal ion's charge on X-ray irradiation is by no means equal to no damage done. On the grounds of our detailed findings one may anticipate that the similar cascades generally hold also for other metal ions independently whether the ion reverts back to its initial charge or photoreduction is observed. Clearly, these cascades will be accompanied by extensive damage to the surrounding molecules. Note, that after only 10 fs already 28 % of the core ionized states ($Mg^{4+}(2s^{-1}2p^{-1}\ ^1P)$ and $Mg^{4+}(2s^{-2}\ ^1S)$) will undergo the Auger and the interatomic Coulombic decays. This sets off a Coulomb explosion leading to a modification of molecular geometry in the vicinity of the metal ion already at that short timescale. In a broader context, this finding demonstrates that studying interatomic decay processes is of great importance to estimate timescales of radiation damage in metalloproteins during X-Ray diffraction experiments.

*Since the atomic oxygen has a triplet electronic ground state, it has an equivalent of two radicals in our estimate of the reactive product yields.

Positioning of metal ions within or in close proximity to biomolecules makes the radiation damage particularly disruptive for the functions these molecules fulfill. Experimental evidence is available that irradiation of DNA molecules complexed with Ca^{2+} by X-rays at energies below and above the Ca K-edge showed about 30% enhancement in the induction of double strand breaks when the photon energy was increased across the K-edge [160]. Similarly, it was demonstrated that iron containing metalloenzymes were more efficiently deactivated when irradiated with the X-rays above the iron's K-edge [161]. We hope that the interatomic electronic cascades elucidated in this report will be useful in understanding the X-ray induced photochemistry and radiation damage of metal containing biomolecules.

6.5 Conclusions

In this chapter we investigated electronic relaxation of a core ionized metal cation in the microsolvated $Mg^{2+}(H_2O)_6$ cluster. We demonstrated that after the local Auger decay the metal undergoes a multistep electronic decay cascade on a timescale of few hundreds of femtoseconds. In this cascade, ICD and ETMD processes act in a complementary way, facilitating energy transfer from the metal to the water neighbors and electron transfer in the opposite direction, respectively. Thus, the core ionized metal cation returns to the original Mg^{2+} state and introduces a substantial damage to the environment by releasing slow electrons, ionizing the neighbors and setting of repulsive nuclear dynamics in its vicinity.

7 Impact of the metal's charge on ICD lifetimes in microsolvated clusters

The discussion of the interatomic electronic decay processes of microhydrated magnesium cations in the previous chapter revealed that in this system both ICD and ETMD proceed on a femtosecond timescale. The ICD lifetimes of the hexahydrated Mg^{3+} and Mg^{4+} cations with holes in the $2s$ orbital are remarkably short ($\approx$ 1 fs). Such ultrafast interatomic decay may induce repulsive nuclear dynamics in the vicinity of the metal on a femtosecond timescale. Therefore, studying the ICD lifetimes of metal atoms and parameters which govern them is important to elucidate the timescale of radiation damage in biomolecules containing metal atoms.

ICD, which is characterized by the transfer of the excess energy from the excited species to the neighbor, is driven by the correlation between the electrons located on the neighboring species. The long-range nature of the electron repulsion as well as the fact that the final states of ICD lie in the electronic continuum, explain the femtosecond timescale of this process [4,20,24,25,162]. The energy transfer nature of ICD determines the behavior of the width at large separations, R, between the excited species and a neighbor. At such distances ICD can be visualized as follows: the excited species de-excite emitting a virtual photon which is absorbed by the neighbor leading to its ionization. If the electronic transition in the excited species is dipole-allowed, the ICD width behaves as $1/R^6$ and grows fast with decreasing distance [154, 163]. At shorter interatomic distances the overlap between the electrons of the excited species and of the neighbor leads to the enhancement of the width relative to that predicted by the asymptotic behavior [154]. Thus, typical ICD lifetimes in rare gas dimers, which have equilibrium distances in the 3 to 4 Å range, are at few 10 fs to few 100 fs timescale: 64-92 fs (theory) [53, 164, 165] and 150±50 (experiment) in Ne dimer [25], 300-600 fs in He·Ne [24, 162], 75 fs in Ne·Ar [166]. The ICD lifetime becomes progressively shorter if more ionizable neighbors are present around the excited moiety. For example, the experimentally determined lifetime of inner-valence ionized bulk Ne atoms in a neon cluster is only 6 fs [23] as compared to the $\approx$ 100 fs lifetime of the inner-valence ionized neon dimer [25]. The ICD lifetime of the inner-valence ionized neon embedded in the C_{60} fullerene (τ_{ICD} = 1.6 fs) [167] becomes comparable to the Auger lifetime of the core-ionized Ne atom (τ_{Auger} = 1.9 fs) [125].

The combined effect of small interatomic separations and large number of neighbors explains the remarkably short computed ICD lifetimes of microsolvated magnesium ions discussed above. In this context, experiments on aqueous solutions demonstrate that

Parts of this chapter have been already published in
V. Stumpf, C. Brunken and K. Gokhberg, J. Chem. Phys. **145**, 104306 (2016).

not only magnesium but also the isoelectronic Na^+ and Al^{3+} cations decay by ICD on a timescale of few femtoseconds. Thus, Öhrwall et al. investigated ICD in the diluted aqueous solutions of the Na^+, Mg^{2+}, and Al^{3+} salts following the photoemission of a $2s$-electron of the metal ion [14]. The ICD process can be schematically represented as

$$M^{q+} \cdot H_2O + h\nu \rightarrow M^{(q+1)+}(2s^{-1}) \cdot H_2O \rightarrow M^{(q+1)+}(2p^{-1}) \cdot H_2O^+ + e_{ICD}, \qquad (7.1)$$

where M^{q+} denotes the metal cation with the initial charge q. ICD lifetimes, extracted from the Lorentzian widths of the photoelectron spectral lines, were 3.1 fs (Na^+), 1.5 fs (Mg^{2+}) and 0.98 fs (Al^{3+}). Obviously, they showed a clear trend of decreasing monotonically with the growing charge of the metal. The authors identified the equilibrium M^{q+}·H_2O distances in the initial state, and the polarization of water neighbors induced by the cations in the initial and the decaying states as the important parameters determining the ICD lifetime. Increasing the charge of the cation leads to the decreasing equilibrium distances and to the increased polarization of the water neighbors. Both effects diminish the average distance between the electrons localized respectively on the cation and on the water, which leads to the increasing ICD width in this isoelectronic series.

It is experimentally impossible to disentangle these two effects. However, *ab initio* computational methods allow us to study the influence of both the intermolecular distance and neighbor's polarization on the ICD lifetimes separately. We conducted *ab initio* calculations of ICD widths (i.e. inverse ICD lifetimes) in the small Ne·H_2O, Na^+·$(H_2O)_m$ (m = 1-4), and Mg^{2+}·$(H_2O)_n$ (n = 1-6) clusters following the removal of a $2s$-electron of Ne, Na^+, and Mg^{2+}. We did not address ICD of microsolvated aluminum for the reason that its solvation shell structure is pH-dependent [168] and cannot be easily modeled by a single cluster. Instead, we extended the isoelectronic series to the lower charged species and studied ICD rate in Ne·H_2O. We analyzed the dependence of ICD widths on the atom-water distances in monohydrated clusters both including and excluding polarization effects in the decaying state. We furthermore analyzed the dependence of ICD widths on the number of water neighbors at fixed metal-water distances.

7.1 ICD widths of $2s$-ionized states in Ne·H_2O

We begin our discussion with the Ne·H_2O cluster, which bears no positive charge and formally extends the isoelectronic M^{q+}·H_2O (M^{q+} = Na^+, Mg^{2+}) series towards a lower value of q. In the electronic ground state of the Ne·H_2O cluster the weak interaction between the neutral neon atom and the water molecule is reflected by a relatively large equilibrium Ne-O distance (R_{eq} = 3.22 Å), compared to the R_{eq} values of the microsolvated metal cations (see Tab. 7.1). The binding energy of a neon $2s$-electron is larger than the lowest cluster double ionization energies (DIE) in the neutral Ne·H_2O cluster at R_{eq} (see Tab. 7.1). Therefore, ICD channels are open and the ICD electron should have energies between 4 eV and 10 eV. Ejection of electrons from any outer-valence orbital of the water molecule is allowed in ICD for all neon-oxygen distances larger than 2 Å. Since no decay channels become closed in this range, the ICD width behaves smoothly as a function of R (see Fig. 7.1). The ICD lifetime at the equilibrium R is 49.8 fs; it lies

Table 7.1: Atom-water equilibrium distances R_{eq}, ionization energies of $2s$-electrons (IE), double ionization energies (DIE) and ICD lifetimes of isoelectronic $A^{q+}{\cdot}H_2O$ clusters at respective R_{eq}. For $Na^+{\cdot}H_2O$ and $Mg^{2+}{\cdot}H_2O$ the values of R_{eq} correspond to the equilibrium geometries of the $Na^+{\cdot}(H_2O)_4$ and $Mg^{2+}{\cdot}(H_2O)_6$ clusters (see chapter 3.6.1). The DIE correspond to the $A^{q+1}(2p^5 3s^0){\cdot}H_2O^+(ov^{-1})$ final states of ICD. The range of DIE values is due to ionization of different outer-valence electrons of the water molecule in ICD.

A^{q+}	R_{eq} [Å]	IE [eV]	DIE [eV]	τ_{ICD} [fs]
Ne	3.22	47.9	37.9 - 44.0	49.8
Na^+	2.30	78.3	69.9 - 76.0	7.0
Mg^{2+}	2.08	115.3	109.4 - 115.0	3.6

within the typical sub-100 fs range of ICD lifetimes for the rare gas dimers containing neon [21,53]. However, our results deviates from the 86 fs obtained by Ghosh et al. [169] for the same system using a conceptually different computational technique (complex absorbing potential augmented EOM-CCSD, CAP/EOM-CCSD). The deviation can not be explained by the difference in the equilibrium structures, as was verified by an additional ICD lifetime calculation for the geometry used in Ref. [169]. It is, probably due to the difference in approaches used to compute electronic resonances. Similar differences in ICD widths computed by Fano-ADC and CAP/EOM-CCSD methods were reported for van-der-Waals systems containing neon [170]. Another explanation, provided by the authors of Ref. [169], is that the basis set used in their calculation was not sufficiently large. At large $Ne{\cdot}H_2O$ separations the computed ICD width exhibits the $1/R^6$ behavior characteristic of the energy, or virtual photon transfer, process. At intermediate interatomic distances ($R < 5$ Å) the full *ab initio* width grows faster than the asymptotic $1/R^6$ curve. The enhancement of the accurate *ab initio* width relative to the virtual photon transfer width is attributed to the overlap of the electrons localized on different units [154], which is completely neglected in the virtual photon transfer model.

The magnitude of the ICD width depends on the average distance between the electrons located on the two units. The resulting enhancement of the width amounts to 30% at R_{eq}. In the ground state of $Ne{\cdot}H_2O$ the absence of the positive charge on Ne results in a large equilibrium Ne-O distance and a small overlap of the electronic densities of neon and water. Following the inner-valence ionization, which promotes the system into the decaying state, a positive charge appears on Ne distorting the electronic density on the water molecule towards the neon cation and decreasing the average distance between the electrons on the two moieties.

An interesting observation is that any enhancement of the width over the $1/R^6$ asymptotic behavior in the coordinate range of interest is due to the polarization of the water neighbor by the positive charge on the excited moiety. Indeed, the *ab initio* width obtained when the neighbor's polarization is excluded behaves as $1/R^6$ for all R of interest (see Fig. 7.1). Since this conclusion is correct for the case of Ne, it should be also correct for the isoelectronic Na^+ and Mg^{2+} which have more compact electronic orbitals. Therefore, continuing the asymptotic widths to shorter interatomic distances should give us the estimate of ICD widths in $Na^+{\cdot}H_2O$ and $Mg^{2+}{\cdot}H_2O$ where the effect of neighbor polarization in both ground and decaying states is neglected.

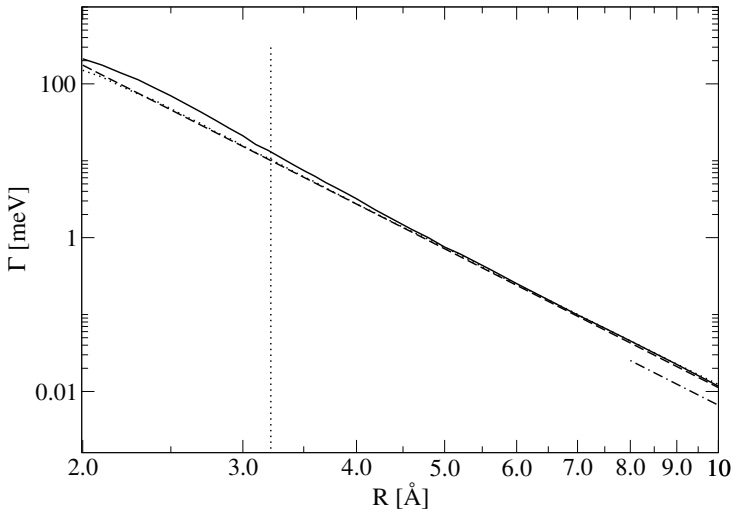

Figure 7.1: ICD width of the $Ne^+(2s^{-1})$ state in the Ne·H_2O cluster as a function of the Ne-O separation. (Solid line) The width obtained in the full *ab initio* computation. (Dotted line) The *ab initio* decay width computed excluding the interatomic relaxation in the decaying state. (Dashed line) Extrapolation of the asymptotic $1/R^6$ behavior which is seen to correspond to the ICD width when all polarization of the water neighbor is neglected to shorter interatomic distances. (Dashed-dotted line) The ICD width computed using the virtual photon transfer model in Eq. 7.2 where the experimental excitation energies and transition dipole moments of Ne^+, and the photoionization cross sections of H_2O were utilized. Note the similarity of different ICD widths at large R. The neon-oxygen distance corresponding to the electronic ground state equilibrium geometry is shown as a vertical dotted line. Reprinted from Ref. [171]. Copyright (2016), with permission from AIP Publishing LLC.

A way to estimate the error of the Fano-ADC-Stieltjes method is the comparison of the numerical ICD widths at asymptotic separations between the species with those obtained by the virtual photon model [154, 163] which relies on the experimentally determined properties of the isolated units:

$$\Gamma = \frac{3c\left|\vec{D}_M\right|^2 \sigma_{H_2O}(\omega)}{\pi\omega R^6}. \tag{7.2}$$

Here, $\vec{D}_M$ is the transition dipole moment corresponding to the $(2s^{-1})\rightarrow(2p^{-1})$ transition in the inner-valence ionized atom or cation, ω is the energy of the corresponding virtual photon, $\sigma_{H_2O}(\omega)$ is the ionization cross section of H_2O averaged over the photon's polarization at this energy, and c the speed of light (all parameters given in atomic units). The asymptotic ICD width computed using the experimental parameters of isolated Ne [111] and water molecule [172] is plotted in Fig. 7.1. Comparing it with the *ab initio* width one can see that the virtual photon model predicts an ICD width 1.9 times smaller than the numerical value.

This discrepancy can be explained by the fact that the transition dipole moment and

ionization cross sections, present implicitly in the *ab initio* approach, contain errors at the level of approximation we employ. Thus, the decaying $Ne^+(2s^{-1})$ state of Ne is constructed using both $1h$ and $2h1p$ configurations, necessary to include the intra-atomic correlation and relaxation effects of the $2s$-hole. The 2p-hole in the final $Ne^+(2p^{-1})$ state is constructed using only $1h$ configurations. To estimate the errors introduced by this restricted and unbalanced representation of the initial and final states we carried out an auxiliary CI calculation for Ne. It included all $1h$ and $2h1p$ configurations constructed from the neutral Ne reference state for the calculation of the $Ne^+(2s^{-1})$ decaying state, and only the $1h$ configurations corresponding to the $2p$-holes for the $Ne^+(2p^{-1})$ final state. Compared to the experimental values the transition energy, ω, was underestimated by a factor of 0.9, whereas the transition moment, $\vec{D}_M$, was too high by a factor of 1.1. The ionization cross section $\sigma_{H_2O}(\omega)$ implicit in the present Fano-ADC-Stieltjes method is constructed using only singly excited $1h1p$ configurations. As was demonstrated by Ruberti *et al.* [173], the computed cross section of water overestimates the experimental one in the photon energy range of interest (25 eV $< \omega <$ 40 eV) if only single excitations are used. Moreover, an additional error in $\sigma(\omega)$ appears due to the wrong energy of the virtual photon implicit in the ADC calculation of the width. Altogether we may estimate the error of the ADC(2x) scheme at asymptotic distances to be a factor 1.8 of the virtual photon model; the value close to the factor 1.9 was actually obtained.

7.2 ICD widths of $2s$-ionized states in $Na^+ \cdot H_2O$ and $Mg^{2+} \cdot H_2O$

Replacing Ne by Na^+ modifies the initial state of the system considerably. The attractive interaction between the sodium cation and the polar water molecule reduces the equilibrium R_{eq} value to 2.30 Å ,compared to the 3.22 Å in $Ne \cdot H_2O$. At such interatomic distances the internuclear repulsion in the final states of ICD is so strong that the kinetic energy of the emitted electrons is lower (2.3 eV to 8.4 eV) than in the $Ne \cdot H_2O$ (see Tab. 7.1) in spite of the higher excess energy (≈32 eV) of $Na^{2+}(2s^{-1})$.

The presence of a positively charged ion in the initial state leads to the polarization of the water already in the initial state. Therefore, the width computed when the interatomic relaxation is omitted deviates at $R < 5.0$ Å from the $1/R^6$ behavior, unlike in the case of $Ne \cdot H_2O$, where the deviation sets in at shorter R. At R_{eq} this width is enhanced by 30% relative to the $1/R^6$ curve continued from the asymptotic distances. The polarization of H_2O increases even further following the $2s$-ionization of Na^+ which promotes the system to the decaying state. Including the interatomic relaxation in the calculation makes the enhancement of the ICD width even more pronounced, so it is enhanced by the factor of 2.1 at R_{eq}. We conclude that the original polarization of H_2O by Na^+ in the initial state as well as the additional polarization induced by removing the $2s$-electron lead to much stronger electron overlap and consequent enhancement of the ICD width relative to the asymptotic $1/R^6$ behavior.

Combined effect of shorter equilibrium interatomic distances, as well as strong polarization of the water molecule results in the very short ICD lifetime of 7.0 fs. A compara-

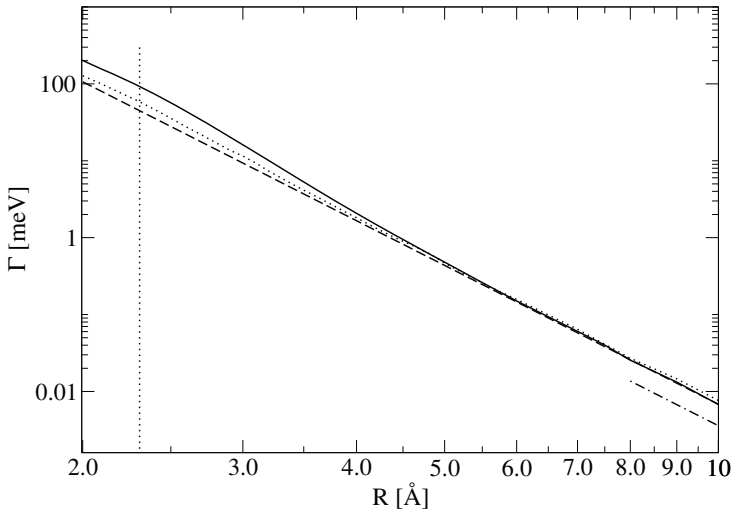

Figure 7.2: ICD width of the $Na^{2+}(2s^{-1})$ state in the $Na^+{\cdot}H_2O$ cluster as a function of the Na-O separation. (Solid line) The width obtained in the full *ab initio* computation. (Dotted line) The *ab initio* decay width computed excluding the interatomic relaxation in the decaying state. (Dashed line) Extrapolation of the asymptotic $1/R^6$ behavior to shorter interatomic distances which corresponds to the ICD width when all polarization of the water neighbor is neglected. (Dashed-dotted line) The ICD width computed using the virtual photon transfer model in Eq. 7.2 where the experimental excitation energies and transition dipole moments of Na^{2+}, and the photoionization cross sections of H_2O were utilized. The sodium-oxygen distance corresponding to the $Na^+{\cdot}H_2O$ electronic ground state equilibrium geometry is shown as a vertical dotted line. Reprinted from Ref. [171]. Copyright (2016), with permission from AIP Publishing LLC.

ble lifetime was obtained previously for a single geometry calculation in $Na^+{\cdot}H_2O$ using a simpler, perturbation theory based Wigner-Weisskopf method [174]. The lifetime at $R = 2.21$ Å was found to be 3.5 fs, while our calculation gives 5.5 fs for this geometry. The ICD widths of the decaying state computed *ab initio* and using the virtual photon transfer model are shown in Fig. 7.2. The error of the Fano-ADC-Stieltjes method in the asymptotic regime relative to the virtual photon model is similar to the one in $Ne{\cdot}H_2O$: the *ab initio* method overestimates the result given by the virtual photon model by a factor of 2.0.

The extension of this isoelectronic series to $Mg^{2+}{\cdot}H_2O$ continues the observed trend; the equilibrium distance and the corresponding ICD lifetime decrease to 2.08 Å and 3.6 fs respectively, and the kinetic energy of the ICD electrons becomes even lower (0.3 - 4.1 eV). The *ab initio* widths corresponding to the calculations done with and without accounting for the interatomic relaxation are shown in Fig. 7.3. Since in the initial state the doubly charged Mg^{2+} polarizes the water neighbor stronger, the corresponding width enhancement relative to $1/R^6$ behavior (see the dashed curve in Fig. 7.3) is larger than in the case of Na^+ and it amounts to 70% at R_{eq}.

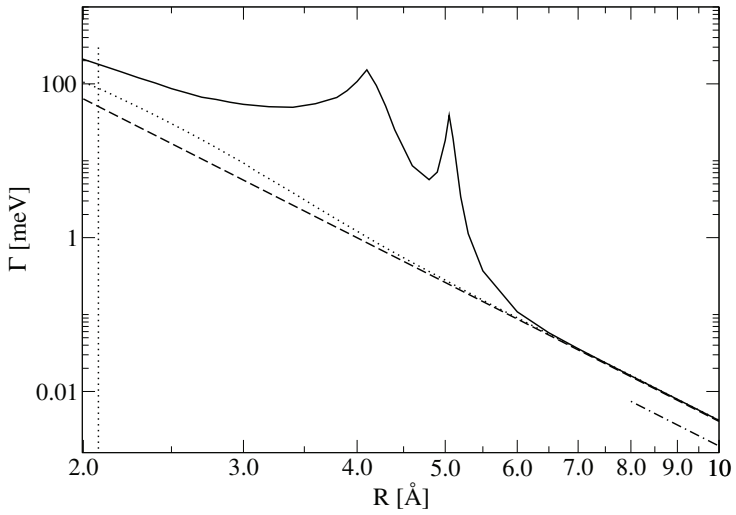

Figure 7.3: ICD width of the $Mg^{3+}(2s^{-1})$ state of the $Mg^{2+}{\cdot}H_2O$ cluster as a function of the Mg-O separation. (Solid line) The width obtained in the full *ab initio* computation. (Dotted line) The *ab initio* decay width computed excluding the interatomic relaxation in the decaying state. (Dashed line) Extrapolation of the asymptotic $1/R^6$ behavior to shorter interatomic distances which corresponds to the ICD width when all polarization of the water neighbor is neglected. (Dashed-dotted line) The ICD width computed using the virtual photon transfer model (see Eq. 7.2) where the experimental excitation energies and transition dipole moments of Na^{2+}, and the photoionization cross sections of H_2O were utilized. The magnesium-oxygen distance corresponding to the $Mg^{2+}{\cdot}H_2O$ electronic ground state equilibrium geometry is shown as a vertical dotted line. Reprinted from Ref. [171]. Copyright (2016), with permission from AIP Publishing LLC.

Including the configurations responsible for the interatomic relaxation in the calculation of the ICD state leads not only to the increase in Γ due to the additional polarization of H_2O in the ICD state, but also to the appearance of the charge transfer states in the spectrum. The ICD $Mg^{3+}(2s^{-1}){\cdot}(H_2O)$ state crosses and interacts with the $Mg^{2+}(2s^{-1}3s^1){\cdot}H_2O^+$ resonance charge transfer states at R = 3.8-5.0 Å which leads to the non-monotonic behavior and strong enhancement of the ICD width at 3.8-5.0 Å . At R = 4 Å the lifetime is approximately 6 fs, comparable with ICD lifetimes at much shorter interatomic distances or autoionization lifetimes of the isolated $Mg^{3+}(2s^{-1}3s^1)$ atom (2-3 fs) [175]. Such enhancement of the ICD widths due to interactions with charge transfer states is expected to be of general importance in the higher charged cations. At the equilibrium R the full width is enhanced relative to the $1/R^6$ behavior by the factor of 3.5. It is instructive to compare the behavior of ICD widths with R throughout the $Ne{\cdot}H_2O$, $Na^+{\cdot}H_2O$, $Mg^{2+}{\cdot}H_2O$ isoelectronic series (see Fig. 7.4). At large interatomic distances, where the $1/R^6$ behavior is valid, ICD is fastest for Ne and slowest for Mg^{2+}. Higher positive charge leads to a lower transition dipole moment, to a higher virtual photon energy, and to a lower value of the ionization cross section of H_2O which results in

smaller Γ (See Eq. 7.2). At shorter R's the positive charge on the metal cations induces a polarization of the water neighbor both in the initial and decaying states, leading to stronger enhancement relative to the $1/R^6$ behavior compared to Ne·H_2O. As the result the ICD widths at the respective equilibrium geometries are 13 meV, 92 meV and 178 meV, while at $R = 2.0$ Å they nearly coincide. In the case of sodium the ICD width remains lower than the one for Ne down to the shortest interatomic distances. In the case of magnesium the interaction with the charge transfer states makes the electronic decay more efficient than the decay of neon in the 2.3-5.5 Å range.

One can also attempt to answer the question which parameter - the interatomic separation R or the water polarization induced by the charged moiety - is primarily responsible for the order of the ICD widths in the studied isoelectronic series. If we consider the ICD widths which do not include the effect of water polarization for the Na^+·H_2O, Mg^{2+}·H_2O clusters at the equilibrium distance of Na^+·H_2O (2.30 Å) we find that their ratio is 1.7:1.0. The ratio of the same ICD widths which do not include the effect of water polarization computed at respective equilibrium internuclear distances of the the Na^+·H_2O (2.30 Å) and Mg^{2+}·H_2O (2.08 Å) clusters is 1.0:1.1. The ratio of the ICD widths which include the effect of water polarization computed at respective equilibrium internuclear distances of the the Na^+·H_2O (2.30 Å) and Mg^{2+}·H_2O (2.08 Å) clusters is 1.0:1.9. Therefore, we conclude that the equilibrium distances and the polarization induced by the cationic charge on H_2O are equally important in determining the ordering of the ICD widths in the Na^+·H_2O, Mg^{2+}·H_2O series.

7.3 ICD widths of $2s$-ionized states in Na^+·$(H_2O)_n$ and Mg^{2+}·$(H_2O)_n$

Metal ions in their natural environment (coordination complexes, solutions etc.) are surrounded by a coordination shell of ligands or solvent molecules. The ICD width should be linear with the number of the equivalent neighbors as long as these neighbors do not interact. There are not many calculations of the ICD width as a function of the number of neighbors. Thus, linear behavior was found theoretically in the Ca·He_n clusters [94]; the ICD width of the inner-valence ionized neon atom in Ne_n, however, increased faster than linear with n [54].

We would like to determine this behavior for larger microsolvated clusters of Na^+ and Mg^{2+}. Results of calculations in Na^+·$(H_2O)_m$ for m = 1-4 using a simpler Wigner-Weisskopf method show a lot of scatter and do not allow to extract the Γ behavior with the number of neighbors [174]. However, one would expect a nonlinear dependence of the ICD width on the coordination number for microsolvated cations. The interactions of the ligands with the metal cation are non-additive and become weaker with the growing coordination number, in particular, if the metal cation carries a high charge [176, 177]. This can be explained by the fact that the electronic interaction of a specific ligand with the cation is modified by the presence of the remaining ligands, which become polarized and shield the charge on the metal, weakening its interaction with the ligand in question. Similar effect should also be observed in the behavior of Γ with the number of ligands. In larger clusters individual molecules should be less polarized by the cation due to the

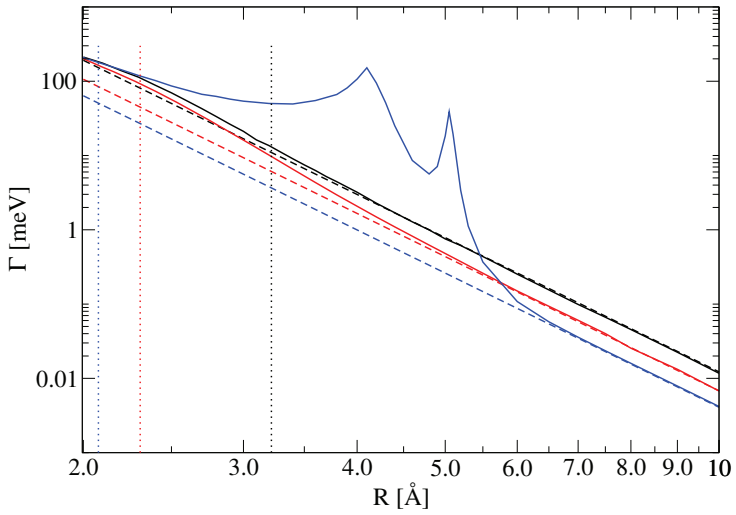

Figure 7.4: ICD widths of the $2s$ ionized $M^{q+}(2s^{-1})\cdot H_2O$ states of the isoelectronic series of microsolvated clusters $Ne\cdot H_2O$, $Na^+\cdot H_2O$, $Mg^{2+}\cdot H_2O$. (Solid lines) Full *ab initio* ICD width. (Dashed lines) Extrapolation of the asymptotic $1/R^6$ behavior to shorter interatomic distances which corresponds to the ICD width when all polarization of the water neighbor is neglected. Note the ordering of the curves in the asymptotic regime and at small interatomic distances.Reprinted from Ref. [171]. Copyright (2016), with permission from AIP Publishing LLC.

shielding of its charge by the rest of the neighbors. Therefore, the contribution of the individual ligands to the total ICD width should decrease with the number of neighbors. The gradual filling up of the first coordination shell of the sodium cation (see Fig. 7.5), leads only to a weak nonlinearity of the corresponding ICD width. In the case of the tetra-coordinated sodium cation the difference between the *ab initio* result and the linear extrapolation is approximately 6%. Switching off the interatomic relaxation in the decaying state (see Fig. 7.5) makes the deviation from the linear behavior even weaker. A more pronounced nonlinearity in Γ can be observed in $Mg^{2+}\cdot(H_2O)_n$ when n is varied. This is due to the stronger polarization of H_2O by the $Mg^{3+}(2s^{-1})$ ion in the decaying state and to the consequently stronger shielding of the ionic charge compared to the $Na^+\cdot(H_2O)_m$ clusters. Both the higher charge of the magnesium cation and the smaller metal-oxygen distances are responsible for this effect. Thus, for the tetra-coordinated Mg^{2+} a deviation from linear behavior of 25% occurs, while at the maximum coordination number of 6 it reaches an even higher value of 31%. In contrast to $Na^+\cdot(H_2O)_m$ clusters, excluding the additional polarization in the decaying state decreases this deviation markedly to 12% for $n = 6$. This shows that the polarization induced by the additional charge in the decaying state is mostly responsible for the deviation from the linear behavior. In conclusion, the linear extrapolation approach is expected to give reasonable results for metal cations with a low charge in the initial state, where the metal-ligand distances are larger and the polarization of ligands in the

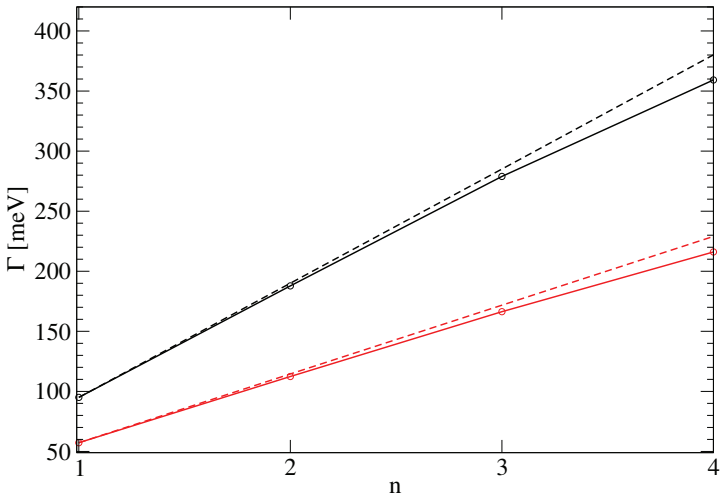

Figure 7.5: ICD width as the function of the coordination number n in $Na^+ \cdot (H_2O)_n$. (Full black line) the full *ab initio* result; (dashed black line) a linear extrapolation from the decay width of the singly coordinated Na^+. The corresponding red lines belong to computations, where polarization of the water neighbors in the decaying state was excluded. The calculations were done for cluster geometries obtained from the fully optimized $Na^+ \cdot (H_2O)_4$ one as described in chapter 3.6.1.Reprinted from Ref. [171]. Copyright (2016), with permission from AIP Publishing LLC.

initial [105] and decaying states is weaker. The larger the charge on the metal is, the larger deviation from the linear behavior of the ICD width with n is expected.

Finally, we would like to establish a connection between the *ab initio* results reported above and the ICD lifetimes of Na^+ and Mg^{2+} in aqueous solution determined experimentally by Öhrwall et al. [14]. The first coordination shell of the cation makes the major contribution to the ICD width of the $2s$-ionized state. We estimate that including the second solvation shell would increase the width only weakly (by about 3%). Therefore, calculations in microsolvated clusters are expected to give accurate ICD widths in dilute solutions. In the case of Mg^{2+} the coordination number distribution in aqueous solution is narrow with the maximum at $n = 6$ [102]. Furthermore, the metal-oxygen distance in the $Mg^{2+} \cdot (H_2O)_6$ cluster (2.08 Å) lies in the range of experimental values for the solvating Mg^{2+} (2.00-2.15 Å) [101]. The Fano-ADC-Stieltjes method yields 0.84 fs as the lifetime in the cluster, while the experimental value in solution is 1.5 fs. The discrepancy between the computed and the experimental results lies within the error of the Fano-ADC-Stieltjes method (factor 2.2) which we estimated by comparing the virtual photon model with the *ab initio* calculation.

Due to the rather broad distribution of the coordination numbers and metal-oxygen interatomic distances for Na^+ in aqueous solution [178], a comparison with a cluster ICD lifetime is less reliable. The experimental lifetime was found to be 3.1 fs, while the calculations in the tetra-coordinated cluster give 1.8 fs. The *ab initio* result lies within the

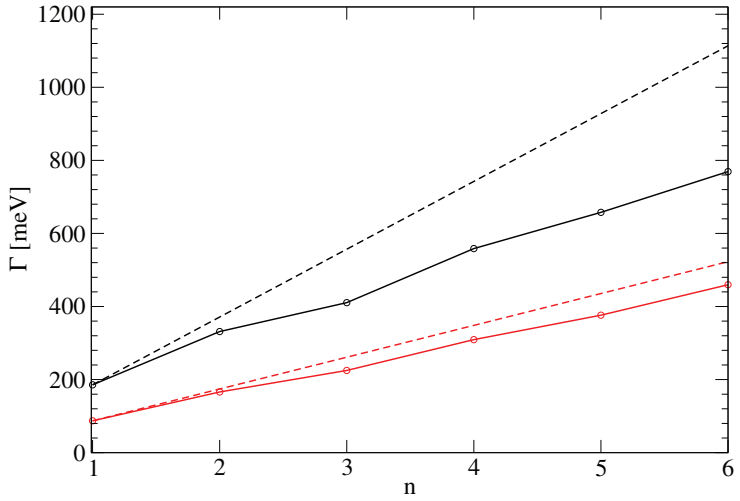

Figure 7.6: ICD width as the function of the coordination number n in $Mg^{2+}\cdot(H_2O)_n$. (Full black line) the full *ab initio* result; (dashed black line) a linear extrapolation from the decay width of the singly coordinated Mg^{2+}. The corresponding red lines belong to computations, where polarization of the water neighbors in the decaying state was excluded. The calculations were done for cluster geometries obtained from the fully optimized $Mg^{2+}\cdot(H_2O)_6$ one as described in chapter 3.6.1. Reprinted from Ref. [171]. Copyright (2016), with permission from AIP Publishing LLC.

error of the Fano-ADC-Stieltjes method (factor 2.0). In addition, in comparing the ICD widths for Na^+ one should keep in mind that penta- and higher coordinated structures are prominent in a solution. An *ab initio* calculation which takes into account statistical distribution of nearest solvent shells will, therefore, result in ICD lifetime shorter than 3.6 fs. Thus, average experimental values for the sodium-oxygen distance and coordination number are 2.34 Å and 5.2, respectively [102]. Inserting these parameters in the pairwise approximation with a 10% nonlinearity correction and 2.0 correction factor of the Fano-ADC-Stieltjes method we obtain a shorter lifetime of 3.3 fs. Interestingly, the ratio of the *ab initio* width in $Mg^{2+}\cdot(H_2O)_6$ to the one in $Na^+\cdot(H_2O)_4$ nearly equals the experimental ratio, 2.14 to 2.06. The decrease of the ICD lifetime due to the larger average coordination number of the sodium in solution compared to the $Na^+\cdot(H_2O)_4$ cluster is compensated by the larger average sodium-oxygen distance.

7.4 Conclusions

In this chapter we investigated charge dependent parameters determining ICD lifetimes of isoelectronic microhydrated Na^+ and Mg^{2+} metal ions after 2s ionization. We showed that at large metal-oxygen distances ICD lifetimes decrease with the growing charge as predicted by the virtual photon model. At decreasing metal-oxygen distances polarization of the water neighbor enhances ICD the stronger the higher the charge of the metal

is. In the $Mg^{3+}{\cdot}H_2O$ cluster interactions with $Mg^{2+}{\cdot}H_2O^+$ charge transfer states occur at intermediate metal-oxygen distance, strongly enhancing the electronic decay.We conclude that the ordering of the ICD lifetimes observed in the experiment is both due to shorter metal-oxygen distance and stronger polarization of the water ligand in the case of the magnesium cation. We furthermore showed that the induced polarization of the water molecules leads to a slower than linear growth of the ICD width with the number of equivalent water neighbors; the nonlinearity is stronger for the higher charged Mg^{2+} cation.

8 Conclusions and Outlook

In this work we investigated by means of *ab initio* computational methods non-local electronic decay processes which involve energy transfer (Interatomic Coulombic Decay or ICD) and electron transfer (Electron Transfer Mediated Decay or ETMD) between positively charged ions and their environment. ICD - which has been extensively theoretically and experimentally studied for about two decades - is an established ultrafast decay pathway in weakly bound chemical environments, whereby electronically excited species relax by ionizing their neighbors. What we found and reported in this thesis is that the relatively obscure ETMD process is an efficient pathway for the redistribution of localized positive charge in weakly bound medium. We carried out *ab initio* studies of ETMD in several systems which comprise atomic cations in their electronic ground state configuration, i.e. atomic cations with a low excess energy embedded in a van-der-Waals or hydrogen bonded chemical environment. We characterized ETMD in this class of systems with respect to its timescale and to the experimental observables, such as energies of emitted slow electrons or kinetic energy released in Coulomb explosion. The ICD process was also investigated, with emphasis on the ultrashort timescales observed for metal cations surrounded by water molecules.

The environment is doubly ionized in an ETMD process, therefore, it can be utilized as an efficient mechanism for the double ionization of the atoms or molecules adjacent to the cation. To clarify this idea we investigated the double ionization of a magnesium atom via the ETMD(2) relaxation of an attached He^+ cation. In our study, this cation is created via photoionization of the helium atom. The joint process of the photoionization and ETMD(2) is equivalent to a one-photon double ionization of the magnesium atom. Our calculations show that ETMD is able to suppress the competing RCT process and efficiently doubly ionizes the magnesium. Therefore, the double ionization cross section of Mg with the attached He atom is comparable to the photoionization cross section of helium. In relative terms it is three orders of magnitude larger than the cross section of the direct one-photon double-ionization of the isolated magnesium atom. The experimental verification of this double ionization scheme was realized in helium nanodroplets doped with magnesium clusters. Both intact doubly ionized magnesium clusters and singly ionized fragments stemming from the fission of the doubly ionized magnesium clusters were detected. These products appear only above the ionization threshold of helium and only in coincidence with slow ETMD electrons. We propose the one-photon double ionization via ETMD for experimental production and further investigation of molecular dications in cold environment such as helium nanodroplets. Molecules with low double ionization potentials, e.g. polyacenes are suitable immediate candidates for such studies.

From the point of view of a cation undergoing ETMD, this decay mechanism reduces its charge by one, i.e. it constitutes a purely electronic mechanism of partial neutralization which needs not involve any motion of the nuclei. The energy conservation condition

requires the electron affinity of the cation to be higher than the double ionization potential of the environment. Therefore, ETMD as a mechanism of partial neutralization is particularly important for multiply charged cations which are produced by the Auger decay. Our calculations demonstrate that energetically low $Ne^{2+}(2p^{-2})$ cations produced by the KLL Auger decay of the neon atom undergo ETMD(2) process and are partially neutralized in the presence of a single Xe neighbor. The Ne^{2+}·Xe cluster represents an ideal system for the detailed study of ETMD(2) in a coincident experiment and to facilitate such measurements we computed the kinetic energy spectra of the ETMD electrons and the KER spectra of the nuclei. If ETMD(2) is energetically forbidden, in larger systems ETMD(3) may take over its role as we show for the Ne^{2+}·Kr_2 cluster since the delocalization of the positive charge over two neighbors lowers its threshold. The lifetimes of ETMD in the Ne^{2+}·Xe, Ne^{2+}·Kr_2 and in the the He^{+}·Mg cluster discussed above lie in the picosecond range at the equilibrium geometries of the respective neutral clusters. Therefore, ETMD in these small, weakly bound van-der-Waals clusters is accompanied by nuclear dynamics. It is set off by the creation of positive charge in the Auger decay following the core ionization and causes a shortening of interatomic distances between the cation and the neighbors. For the Ne^{2+}·Kr_2 cluster we observed a reduction of the ETMD(3) lifetime by an order of magnitude due to the nuclear dynamics. This phenomenon, which is expected to be of general importance for cations created in a polarizable medium, leads to the enhancement of ETMD rate. This findings suggest that in larger clusters due to the larger number of neighbors ETMD occurs on the femtosecond timescale and becomes the leading neutralization process for highly charged ions. Experimental evidence for an Auger-ETMD(3) cascade was provided in large mixed neon-krypton clusters. Slow electrons and Ne^{+}/Kr^{+}/Kr^{+} triples of ions were recorded in coincidence after the ionization of the neon-krypton clusters above the K edge of neon. Analysis of the experimental data clearly shows that for each Auger decay event which takes place on the Ne-Kr interface in the cluster there is an ETMD event which partially neutralizes the Ne^{2+} cation and redistributes the charge across the Ne-Kr boundary.

Both aspects of ETMD as an electronic decay mechanism which partially neutralizes a cation and which doubly ionizes its environment play an essential role in understanding the X-Ray induced radiation damage of systems containing metal cations. Our calculations in the microsolvated Mg^{2+}·$(H_2O)_6$ cluster reveal that core ionization of Mg^{2+} initiates a cascade of electronic decay steps since all electronic states of Mg^{3+} and Mg^{4+} cations lie in the electronic continuum. The decay cascade consists of ETMD and ICD steps and ultimately returns the magnesium cations into the original Mg^{2+} state. Each ICD step releases the excess energy from the excited cations while each ETMD step of the cascade reduces the charge of the metal cation with a low excess energy by one. At the same time, each ICD step ionizes the environment singly and each ETMD step ionizes it doubly. Therefore, the decay cascade leads to a massive degradation of the water solvation shell. We estimate that, on average, 4.3 radicals and 2.4 slow electrons are released by the decay cascade. Importantly, the duration of the cascade is approximately 220 fs at the frozen nuclei approximation; allowing for nuclear dynamics to occur should shorten this duration even further. This findings demonstrate that X-Ray absorption in metals is able to introduce direct and indirect damage to biomolecules on a femtosecond timescale. In this context, it would be instructive to study X-Ray induced interatomic

decay cascades in small metal containing biomolecules (e.g. Mg^{2+}-ATP, chlorophyll) and to estimate the contributions of the direct and indirect damage. Such molecules can in principle be handled by the computational methods presented in this work.

We noted above that the total duration of the interatomic decay cascade in the $Mg^{4+}\cdot(H_2O)_6$ cluster was 220 fs. This value can be seen as an upper bound since we neglected nuclear dynamics accompanying the electronic decay. We expect the nuclear dynamics to remove positively charged moieties (e.g. protons or intact water cations) produced by early steps of the cascade and thus to open decay channels closed due to the presence of these moieties. Nuclear dynamics simulations could help to understand the mechanisms of such charge withdrawal and provide the corresponding timescales. This knowledge would allow to estimate the duration of the interatomic cascades following Auger decay more precisely. We furthermore expect that nuclear dynamics could play an important role for the timescale of interatomic decay of highly charged cations, such as e.g. Mg^{4+}, in an extended solvation environment. The positive charge may induce a proton transfer to a second solvation shell of the metal. This would impact the interatomic decay lifetimes, since the electronic properties of the water molecule (e.g. polarizability) would change upon the proton loss. Recent studies on electronic decay following core ionization of liquid water show that the interplay between electronic decay and nuclear dynamics needs to taken into account to obtain qualitatively correct decay observables in extended systems [96, 179].

The computed timescales of the interatomic electronic decay for the microhydrated Mg^{4+} and Mg^{3+} cations are remarkably short. Thus, the ICD lifetimes of excited, hexahydrated Mg^{4+} and Mg^{3+} cations with holes in the $2s$ orbital were found to be even shorter (≈ 0.8 fs) than the Auger lifetime of Mg^{3+} (1.9 fs). Experiments on excited Mg^{3+} cations in aqueous solutions support our results and yield an ultrashort ICD lifetime of 1.5 fs. Moreover, also the isoelectronic Na^{2+} and Al^{4+} cations were observed to decay in aqueous solutions on a comparable timescale, the corresponding ICD lifetimes being 3.1 and 0.9 fs, respectively. We were able to explain the faster decay of Mg^{3+} compared to Na^{2+} by conducting decay lifetime calculations in microsolvated clusters comprising the metal ions and their first solvation shell. In the asymptotic range of metal-oxygen distances the increase of the ion's charge leads to a growth of the ICD lifetimes. This result can be explained by the charge dependent parameters within the virtual photon model. At short metal-oxygen distances polarization of the water neighbor enhances ICD the stronger the higher the charge of the metal is. Surprisingly, the ICD lifetimes of monohydrated Na^{2+}, Mg^{3+} and the isoelectronic Ne are virtually equal at short metal-oxygen distances. We conclude that the faster decay of Mg^{3+} compared to Na^{2+} is both due to smaller metal-oxygen distances and the higher degree of polarization of the ligand for the magnesium. The discrepancy of the absolute experimental and computed lifetimes is of factor two. We show that the different levels of electronic correlation in the description of the initial and final states of ICD within the Fano-ADC-Stieltjes scheme are responsible for this discrepancy.

A further important finding is the interaction of the microsolvated Mg^{3+} cations decaying by ICD with the charge transfer states, where an electron is transferred into the empty $3s$ orbital of magnesium. Such interactions strongly enhance the interatomic decay and are expected to appear not only in connection with ICD but also with ETMD. In the $Mg^{3+}\cdot H_2O$ cluster the interaction with charge transfer states occurs at metal-

oxygen distances larger than the equilibrium ones. By varying the charge state of the cation and the electronic properties of the ligand, systems may be found, where charge transfer is possible close to the equilibrium geometry. In this context, methodological development is necessary to investigate a broader range of model systems. The currently available Fano-ADC-Stieltjes method is restricted to singly and doubly ionized as well excited states of systems which can be described by a single determinant in the neutral ground state. For the application of this scheme to a broader range of charge states it can be combined with an universal electronic structure approach such as e.g. MRCI instead of ADC.

ICD of metal ions is able to initiate repulsive nuclear dynamics in their vicinity few femtoseconds after the absorption of the photon. Therefore, studying ICD and the parameters which determine its timescale is important to estimate the times at which X-Ray induced damage sets on in metalloproteins. Such knowledge is needed in the context of the recently formulated idea of the serial femtosecond structure determination at XFELs, in which the short duration of the X-Ray pulses is meant to provide damage-free structures of proteins.

For ETMD, our calculations in Mg^{3+} and Mg^{4+} support the results of earlier studies which showed that this process takes place on a timescale of few tens of femtoseconds in microhydrated metal cations [93]. In particular, the ETMD(3) mechanism becomes very efficient if the metal cation is surrounded by a complete solvation shell of water molecules as the lifetime computations in $Mg^{4+}\cdot(H_2O)_6$ reveal. It strongly benefits from the nonlinear scaling of the decay width with the number of neighbors and from reduced water-water distances. In addition, increased polarization of the neighbors should translate into the increased overlap between the occupied orbitals of the neighbors with the empty orbitals on the cation which should increase the rates of interatomic decay processes. Interestingly, the ETMD lifetimes of the hexahydrated Mg^{4+} and Mg^{3+} cations are very similar although the degree of the water's polarization is considerably higher for the Mg^{4+}. Keeping in mind that the Auger cascades in heavier elements such as transition metals yield broad charge distributions, the dependence or the ETMD lifetimes on the charge state of the metal cations deserves further investigations. The transition metals are the predominant metal species in the metalloenzymes and are thus expected to play an important role in the X-Ray induced damage of the latter.

Bibliography

[1] V. May and O. Kühn, *Charge and energy transfer dynamics in molecular systems*, Wiley-VCH, Weinheim, 2., revised and enlarged edition, 2004.

[2] A. Nitzan, *Chemical dynamics in condensed phases*, Oxford University Press, 1. publ. in paperback edition, 2013.

[3] R. A. Marcus, *Rev. Mod. Phys.* **65**, 599 (1993).

[4] L. S. Cederbaum, J. Zobeley, and F. Tarantelli, *Phys. Rev. Lett.* **79**, 4778 (1997).

[5] M. Förstel, T. Arion, and U. Hergenhahn, *J. Electron. Spectrosc. Relat. Phenom.* **191**, 16 (2013).

[6] S. Kopelke, Y.-C. Chiang, K. Gokhberg, and L. S. Cederbaum, *J. Chem. Phys.* **137**, 034302 (2012).

[7] G. Jabbari, K. Sadri, L. S. Cederbaum, and K. Gokhberg, *J. Chem. Phys.* **144**, 164307 (2016).

[8] J. Zobeley, R. Santra, and L. S. Cederbaum, *J. Chem. Phys.* **115**, 5076 (2001).

[9] S. Marburger, O. Kugeler, U. Hergenhahn, and T. Möller, *Phys. Rev. Lett.* **90**, 203401 (2003).

[10] T. Jahnke, A. Czasch, M. S. Schöffler, S. Schlössler, A. Knapp, M. Käsz, J. Titze, C. Wimmer, K. Kreidi, R. E. Grisenti, A. Staudte, O. Jagutzki, U. Hergenhahn, H. Schmidt-Böcking, and R. Dörner, *Phys. Rev. Lett.* **93**, 163401 (2004).

[11] M. Mucke, M. Braune, S. Barth, M. Förstel, T. Lischke, V. Ulrich, T. Arion, U. Becker, A. Bradshaw, and U. Hergenhahn, *Nat. Phys.* **6**, 143 (2010).

[12] T. Jahnke, H. Sann, T. Havermeier, K. Kreidi, C. Stuck, M. Meckel, M. Schöffler, N. Neumann, R. Wallauer, S. Voss, A. Czasch, O. Jagutzki, A. Malakzadeh, F. Afaneh, T. Weber, H. Schmidt-Böcking, and R. Dörner, *Nat. Phys.* **6**, 139 (2010).

[13] G. A. Grieves and T. M. Orlando, *Phys. Rev. Lett.* **107**, 016104 (2011).

[14] G. Öhrwall, N. Ottoson, W. Pokapanich, S. Legendre, S. Svensson, and O. Björneholm, *J. Phys. Chem. B.* **114**, 17057 (2010).

[15] M. Lundwall, W. Pokapanich, H. Bergersen, A. Lindblad, T. Rander, G. Öhrwall, M. Tchaplyguine, S. Barth, U. Hergenhahn, S. Svensson, and O. Björneholm, *J. Chem. Phys.* **126**, 214706 (2007).

[16] E. Fasshauer, M. Förstel, S. Pallmann, M. Pernpointner, and U. Hergenhahn, *New J. Phys.* **16**, 103026 (2014).

[17] M. Thompson, M. D. Baker, A. Christie, and J. F. Tyson, *Auger electron spectroscopy*, Wiley New York, 1985.

[18] V. Averbukh, P. V. Demekhin, P. Kolorenč, S. Scheit, S. D. Stoychev, A. I. Kuleff, Y.-C. Chiang, K. Gokhberg, S. Kopelke, N. Sisourat, and L. S. Cederbaum, *J. Electron Spectrosc. Relat. Phenom.* **183**, 36 (2011).

[19] R. Santra and L. S. Cederbaum, *Phys. Rep.* **368**, 1 (2002).

[20] V. Averbukh and L. S. Cederbaum, *J. Chem. Phys.* **123**, 204107 (2005).

[21] P. Kolorenč, V. Averbukh, K. Gokhberg, and L. S. Cederbaum, *J. Chem. Phys.* **129**, 244102 (2008).

[22] Y. Sajeev, A. Ghosh, N. Vaval, and S. Pal, *Int. Rev. Phys. Chem.* **33**, 397 (2014).

[23] G. Öhrwall, M. Tchaplyguine, M. Lundwall, R. Feifel, H. Bergersen, T. Rander, A. Lindblad, J. Schulz, S. Peredkov, S. Barth, S. Marburger, U. Hergenhahn, S. Svensson, and O. Björneholm, *Phys. Rev. Lett.* **93**, 173401 (2004).

[24] F. Trinter, J. B. Williams, M. Weller, M. Waitz, M. Pitzer, J. Voigtsberger, C. Schober, G. Kastirke, C. Müller, C. Goihl, P. Burzynski, F. Wiegandt, T. Bauer, R. Wallauer, H. Sann, A. Kalinin, L. P. H. Schmidt, M. Schöffler, N. Sisourat, and T. Jahnke, *Phys. Rev. Lett.* **111**, 093401 (2013).

[25] K. Schnorr, A. Senftleben, M. Kurka, A. Rudenko, L. Foucar, G. Schmid, A. Broska, T. Pfeifer, K. Meyer, D. Anielski, R. Boll, D. Rolles, M. Kübel, M. F. Kling, Y. H. Jiang, S. Mondal, T. Tachibana, K. Ueda, T. Marchenko, M. Simon, G. Brenner, R. Treusch, S. Scheit, V. Averbukh, J. Ullrich, C. D. Schröter, and R. Moshammer, *Phys. Rev. Lett.* **111**, 093402 (2013).

[26] K. Sakai, S. D. Stoychev, T. Ouchi, I. Higuchi, M. Schöffler, T. Mazza, H. Fukuzawa, K. Nagaya, M. Yao, Y. Tamenori, A. I. Kuleff, N. Saito, and K. Ueda, *Phys. Rev. Lett.* **106**, 033401 (2011).

[27] M. Förstel, M. Mucke, T. Arion, A. M. Bradshaw, and U. Hergenhahn, *Phys. Rev. Lett.* **106**, 033402 (2011).

[28] T. Hartman, P. N. Juranić, K. Collins, B. Reilly, N. Appathurai, and R. Wehlitz, *Phys. Rev. Lett.* **108**, 023001 (2012).

[29] J. P. Toennies and A. F. Vilesov, *Angew. Chem. Int. Ed.* **43**, 2622 (2004).

[30] F. Stienkemeier and K. K. Lehmann, *J. Phys. B.: At. Mol. Opt. Phys.* **39**, R127 (2006).

[31] R. Santra and L. S. Cederbaum, *Phys. Rev. Lett.* **90**, 153401 (2003).

[32] Y. Morishita, X.-J. Liu, N. Saito, T. Lischke, M. Kato, G. Prümper, M. Oura, H. Yamaoka, Y. Tamenori, I. H. Suzuki, and K. Ueda, *Phys. Rev. Lett.* **96**, 243402 (2006).

[33] K. Kreidi, T. Jahnke, T. Weber, T. Havermeier, X. Liu, Y. Morisita, S. Schössler, L. Schmidt, M. Schöffler, M. Odenweller, N. Neumann, L. Foucar, J. Titze, B. Ulrich, F. Sturm, C. Stuck, R. Wallauer, S. Voss, I. Lauter, H. K. Kim, M. Rudloff, H. Fukuzawa, G. Prümper, N. Saito, K. Ueda, A. Czasch, O. Jagutzki, H. Schmidt-Böcking, S. S., P. V. Demekhin, and R. Dörner, *Phys. Rev. A* **78**, 043422 (2008).

[34] S. Scheit, V. Averbukh, H.-D. Meyer, N. Moiseyev, R. Santra, T. Sommerfeld, J. Zobeley, and L. S. Cederbaum, *J. Chem. Phys.* **121**, 8393 (2004).

[35] R. W. Howell, *Int. J. Radiat. Biol.* **84**, 959 (2008).

[36] I. Tavernelli, M.-P. Gaigeot, R. Vuilleumier, C. Stia, A. Hervé du Penhoat, and M.-F. Politis, *ChemPhysChem* **9**, 2099 (2008).

[37] S. D. Stoychev, A. I. Kuleff, and L. S. Cederbaum, *J. Chem. Phys.* **133**, 154307 (2010).

[38] E. Alizadeh, T. M. Orlando, and L. Sanche, *Annu. Rev. Phys. Chem.* **66**, 379 (2015).

[39] C. v. Sonntag, *Free-radical-induced DNA damage and its repair*, Springer, Berlin; Heidelberg, 2006.

[40] K. Gokhberg, P. Kolorenč, A. I. Kuleff, and L. S. Cederbaum, *Nature* **505**, 661 (2014).

[41] F. Trinter, M. S. Schöffler, H. K. Kim, F. P. Sturm, K. Cole, N. Neumann, A. Vredenborg, J. Williams, I. Bocharova, R. Guillemin, M. Simon, A. Belkacem, A. L. Landers, T. Weber, H. Schmidt-Böcking, R. Dörner, and T. Jahnke, *Nature* **505**, 664 (2014).

[42] R. Roots and S. Okada, *Radiat. Res.* **64**, 306 (1975).

[43] D. Emfietzoglou, I. Kyriakou, I. Abril, R. Garcia-Molina, I. Petsalakis, H. Nikjoo, and A. Pathak, *Nucl. Instrum. Meth. B.* **267**, 45 (2009).

[44] I. Bertini, H. B. Gray, E. I. Stiefel, and J. S. Valentine, *Biological Inorganic Chemistry*, University Science Books, Sausalito, 2007.

[45] O. Carugo and K. Djinović-Carugo, *Trends Biochem. Sci.* **30**, 213 (2005).

[46] M. Schlitz and B. Bricogne, *J. Synchrotron Radiat.* **14**, 34 (2007).

[47] J. Yano, J. Kern, K.-D. Irrgang, M. J. Latimer, U. Bergmann, P. Glatzel, Y. Pushkar, J. Biesiadka, B. Loll, K. Sauer, J. Messinger, A. Zouni, and V. K. Yachandra, *Proc. Natl. Acad. Sci.* **102**, 12047 (2005).

[48] G. I. Berglund, G. H. Carlsson, A. T. Smith, H. Szöke, A. Henriksen, and J. Hajdu, *Nature* **417**, 463 (2002).

[49] M. Schlitz and B. Bricogne, *Proc. Natl. Acad. Sci.* **101**, 8569 (2004).

[50] I. Schlichting, J. Berendzen, K. Chu, A. M. Stock, S. A. Maves, D. E. Benson, R. M. Sweet, D. Ringe, G. A. Petsko, and S. G. Sligar, *Science* **287**, 1615 (2000).

[51] H. N. Chapman, P. Fromme, A. Barty, T. A. White, R. A. Kirian, A. Aquila, M. S. Hunter, J. Schulz, D. P. DePonte, U. Weierstall, et al., *Nature* **470**, 73 (2011).

[52] C. Pellegrini, A. Marinelli, and S. Reiche, *Rev. Mod. Phys.* **88**, 015006 (2016).

[53] V. Averbukh and L. S. Cederbaum, *J. Chem. Phys.* **125**, 094107 (2006).

[54] R. Santra, J. Zobeley, and L. S. Cederbaum, *Phys. Rev. B* **64**, 245104 (2001).

[55] M. Born and J. R. Oppenheimer, *Ann. Phys.* **84**, 457 (1927).

[56] A. Szabo and N. S. Ostlund, *Modern Quantum Chemistry*, Dover, Mineola, NY, 1996.

[57] T. Helgaker, P. Jorgensen, and J. Olsen, *Molecular Electronic-Structure Theory*, Wiley, New York, 2000.

[58] C. Møller and M. S. Plesset, *Phys. Rev.* **46**, 618 (1934).

[59] J. Schirmer and A. Barth, *Z. Phys. A* **317**, 267 (1984).

[60] A. L. Fetter and J. D. Walecka, *Quantum Theory of Many-Particle Systems*, Dover, Mineola, NY, 2003.

[61] J. Schirmer, L. S. Cederbaum, and O. Walter, *Phys. Rev. A* **28**, 1237 (1983).

[62] A. B. Trofimov and J. Schirmer, *J. Chem. Phys.* **123**, 144115 (2005).

[63] F. Mertins and J. Schirmer, *Phys. Rev. A* **53**, 2140 (1996).

[64] J. R. Taylor, *Scattering theory*, Wiley, New York, 1972.

[65] V. I. Kukulin, V. M. Krasnopol'sky, and J. Horacek, *Theory of resonances*, Kluwer Academic Publishers, Dordrecht, 1989.

[66] U. Fano, *Phys. Rev.* **124**, 1866 (1961).

[67] P. A. M. Dirac, *Z. Phys.* **44**, 585 (1927).

[68] N. Moiseyev, *Phys. Rep.* **302**, 212 (1998).

[69] U. V. Riss and H.-D. Meyer, *J. Phys. B* **26**, 4503 (1993).

[70] R. Santra, L. S. Cederbaum, and H.-D. Meyer, *Chem. Phys. Lett.* **303**, 413 (1999).

[71] P. W. Langhoff, *Electron-Molecule and Photon-Molecule Collisions*, Plenum Press, New York, 1979.

[72] A. U. Hazi, *Electron-Molecule and Photon-Molecule Collisions*, Plenum Press, New York, 1979.

[73] U. Fano and J. W. Cooper, *Rev. Mod. Phys.* **40**, 441 (1968).

[74] W. P. Reinhardt, *Comput. Phys. Commun.* **17**, 1 (1979).

[75] F. Müller-Plathe and G. H. F. Diercksen, *Electronic Structure of Atoms, Molecules and Solids, Proceedings of the II Escola Brasileira de Estruture Electrônica*, World Scientific, Singapore, 1990.

[76] H.-J. Werner, P. J. Knowles, G. Knizia, F. R. Manby, M. Schütz, P. Celani, T. Korona, R. Lindh, A. Mitrushenkov, G. Rauhut, K. R. Shamasundar, T. B. Adler, R. D. Amos, A. Bernhardsson, A. Berning, D. L. Cooper, M. J. O. Deegan, A. J. Dobbyn, F. Eckert, E. Goll, C. Hampel, A. Hesselmann, G. Hetzer, T. Hrenar, G. Jansen, C. Köppl, Y. Liu, A. W. Lloyd, R. A. Mata, A. J. May, S. J. McNicholas, W. Meyer, M. E. Mura, A. Nicklass, D. P. O'Neill, P. Palmieri, D. Peng, K. Pflüger, R. Pitzer, M. Reiher, T. Shiozaki, H. Stoll, A. J. Stone, R. Tarroni, T. Thorsteinsson, and M. Wang, MOLPRO, version 2010.1, a package of ab initio programs, 2012.

[77] D. E. Woon and J. T. H. Dunning, *J. Chem. Phys.* **100**, 2975 (1994).

[78] K. L. Schuchardt, B. T. Didier, T. Elsethagen, L. Sun, V. Gurumoorthi, J. Chase, J. Li, and T. L. Windus, *Journal of Chemical Information and Modeling* **47**, 1045 (2007).

[79] F.-M. Tao and Y.-K. Pan, *J. Chem. Phys.* **97**, 4989 (1992).

[80] F. Tarantelli, *Chem. Phys.* **329**, 11 (2006).

[81] G. Karlström, R. Lindh, P.-A. Malmqvist, B. O. Roos, U. Ryde, V.Veryazov, P.-O. Widmark, M. Cossi, B. Schimmelpfennig, P. Neogrady, and L. Seijo, *Computational Material Science* **28**, 222 (2003).

[82] K. Kaufmann, W. Baumeister, and M. Jungen, *J. Phys. B.: At. Mol. Opt. Phys.* **22**, 2223 (1989).

[83] M. W. Schmidt, K. K. Baldridge, J. A. Boatz, S. T. Elbert, M. S. Gordon, J. H. Jensen, S. Koseki, N. Matsunaga, K. A. Nguyen, S. J. Su, T. L. Windus, M. Dupuis, and J. A. Montgomery, *J.Comput.Chem.* **14**, 1347 (1993).

[84] F. Tarantelli and L. S. Cederbaum, *Phys. Rev. A* **46**, 81 (1992).

[85] A. Mahler and A. K. Wilson, *J. Chem. Phys.* **142**, 084102 (2015).

[86] S. Scheit, L. S. Cederbaum, and H.-D. Meyer, *J. Chem. Phys.* **118**, 2092 (2003).

[87] P. V. Demekhin, S. Scheit, S. D. Stoychev, and L. S. Cederbaum, *Phys. Rev. A* **78**, 043421 (2008).

[88] T. Miteva, Y.-C. Chiang, P. Kolorenč, A. I. Kuleff, K. Gokhberg, and L. S. Cederbaum, *J. Chem. Phys.* **141**, 064307 (2014).

[89] H. Meyer, *Annu. Rev. Phys. Chem.* **53**, 141 (2002).

[90] E. D. Glendening and D. Feller, *J. Phys. Chem.* **100**, 4790 (1996).

[91] V. R. Saunders and J. H. van Lenthe, *Mol. Phys.* **48**, 923 (1983).

[92] GAMESS-UK is a package of ab initio programs. See: "http://www.cfs.dl.ac.uk/gamess-uk/index.shtml", M. F. Guest, I. J. Bush, H. J. J. van Dam, P. Sherwood, J. M. H. Thomas, J. H. van Lenthe, R. W. A. Havenith, J. Kendrick, "The GAMESS-UK electronic structure package: algorithms, developments and applications", Molecular Physics, Vol. 103, No. 6-8, 20 March-20 April 2005, 719-747.

[93] I. B. Müller and L. S. Cederbaum, *J. Chem. Phys.* **122**, 094305 (2005).

[94] N. V. Kryzhevoi, V. Averbukh, and L. S. Cederbaum, *Phys. Rev. B* **76**, 094513 (2007).

[95] W. Pokapanich, N. V. Kryzhevoi, N. Ottosson, S. Svensson, L. S. Cederbaum, G. Öhrwall, and O. Björneholm, *J. Am. Chem. Soc.* **133**, 13430 (2011).

[96] P. Slavíček, B. Winter, L. S. Cederbaum, and N. V. Kryzhevoi, *J. Am. Chem. Soc.* **136**, 18170 (2014).

[97] D. Woon and J. T. H. Dunning, *J. Chem. Phys.* **100**, 2975 (1994).

[98] D. Woon and J. T. H. Dunning, *J. Chem. Phys.* **103**, 4572 (1995).

[99] J. T. H. Dunning, *J. Chem. Phys.* **90**, 1007 (1989).

[100] D. Feller, E. D. Glendening, D. E. Woon, and M. W. Feyereisen, *J. Chem. Phys.* **103**, 3526 (1995).

[101] H. Ohtaki and T. Radnai, *Chem. Rev.* **93**, 1157 (1993).

[102] Y. Marcus, *Chem. Rev.* **109**, 1346 (2009).

[103] J. Makarewicz, *J. Chem. Phys.* **129**, 184310 (2008).

[104] P. Kolorenč and N. Sisourat, *J. Chem. Phys.* **143**, 224310 (2015).

[105] E. Miliordos and S. S. Xantheas, *Phys. Chem. Chem. Phys.* **16**, 6886 (2013).

[106] R. A. Kendall, T. H. Dunning Jr., and H. J. R., *J. Chem. Phys.* **96**, 6796 (1992).

[107] R. Dörner, H. Schmidt-Böcking, T. Weber, T. Jahnke, M. Schöffler, A. Knapp, M. Hattass, A. Czasch, L. P. H. Schmidt, and O. Jagutzki, *Radiat. Phys. Chem.* **70**, 191 (2004).

[108] T. Schneider and J.-M. Rost, *Phys. Rev. A* **67**, 062704 (2003).

[109] R. Wehlitz, P. N. Juranić, and D. V. Lukić, *Phys. Rev. A* **78**, 033428 (2008).

[110] J. Bluett, D. Lukic, S. Whitfield, and R. Wehlitz, *Nucl. Instrum. Meth. B.* **241**, 114 (2005).

[111] A. E. Kramida, Y. Ralchenko, J. Reader, and NIST ASD TEAM, (2015).*NIST Atomic Spectra Database* (version 5.3), [Online]. Available: `http://physics.nist.gov/asd`. National Institute of Standards and Technology, Gaithersburg, MD.

[112] N. Sisourat, N. V. Kryzhevoi, P. Kolorenč, S. Scheit, T. Jahnke, and L. S. Cederbaum, *Nat. Phys.* **6**, 508 (2010).

[113] J. A. R. Samson and W. C. Stolte, *J. Electron Spectrosc. Relat. Phenom.* **123**, 265 (2002).

[114] V. Stumpf, N. V. Kryzhevoi, K. Gokhberg, and L. S. Cederbaum, *Phys. Rev. Lett.* **112**, 193001 (2014).

[115] T. Havermeier, T. Jahnke, K. Kreidi, R. Wallauer, S. Voss, M. Schöffler, S. Schössler, L. Foucar, N. Neumann, J. Titze, H. Sann, M. Kühnel, J. Voigtsberger, J. H. Morilla, W. Schöllkopf, H. Schmidt-Böcking, R. E. Grisenti, and R. Dörner, *Phys. Rev. Lett.* **104**, 133401 (2010).

[116] A. C. LaForge, V. Stumpf, K. Gokhberg, J. von Vangerow, F. Stienkemeier, N. V. Kryzhevoi, P. O'Keeffe, A. Ciavardini, S. R. Krishnan, M. Coreno, K. C. Prince, R. Richter, R. Moshammer, T. Pfeifer, L. S. Cederbaum, and M. Mudrich, *Phys. Rev. Lett.* **116**, 203001 (2016).

[117] G. Krois, J. V. Pototschnig, F. Lackner, and W. E. Ernst, *J. Phys. Chem. A* **117**, 13719 (2013).

[118] Y. Ovcharenko, V. Lyamayev, R. Katzy, M. Devetta, A. LaForge, P. O'Keeffe, O. Plekan, P. Finetti, M. Di Fraia, M. Mudrich, M. Krikunova, P. Piseri, M. Coreno, N. Brauer, T. Mazza, S. Stranges, C. Grazioli, R. Richter, K. C. Prince, M. Drabbels, C. Callegari, F. Stienkemeier, and T. Möller, *Phys. Rev. Lett.* **112**, 073401 (2014).

[119] C. C. Wang, O. Kornilov, O. Gessner, J. H. Kim, D. S. Peterka, and D. M. Neumark, *J. Phys. Chem. A* **112**, 9356 (2008).

[120] D. Buchta, S. R. Krishnan, N. B. Brauer, M. Drabbels, P. OKeeffe, M. Devetta, M. Di Fraia, C. Callegari, R. Richter, M. Coreno, K. C. Prince, F. Stienkemeier, J. Ullrich, R. Moshammer, and M. Mudrich, *J. Chem. Phys.* **139**, 084301 (2013).

[121] T. Diederich, T. Döppner, T. Fennel, J. Tiggesbäumker, and K.-H. Meiwes-Broer, *Phys. Rev. A* **72**, 023203 (2005).

[122] W.-C. Tung, M. Pavanello, and L. Adamowicz, *J. Chem. Phys.* **136**, 104309 (2012).

[123] J. J. Yeh and I. Lindau, *At. Data Nucl. Data Tables* **32**, 1 (1985).

[124] Y. Hikosaka, T. Kaneyasu, P. Lablanquie, F. Penent, E. Shigemasa, and K. Ito, *Phys. Rev. A* **92**, 033413 (2015).

[125] H. P. Kelly, *Phys. Rev. A* **11**, 556 (1975).

[126] B. Kanngiesser, M. Jainz, S. Brünken, W. Benten, C. Gerth, K. Godehusen, K. Tiedtke, P. van Kampen, A. Tutay, P. Zimmermann, V. F. Demekhin, and A. G. Kochur, *Phys. Rev. A* **62**, 014702 (2000).

[127] N. Saito, I. H. Suzuki, and S. D. Stoychev, *Chem. Phys. Lett.* **441**, 16 (2007).

[128] T. Jahnke, *J. Phys. B.: At. Mol. Opt. Phys.* **48**, 082001 (2015).

[129] V. Stumpf, S. Scheit, P. Kolorenč and K. Gokhberg, *Chem. Phys.*, http://dx.doi.org/10.1016/j.chemphys.2016.08.018 (2016).

[130] V. Stumpf, P. Kolorenč, K. Gokhberg, and L. S. Cederbaum, *Phys. Rev. Lett.* **110**, 258302 (2013).

[131] T. Arion, M. Mucke, M. Förstel, A. M. Bradshaw, and U. Hergenhahn, *J. Chem. Phys.* **134**, 074306 (2011).

[132] R. Feifel, M. Tchaplyguine, G. Öhrwall, M. Salonen, M. Lundwall, R. R. T. Marinho, M. Gisselbrecht, S. L. Sorensen, A. Naves de Brito, L. Karlsson, N. Mårtensson, S. Svensson, and O. Björneholm, *Eur. Phys. J. D* **30**, 343 (2004).

[133] N. V. Kryzhevoi and L. S. Cederbaum, *Angew. Chem. Int. Ed.* **50**, 1306 (2011).

[134] W. Mehlhorn, *Z. Phys.* **187**, 21 (1965).

[135] J. Jauhiainen, A. Kivimäki, S. Aksela, O.-P. Sairanen, and H. Aksela, *J. Phys. B.: At. Mol. Opt. Phys.* **28**, 4091 (1995).

[136] J. Viefhaus, M. Braune, S. Korica, A. Reinköster, D. Rolles, and U. Becker, *J. Phys. B.: At. Mol. Opt. Phys.* **38**, 3885 (2005).

[137] K. Ueda, private communication.

[138] S. J. George, J. Fu, Y. Guo, O. B. Drury, S. Friedrich, T. Rauchfuss, P. I. Volkers, J. C. Peters, V. Scott, S. D. Brown, C. M. Thomas, and S. P. Cramer, *Inorg. Chim. Acta* **361**, 1157 (2008).

[139] J. G. Mesu, A. M. Beale, F. M. F. de Groot, and B. M. Weckhuysen, *J. Phys. Chem. B* **110**, 17671 (2006).

[140] S. B. Nielsen and L. H. Andersen, *Biophys. Chem.* **124**, 229 (2006).

[141] P. E. Barran, N. R. Walker, and A. J. Stace, *J. Chem. Phys.* **112**, 6173 (2000).

[142] C. Steinbach and U. Buck, *J. Chem. Phys.* **122**, 134301 (2005).

[143] M. Peschke, A. T. Blades, and P. Kebarle, *J. Phys. Chem. A* **102**, 9978 (1998).

[144] I. Unger and R. Seidel and S. Thürmer and E. F. Aziz and L. S. Cederbaum and E. Muchová and P. Slavíček, and B. Winter and N. V. Kryzhevoi, ArXiv e-prints, 1604.08892 (2016).

[145] O. Svoboda, D. Hollas, M. Oncak, and P. Slavíček, *Phys. Chem. Chem. Phys.* **15**, 11531 (2013).

[146] O. Marsalek, C. G. Elles, P. A. Pieniazek, E. Pluhařová, J. VandeVondele, S. E. Bradforth, and P. Jungwirth, *J. Chem. Phys.* **135**, 224510 (2011).

[147] T. Jahnke, A. Czasch, M. Schöffler, S. Schössler, M. Käsz, J. Titze, K. Kreidi, R. E. Grisenti, A. Staudte, O. Jagutzki, L. Schmidt, T. Weber, H. Schmidt-Böcking, K. Ueda, and R. Dörner, *Phys. Rev. Lett.* **99**, 153401 (2007).

[148] T. Ouchi, K. Sakai, H. Fukuzawa, X.-J. Liu, I. Higuchi, Y. Tamenori, K. Nagaya, H. Iwayama, M. Yao, D. Zhang, D. Ding, A. I. Kuleff, S. D. Stoychev, P. V. Demekhin, N. Saito, and K. Ueda, *Phys. Rev. Lett.* **107**, 053401 (2011).

[149] R. Feifel, J. H. D. Eland, R. J. Squibb, M. Mucke, S. Zagorodskikh, P. Linusson, F. Tarantelli, P. Kolorenč, and V. Averbukh, *Phys. Rev. Lett.* **116**, 073001 (2016).

[150] J. Severs, F. Harris, S. Andrews, and D. Parry, *Chem. Phys.* **175**, 467 (1993).

[151] G. Handke, F. Tarantelli, A. Tarantelli, and L. Cederbaum, *J. Electron. Spectrosc. Relat. Phenom.* **75**, 109 (1995).

[152] W. Pokapanich, H. Bergersen, I. L. Bradeanu, R. R. T. Marinho, A. Lindblad, S. Legendre, A. Rosso, S. Svensson, O. Björneholm, M. Tchaplyguine, G. Öhrwall, N. V. Kryzhevoi, and L. S. Cederbaum, *J. Am. Chem. Soc.* **131**, 7264 (2009).

[153] N. Ottosson, G. Öhrwall, and O. Björneholm, *Chem. Phys. Lett.* **543**, 1 (2012).

[154] V. Averbukh, I. B. Müller, and L. S. Cederbaum, *Phys. Rev. Lett.* **93**, 263002 (2004).

[155] V. Stumpf, K. Gokhberg, and L. S. Cederbaum, *Nat. Chem.* **8**, 237 (2016).

[156] O. Vendrell, S. D. Stoychev, and L. S. Cederbaum, *ChemPhysChem* **11**, 1006 (2010).

[157] E. Kamarchik, O. Kostko, J. M. Bowman, M. Ahmed, and A. I. Krylov, *J. Chem. Phys.* **132**, 194311 (2010).

[158] P. O'Neill, *Radiation-induced damage in DNA*, Elsevier Science B.V., Amsterdam, 2001.

[159] M.-P. Gaigeot, R. Vuilleumier, C. Stia, M. E. Galassi, R. Rivarola, B. Gervais, and M.-F. Politis, *J. Phys. B.: At. Mol. Opt. Phys.* **40**, 1 (2007).

[160] K. Takakura, *Acta Oncol.* **35**, 883 (1996).

[161] H. H. Jawad and D. E. Watt, *Int. J. Radiat. Biol.* **50**, 665 (1986).

[162] G. Jabbari, S. Klaiman, Y.-C. Chiang, F. Trinter, T. Jahnke, and K. Gokhberg, *J. Chem. Phys.* **140**, 224305 (2014).

[163] K. Gokhberg, S. Kopelke, N. V. Kryzhevoi, P. Kolorenč, and L. S. Cederbaum, *Phys. Rev. A* **81**, 013417 (2010).

[164] R. Santra and L. S. Cederbaum, *J. Chem. Phys.* **115**, 6853 (2001).

[165] N. Vaval and L. S. Cederbaum, *J. Chem. Phys.* **126**, 164110 (2007).

[166] T. Ouchi, K. Sakai, H. Fukuzawa, I. Higuchi, P. V. Demekhin, Y.-C. Chiang, S. D. Stoychev, A. I. Kuleff, T. Mazza, M. Schöffler, K. Nagaya, M. Yao, Y. Tamenori, N. Saito, and K. Ueda, *Phys. Rev. A* **83**, 053415 (2011).

[167] V. Averbukh and L. S. Cederbaum, *Phys. Rev. Lett.* **96**, 053401 (2006).

[168] R. B. Martin, *J. Inorg. Biochem.* **44**, 141 (1991).

[169] A. Ghosh, S. Paj, and N. Vaval, *J. Chem. Phys.* **139**, 064112 (2013).

[170] A. Ghosh and N. Vaval, *J. Chem. Phys.* **141**, 234108 (2014).

[171] V. Stumpf, C. Brunken, and K. Gokhberg, *J. Chem. Phys.* **145**, 104306 (2016).

[172] W. F. Chan, G. Cooper, and C. E. Brion, *J. Chem. Phys.* **178**, 387 (1993).

[173] M. Ruberti, R. Yun, K. Gokhberg, S. Kopelke, L. S. Cederbaum, F. Tarantelli, and V. Averbukh, *J. Chem. Phys.* **139**, 144107 (2013).

[174] I. B. Müller, PhD thesis, Heidelberg University, 2006.

[175] C. T. Johnson and A. E. Kingston, *J. Phys. B: At. Mol. Phys.* **20**, 5757 (1987).

[176] M. M. Probst, *Chem. Phys. Lett.* **137**, 229 (1987).

[177] F. Floris, M. Persico, A. Tani, and J. Tomasi, *Chem. Phys.* **195**, 207 (1995).

[178] J. A. White, E. Schwegler, G. Galli, and F. Gygi, *J. Chem. Phys.* **113**, 4668 (2000).

[179] S. Thürmer, M. Ončák, N. Ottosson, R. Seidel, U. Hergenhahn, S. E. Bradforth, P. Slavíček, and B. Winter, *Nat. Chem.* **5**, 590 (2013).

Acknowledgement

I am very grateful to my supervisor Prof. Lorenz S. Cederbaum for offering me an interesting research topic, for giving me the possibility to work independently and for the financial support.

I also would like to acknowledge Prof. Andreas Dreuw for evaluating my thesis.

I want to thank my mentor and friend Dr. Kirill Gokhberg whose clear way of thinking made the scientific discussions very instructive. I highly appreciate his positive attitude and his patience in teaching the PhD students.

Moreover, I would like to acknowledge the following persons and organizations whose support was indispensable for the completion of this work:

- Prof. Jochen Schirmer, Dr. Tsveta Miteva and Dr. Kirill Gokhberg for proofreading my thesis.
- DFG-Forschergruppe 1789 "Intermolecular and Interatomic Coulombic Decay" for giving me the opportunity to participate in this unique scientific collaboration and for the financial support of my research visit to the Elettra Sincrotrone Trieste.
- IMPRS for Quantum Dynamics for funding the participation in conferences.
- Dr. Přemysl Kolořenc for hosting me during my visits in Prague, providing the codes for the decay width calculations and the continuous support during the whole period of my PhD.
- Our collaborators from the Freiburg Nanophysics group Dr. Aaron LaForge and PD Marcel Mudrich for the invitation to the exciting beamtime in Trieste.
- Our collaborators from the research group of Prof. Kiyoshi Ueda for providing us recent results of coincident spectroscopy measurements in mixed neon-krypton clusters.
- Dr. Shachar Klaiman and Dr. Nikolai Kryzhevoi for sharing their scientific expertise and for the numerous fruitful discussions.
- Dr. Ying-Chih Chiang for running the nuclear dynamics simulations and explaining the corresponding computational methods.
- My office neighbor Dr. Evgeniy Gromov for the help with electronic structure methods, quantum chemistry software packages and for a comfortable working atmosphere.

- Dr. Adrian Komainda for voluntarily supporting me in the supervision of the students.
- Our system administrators Dr. Frank Otto and Dr. Markus Schröder for providing a stable and user-friendly IT infrastructure.
- Our secretary Annette Braun for taking care of the formalities and for the timely reminders of the important issues.
- My bachelor student Christoph Brunken for his assistance and his high-quality contributions to this work.
- Nikolay Golubev, Ghazal Jabbari, Rafael Beinke, Dr. Tsveta Miteva, Dr. Adrian Komainda, Dr. Elke Faßhauer, Dr. Federico Pont, Dr. Sivaranjana Reddy and other current and former members of the TC group who created a very pleasant and inspiring working environment.

I am also obliged to my family and my friends outside the TC group for supporting me throughout my studies. Finally, I would like to thank my beloved Valentina for her patience and kindness in every phase of my PhD project.

Eidesstattliche Versicherung

Eidesstattliche Versicherung gemäß §8 der Promotionsordnung der Naturwissenschaftlichen-Mathematischen Gesamtfakultät der Universität Heidelberg

1. Bei der eingereichten Dissertation zu dem Thema "Neutralization and relaxation of cations in an environment driven by interatomic decay processes" handelt es sich um meine eigenständig erbrachte Leistung.

2. Ich habe nur die angegebenen Quellen und Hilfsmittel benutzt und mich keiner unzulässigen Hilfe Dritter bedient. Insbesondere habe ich wörtlich oder sinngemäß aus anderen Werken übernommene Inhalte als solche kenntlich gemacht.

3. Die Arbeit oder Teile davon habe ich bislang nicht an einer Hochschule des In- oder Auslands als Bestandteil einer Prüfungs- oder Qualifikationsleistung vorgelegt.

4. Die Richtigkeit der vorstehenden Erklärungen bestätige ich.

5. Die Bedeutung der eidesstattlichen Versicherung und die strafrechtlichen Folgen einer unrichtigen oder unvollständigen eidesstattlichen Versicherung sind mir bekannt.

Ich versichere an Eides statt, dass ich nach bestem Wissen die reine Wahrheit erklärt und nichts verschwiegen habe.

Heidelberg, den

_____

Unterschrift